

学 位 論 文

Study of bottom baryon production in pp collisions

at $\sqrt{s} = 7 \text{ TeV}$

(重心系エネルギー 7TeV での陽子・陽子衝突における
ボトムバリオン生成の研究)

平成 27 年 12 月博士 (理学) 申請

東京大学大学院理学系研究科

物理学専攻

小 森 雄 斗

Abstract

Studies of the production of the bottom baryons Ω_b^- and Ξ_b^- including their antiparticles in pp collisions at $\sqrt{s} = 7$ TeV are performed using data corresponding to an integrated luminosity of 4.5 fb^{-1} collected with the ATLAS detector at the LHC. The bottom baryons are reconstructed in the decay modes of $\Omega_b^- \rightarrow J/\psi(\rightarrow \mu^+\mu^-) + \Omega^-(\rightarrow \Lambda^0(\rightarrow p\pi^-)K^-)$, $\Xi_b^- \rightarrow J/\psi(\rightarrow \mu^+\mu^-) + \Xi^-(\rightarrow \Lambda^0(\rightarrow p\pi^-)\pi^-)$, and their charge conjugates. A two-stage kinematical fit is applied for reducing the background. A large number of the background are suppressed by the second fit of imposing constraints of the decay vertex positions and the masses of preselected J/ψ , Λ^0 , and Ω^- (Ξ^-) candidates in the first fit. After the kinematical selections on the finite lifetime and the decay angle, the Ω_b^- (Ξ_b^-) signals with 3.6σ (2.9σ) significance were observed. The masses were measured to be $M_{\Omega_b^-} = 6035.8 \pm 10.6(\text{stat.})_{-1.1}^{+6.7}(\text{syst.})$ MeV for the Ω_b^- baryon and $M_{\Xi_b^-} = 5775.9 \pm 12.8(\text{stat.})_{-0.8}^{+5.9}(\text{syst.})$ MeV for the Ξ_b^- baryon. These results are consistent with the measurements reported by the CDF and LHCb experiments. The production cross sections are also discussed.

Contents

1	Introduction	- 9 -
2	Theoretical background	- 11 -
2.1	Hadron physics	- 11 -
2.1.1	Meson model	- 11 -
2.1.2	Baryon model	- 12 -
2.2	Bottom baryon model	- 13 -
3	LHC and ATLAS experiment	- 17 -
3.1	Large Hadron Collider	- 17 -
3.2	ATLAS Detector	- 19 -
3.2.1	Magnet systems	- 21 -
3.2.2	Inner detectors	- 21 -
3.2.3	Calorimeters	- 23 -
3.2.4	Muon detectors	- 24 -
3.3	Trigger system	- 27 -
4	Track parameters and vertex fit	- 29 -
4.1	Track parameters	- 29 -
4.1.1	Parameterization of helical motion	- 29 -
4.1.2	Five track parameters	- 30 -
4.2	Vertex fit	- 31 -
4.2.1	Fit procedure	- 31 -
4.2.2	Fit constraint	- 32 -
5	Event reconstruction	- 34 -
5.1	Decay kinematics	- 34 -
5.2	Monte-Carlo simulation	- 36 -
5.3	Data samples	- 38 -
5.4	Muon track reconstruction	- 38 -

5.4.1	Muon reconstruction	- 38 -
5.4.2	Muon selections	- 39 -
5.5	J/ψ reconstruction	- 40 -
5.6	Baryon reconstruction	- 46 -
5.6.1	Λ^0 reconstruction	- 46 -
5.6.2	Ξ^- reconstruction	- 54 -
5.6.3	Ω^- reconstruction	- 61 -
5.7	Bottom baryon reconstruction	- 67 -
5.7.1	Ω_b^- reconstruction	- 67 -
5.7.2	Ξ_b^- reconstruction	- 79 -
6	Results	- 84 -
6.1	Mass measurements	- 84 -
6.1.1	Unbinned maximum likelihood fit	- 84 -
6.1.2	Signal <i>p.d.f.</i>	- 84 -
6.1.3	Fit results	- 86 -
6.1.4	Systematic uncertainties	- 88 -
6.1.5	Mass results	- 91 -
6.2	Production cross sections	- 92 -
6.2.1	Systematic uncertainties	- 93 -
6.2.2	Production cross section results	- 94 -
6.3	Discussion and outlook	- 94 -
7	Conclusions	- 98 -
A	Distributions of the data and the MC samples	- 100 -
A.1	MC truth distributions	- 100 -
A.2	Baryon reconstruction	- 102 -
A.3	Ω^- and Ξ^- reconstruction efficiencies	- 104 -
A.4	Distributions of the Ω_b^- candidates	- 106 -
A.5	Distributions after the refit for the Ξ_b^- analysis	- 107 -
A.6	Distributions of the Ξ_b^- candidates	- 110 -
B	Unbinned maximum likelihood fit	- 111 -
C	Single Gaussian fit	- 112 -
D	Significance and systematic uncertainties	- 113 -
D.1	Significance	- 113 -
D.2	Systematic uncertainties of the tracking momentum scale	- 115 -

D.3 Systematic uncertainties of the pile-up effect - 116 -

Bibliography - 117 -

List of Figures

2.1	Baryon and meson models.	- 11 -
2.2	$J^P = 0^-$ mesons.	- 12 -
2.3	$J^P = 1^-$ mesons.	- 12 -
2.4	Baryon octet.	- 13 -
2.5	Baryon decuplet.	- 13 -
2.6	Baryon octet extended to the bottom baryons.	- 14 -
2.7	Baryon decuplet extended to the bottom baryons.	- 14 -
2.8	Ω_b^- mass distributions at the D0, CDF, and LHCb experiments [4] [10] [12].	- 16 -
3.1	Overall view of the LHC and its injectors [20].	- 18 -
3.2	Overall view of the LHC experiments [22].	- 19 -
3.3	Cutaway view of the ATLAS detector [23].	- 20 -
3.4	Geometry of the ATLAS magnet windings [23].	- 21 -
3.5	Cutaway view of the ATLAS inner detectors [23].	- 23 -
3.6	Cutaway view of the ATLAS calorimeter system [23].	- 24 -
3.7	3-dimensional view of the ATLAS muon detectors [24].	- 25 -
3.8	Side view of the ATLAS muon detectors [24].	- 26 -
3.9	Block diagram of the ATLAS trigger system [25].	- 27 -
5.1	Image of the Ξ_b^- and Ω_b^- decay chains.	- 35 -
5.2	p_T (left) and η (right) distributions of the Ω_b^- (top) and Ξ_b^- (bottom) samples before the detector simulation.	- 37 -
5.3	Muon reconstruction efficiency of the J/ψ trigger [33].	- 38 -
5.4	Integrated luminosity as a function of the day in 2011 [34].	- 38 -
5.5	Invariant mass distributions of the combined muon pairs.	- 40 -
5.6	Invariant mass distributions of the combined muon pairs satisfying the quality requirements.	- 41 -
5.7	Invariant mass distributions of the combined muon pairs in the data and the MC samples.	- 42 -

5.8	p_{Tm} , η_m , and ϕ_m distributions of the muons composing the J/ψ candidates.	- 42 -
5.9	χ_m^2 , p_{Tm} , η_m , and ϕ_m distributions of the J/ψ candidates. Those pairs having $\chi_m^2 > 4$ are included in the χ_m^2 distribution.	- 43 -
5.10	dR distributions between the truth J/ψ and the reconstructed J/ψ candidates.	- 44 -
5.11	J/ψ reconstruction efficiencies.	- 45 -
5.12	Invariant mass distributions of the Λ^0 candidates satisfying the quality requirements.	- 47 -
5.13	Illustration of L_{xy} for the Λ^0 analysis.	- 48 -
5.14	L_{xy} distribution of the Λ^0 candidates.	- 49 -
5.15	2-dimensional vertex position distribution of the Λ^0 candidates in the sideband region.	- 49 -
5.16	Invariant mass distributions of the Λ^0 candidates satisfying all requirements in the data and the MC samples.	- 50 -
5.17	χ_n^2 , p_{Tn} , η_n , and ϕ_n distributions of the Λ^0 candidates after the L_{xy} requirement in the signal region.	- 51 -
5.18	dR distributions between the truth Λ^0 and the reconstructed Λ^0 candidates.	- 52 -
5.19	Λ^0 reconstruction efficiencies.	- 53 -
5.20	Λ^0 reconstruction efficiencies in L_{xy} at the truth level.	- 54 -
5.21	Invariant mass distributions of the Ξ^- candidates satisfying the quality requirements.	- 55 -
5.22	Illustration of the pointing angle for the Ξ^- analysis.	- 56 -
5.23	L_{xy} distribution of the Ξ^- candidates.	- 57 -
5.24	$\cos\theta$ distribution of the Ξ^- candidates in the signal region.	- 57 -
5.25	Invariant mass distributions of the Ξ^- candidates satisfying all requirements in the data and the MC sample.	- 59 -
5.26	χ_n^2 , p_{Tn} , η_n , and ϕ_n distributions of the Ξ^- candidates in the signal region.	- 60 -
5.27	2-dimensional invariant mass distribution for the Ξ^- kinematics reflection.	- 61 -
5.28	Invariant mass distributions of the Ω^- candidates satisfying the quality requirements and removing the Ξ^- kinematics reflection.	- 62 -
5.29	L_{xy} distribution of the Ω^- candidates.	- 63 -
5.30	$\cos\theta$ distribution of the Ω^- candidates.	- 63 -
5.31	Invariant mass distributions of the Ω^- candidates satisfying all requirements in the data and the MC sample.	- 65 -

5.32	χ_n^2 , p_{Tn} , η_n , and ϕ_n distributions of the Ω^- candidates in the signal region.	- 66 -
5.33	p_{T0} , η_0 , and ϕ_0 distributions of the proton and pion track parameters used for the refit for the data.	- 68 -
5.34	p_{T0} , η_0 , and ϕ_0 distributions of the proton and pion track parameters used for the refit for the MC sample.	- 69 -
5.35	χ_{pm}^2 distributions of the Λ^0 and Ω^- candidates in the data and the MC sample.	- 70 -
5.36	p_{Tpm} , η_{pm} , and ϕ_{pm} distributions of the Λ^0 and Ω^- candidates after the refit for the data.	- 71 -
5.37	Invariant mass distributions of the Ω_b^- candidates in the data (right) and the MC sample (left) satisfying the quality requirements.	- 72 -
5.38	Illustration of the pointing angle and L_{xy} for the Ω_b^- analysis.	- 73 -
5.39	$\cos\theta$ distributions of the Ω_b^- candidates in the data and the MC sample. -	74 -
5.40	L_{xy} distributions of the Ω_b^- candidates in the data and the MC sample. -	74 -
5.41	Invariant mass distributions of the Ω_b^- candidates satisfying the $\cos\theta$ and L_{xy} requirements.	- 75 -
5.42	Definition of the decay angle.	- 76 -
5.43	$\cos\theta^*$ distributions of the Ω_b^- candidates in the data and the MC sample. -	77 -
5.44	Invariant mass distribution of the final Ω_b^- candidates in the data. . .	- 78 -
5.45	Invariant mass distribution of the Ω_b^- candidates in the MC sample after applying all requirements.	- 78 -
5.46	χ_{pm}^2 distributions of the Λ^0 and Ξ^- candidates in the data and the MC sample.	- 79 -
5.47	Invariant mass distributions of the Ξ_b^- candidates satisfying the quality requirements in the data (right) and the MC sample (left).	- 80 -
5.48	$\cos\theta$ distribution of the Ξ_b^- candidates in the data and the MC sample. -	80 -
5.49	L_{xy} distribution of the Ξ_b^- candidates in the data and the MC sample. -	81 -
5.50	$\cos\theta^*$ distribution of the Ξ_b^- candidates in the data and the MC sample. -	81 -
5.51	Invariant mass distributions of the Ξ_b^- candidates satisfying the $\cos\theta$ and L_{xy} requirements.	- 82 -
5.52	Invariant mass distribution of the Ξ_b^- candidates satisfying all requirements in the data.	- 83 -
5.53	Invariant mass distribution of the Ξ_b^- candidates satisfying all requirements in the MC sample.	- 83 -
6.1	Invariant mass distributions of the Ω_b^- (left) and Ξ_b^- (right) candidates with the fit for the MC samples.	- 85 -

6.2	Invariant mass distributions of the Ω_b^- candidates with the fit for the data.	- 87 -
6.3	Invariant mass distributions of the Ξ_b^- candidates with the fit for the data.	- 87 -
6.4	The J/ψ , Ω^- , and Ξ^- mass distributions from the data (right) and the MC samples (left) with the fitted curves.	- 90 -
6.5	The Ω_b^- masses at each experiment.	- 91 -
6.6	The Ξ_b^- masses at each experiment.	- 91 -
6.7	Distribution of the mass difference for the Ξ_b^{*-} baryon [15].	- 95 -
6.8	Image of a double bottom baryon decay chain.	- 97 -
A.1	Generated p_T (left) and η (right) distributions of the Ω_b^- (top) and Ξ_b^- (bottom) samples.	- 101 -
A.2	Invariant mass distributions of the Λ^0 candidates satisfying the quality requirements in the MC samples.	- 102 -
A.3	L_{xy} distributions of the Λ^0 candidates in the MC samples.	- 102 -
A.4	Invariant mass distributions of the Ω^- (left) and Ξ^- (right) candidates satisfying the quality requirements in the MC samples.	- 103 -
A.5	L_{xy} distributions of the Ω^- (left) and Ξ^- (right) candidates in the MC samples.	- 103 -
A.6	$\cos\theta$ distributions of the Ω^- (left) and Ξ^- (right) candidates in the MC samples.	- 103 -
A.7	dR distributions between the truth Ω^- (left) and Ξ^- (right) and the reconstructed Ω^- and Ξ^- candidates, respectively	- 104 -
A.8	Reconstruction efficiencies in L_{xy} of the Ω^- (left) and Ξ^- (right) candidates.	- 104 -
A.9	Ω^- and Ξ^- reconstruction efficiencies.	- 105 -
A.10	p_T , η , and ϕ distributions of the Ω_b^- candidates in the data (right) and the MC sample (left).	- 106 -
A.11	p_{T0} , η_0 , and ϕ_0 distributions after the refit for the Ξ_b^- candidates (data).- 107 -	
A.12	p_{T0} , η_0 , and ϕ_0 distributions after the refit for the Ξ_b^- candidates (MC).- 108 -	
A.13	p_{Tpm} , η_{pm} , and ϕ_{pm} distributions of the Λ^0 and Ξ^- candidates after the refit.	- 109 -
A.14	p_T , η , and ϕ distributions of the Ξ_b^- candidates in the data (right) and the MC sample (left).	- 110 -
C.1	Invariant mass distributions of the Ω_b^- (left) and Ξ_b^- (right) candidates with the single Gaussian fit in the MC samples.	- 112 -
D.1	Ω_b^- significance in $\cos\theta^*$	- 114 -

D.2	Ξ_b^- significance in $\cos \theta^*$	- 114 -
D.3	Invariant mass distributions of the Ω_b^- (top) and Ξ_b^- (bottom) candidates with the shifted tracks.	- 115 -
D.4	μ distributions of the data and the MC sample.	- 116 -
D.5	Efficiencies in the average μ values.	- 116 -

Chapter 1

Introduction

One of the most successful theory of the twentieth century in elementary particle physics is the Standard Model. In nature, there are four interactions: the weak, electromagnetic, strong, and gravitational interactions, and the Standard Model is able to describe the three interactions except for the gravitational interaction. The four interactions are transmitted by three types of gauge bosons; the W^\pm and Z bosons for the weak interaction, photons for the electromagnetic interaction, and the gluons for the strong interaction. The weak and electromagnetic interactions are based on and unified in the gauge theory of the group $SU(2) \times U(1)$ and the strong interaction is described by that of the gauge group $SU(3)$. The existence of these gauge bosons has been proved by various experiments.

When local gauge invariance is required, all particles need to be massless. To avoid this mathematical property, the spontaneous symmetry breaking of a scalar field is introduced. The scalar field is termed the Higgs field and emerges as a massive particle. This massive particle is the Higgs boson. The Higgs boson had not been observed for a long period, but it was finally discovered with the LHC at CERN in 2012, and the Standard Model strengthens its validity.

A basic theory of hadron physics is described by quantum chromodynamics (QCD) of the strong interaction in the framework of the Standard Model. Hadrons are considered to be bound states of quarks. Therefore, in principle, their properties such as their masses should be determined by QCD. This is, however, not yet a case for light hadrons composed of light quarks (u , d , s) because the effective coupling of the theory increases as the energy scale determined by the hadron masses decreases. On the other hand, properties of heavy hadrons containing one or more heavy quarks (c , b) are better calculable since the perturbative approach is applicable because of their mass setting. Heavy Quark Effective Theory (HQET) [1] and the Constituent Quark Model [2] are good examples of it.

Baryons which include charm quarks are called charmed baryons, and also baryons with bottom quarks are bottom baryons. So far, six out of the sixteen bottom baryon ground-states with one bottom quark have been discovered [3] [4]. Most of them have been observed in the high energy hadron colliders of Tevatron and the LHC. Any double bottom baryons or bottom baryons with charm quarks have not been discovered yet.

Bottom baryons are new particles and their parameters are not measured sufficiently. Indeed QCD of the Standard Model is successful to describe hadron physics, but it still is not enough to evaluate the quality and integrity in the area of heavy hadrons. Therefore, understanding bottom baryons is an essential component in QCD. Furthermore, it plays an important role of accurately estimating $H^0 \rightarrow b\bar{b}$ and other exotic new physics with bottom quarks as bottom hadron production is to be backgrounds for the analyses [5].

In this thesis, bottom baryon production is studied using data taken with the LHC during the entire year of 2011. The theoretical background about bottom baryons is described in the next chapter. Chapter 3 describes the LHC and the ATLAS experiment. In Chapter 4, the method of calculating vertices is described. The reconstruction strategy of the bottom baryons Ω_b^- and Ξ_b^- is detailed in Chapter 5. The results of the mass measurements and the production cross sections are described in Chapter 6. Finally, in Chapter 7, the conclusions are described.

Chapter 2

Theoretical background

2.1 Hadron physics

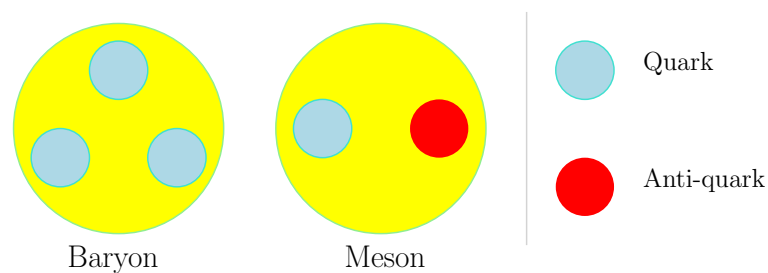


Figure 2.1: Baryon and meson models.

Hadrons are regarded as bound states of some quarks and/or anti-quarks by the strong interaction. Hadrons composed of three quarks are called ‘baryons’ and hadrons composed of one quark and one anti-quark are called ‘mesons’. Figure 2.1 shows a cartoon of a baryon and a meson.

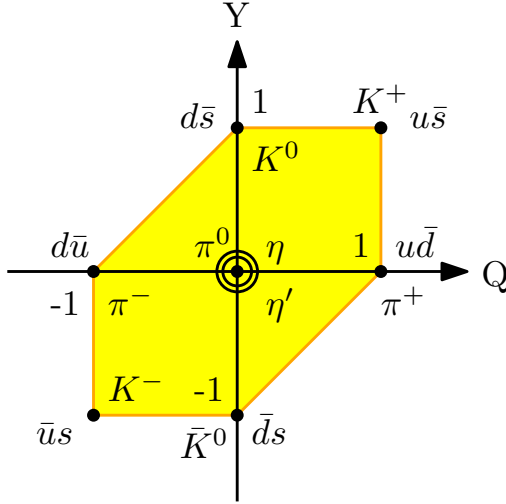
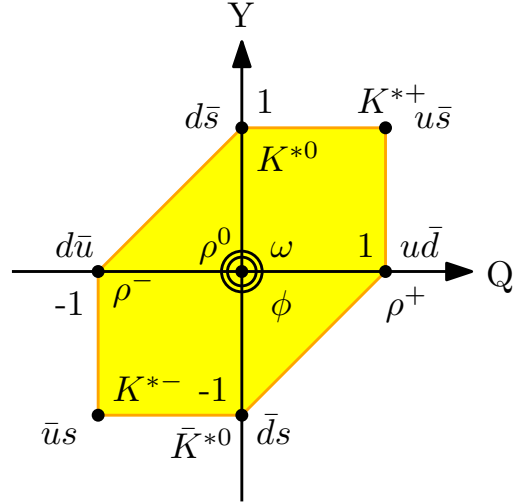
The baryon number of one quark is defined as $\frac{1}{3}$. The number of baryons is 1 and that of mesons is 0. The baryon number is generally conserved during known decays of standard hadrons.

2.1.1 Meson model

A quark spin (s) is $\frac{1}{2}$. Therefore, a ground-state meson spin with zero orbital angular momentum is 1 or 0; $s = 1$ in the case where the directions of the two quarks are the same, and $s = 0$ in the case where those are opposite. The parity operator of mesons is written as

$$P = P_q P_{\bar{q}} (-1)^l. \quad (2.1)$$

Here, a relationship of quarks parity is used ($P_q = -P_{\bar{q}}$). l means the orbital angular momentum quantum number. In the light quark system, u -quarks, d -quarks, and s -quarks are constituent particles of mesons and nine combinations of the two exist. They are nine pseudoscalar mesons ($J(\equiv l + s)^P = 0^-$) and nine vector mesons ($J^P = 1^-$).

Figure 2.2: $J^P = 0^-$ mesons.Figure 2.3: $J^P = 1^-$ mesons.

Figures 2.2 and 2.3 show two types of the nine mesons. x -axis means a charge of the mesons and y -axis means a hypercharge of them. The hypercharge Y is defined as summation of the baryon number B and the strangeness number S , i.e. $Y = B + S$. The strangeness number is the number of anti- s -quarks. The baryon number of mesons is 0, so that y -axis of the figures is identical to the strangeness number. The π^0 and ρ^0 mesons at $Q = Y = 0$ are mixing states of the quark pairs $u\bar{u}$ and $d\bar{d}$. The η , η' , and ω mesons are those of $u\bar{u}$, $d\bar{d}$, and $s\bar{s}$. The ϕ meson is almost a state of the pure pair $s\bar{s}$. The $s\bar{s}$ state of the ω meson has lesser impact on its state, therefore, the ω state is written as $\omega \simeq \sqrt{\frac{1}{2}}(u\bar{u} + d\bar{d})$.

2.1.2 Baryon model

Baryons are composed of three quarks. Therefore, the total angular momentum J of a ground-state baryon with zero orbital angular momentum is $\frac{1}{2}$ or $\frac{3}{2}$. The total wave function must be antisymmetric because of the Pauli exclusion principle as a quark is a fermion. A quark has a color from QCD and all hadrons are colorless. The following color wave function is permitted for baryons:

$$\psi_{color} = \frac{1}{\sqrt{6}}(\text{RGB} - \text{RBG} + \text{GBR} - \text{GRB} + \text{BRG} - \text{BGR}). \quad (2.2)$$

Here, the part ‘RGB’ means that the first quark color is Red, the second is Green, and the third is Blue. Equation (2.2) is antisymmetric under interchanges of the constituent quarks, so that the baryon wave function without the color part should be symmetric under the interchanges. These baryons, which are composed of u , d , and s -quarks, belong to the flavor symmetry group $SU(3)$. The fundamental representation is classified as

$$\mathbf{3} \otimes \mathbf{3} \otimes \mathbf{3} = \mathbf{1} \oplus \mathbf{8} \oplus \mathbf{8} \oplus \mathbf{10}, \quad (2.3)$$

and eighteen combinations among the twenty seven are allowed; the eight baryons with $J = \frac{1}{2}$ and the ten baryons with $J = \frac{3}{2}$. The decuplet is totally symmetric in the interchange of the quarks and therefore the $J = \frac{3}{2}$ baryons satisfy the Pauli exclusion principle. One of the octet baryons has a mixed symmetry, but it forms the symmetric wave function by combining the mixed spin states of the $J = \frac{1}{2}$ baryons. In the end, these baryons are shown in Figures 2.4 and 2.5. The baryons Λ^0 and Σ^0 at $Q = Y = 0$ in Figure 2.4 are the mixing states of the quark trios sud and sdu .

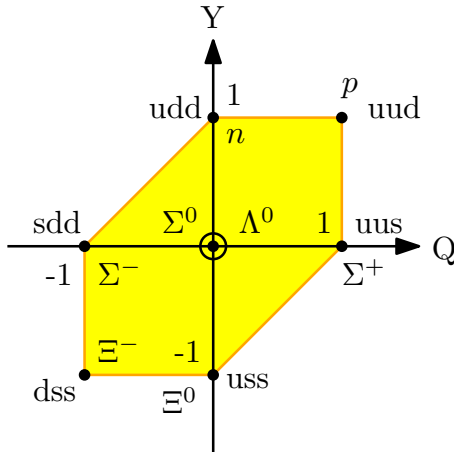


Figure 2.4: Baryon octet.

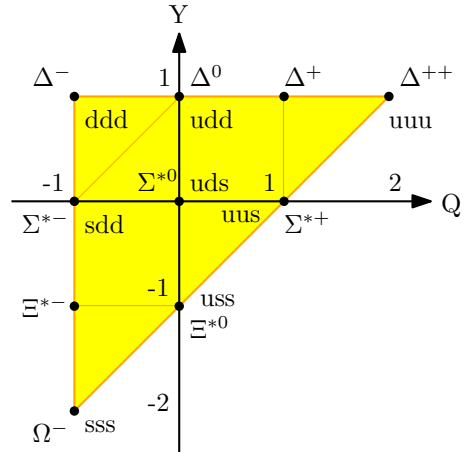


Figure 2.5: Baryon decuplet.

2.2 Bottom baryon model

Bottom baryons that contain one or more bottom quarks but no charm quark can be classified by the $SU(4)$ group analysis similarly to the $SU(3)$ representation of light baryons. The fundamental representation is a quadruplet that is composed of u , d , s , and b -quarks. The multiplet can be classified as

$$\mathbf{4} \otimes \mathbf{4} \otimes \mathbf{4} = \mathbf{4} \oplus \mathbf{20} \oplus \mathbf{20} \oplus \mathbf{20}. \quad (2.4)$$

Considering the Pauli exclusion principle like the previous section, twelve new baryons with bottom quarks should exist in addition to the basic baryon octet and new ten ones should exist in addition to the decuplet. Figures 2.6 and 2.7 show an extended version of Figures 2.4 and 2.5 including the bottom baryons. The bottom surfaces correspond to the octet and the decuplet of Figures 2.4 and 2.5, and z -axis (upper direction) shows the number of bottom quarks.

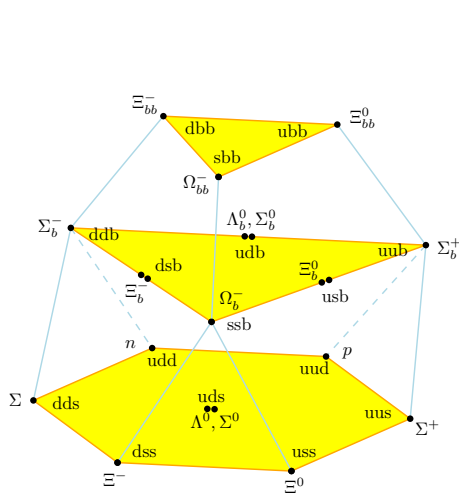


Figure 2.6: Baryon octet extended to the bottom baryons.

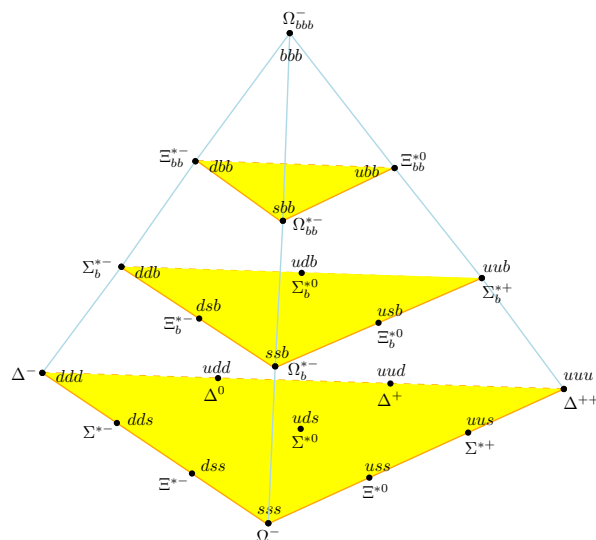


Figure 2.7: Baryon decuplet extended to the bottom baryons.

The $J = \frac{1}{2}$ bottom baryons Λ_b^0 , Σ_b^\pm , Ξ_b^0 , Ξ_b^- , and Ω_b^- and the $J = \frac{3}{2}$ bottom baryons $\Sigma_b^{*\pm}$, Ξ_b^{*0} , and Ξ_b^{*-} have been discovered so far. Excited states of the Λ_b^0 and Ξ_b^- baryons have also been discovered [13]. The first reported one is the Λ_b^0 baryon, which had been observed at the SppS proton-antiproton collider at CERN in 1991 [6]. The searched decay mode was $\Lambda_b^0 \rightarrow J/\psi \Lambda$. Since then, various experiments have observed the Λ_b^0 baryon, and the mass and other parameters have been precisely measured. After the discovery of the Λ_b^0 baryon, any other bottom baryon had not been observed for sixteen years. However, in 2007, the Σ_b^\pm and $\Sigma_b^{*\pm}$ baryons were discovered by the CDF experiment [7] and the Ξ_b^- baryon was discovered by the D0 experiment [8]. The searched decay modes were $\Sigma_b^{\pm,*\pm} \rightarrow \Lambda_b^0 \pi^\pm$ and $\Xi_b^- \rightarrow J/\psi \Xi^-$. A series of discoveries of these new bottom baryons was made possible by high energy collisions of proton-antiproton provided by Tevatron [9]. In 2008, the Ω_b^- baryon through the decay mode of $\Omega_b^- \rightarrow J/\psi \Omega^-$ was discovered by the D0 experiment [10], and in 2011, the Ξ_b^0 baryon was discovered by the CDF experiment through $\Xi_b^0 \rightarrow \Xi_c^+ \pi^-$ [11]. Table 2.1 shows a summary of the bottom baryon masses and the

observation years including the latest particles.

Table 2.1: Bottom baryons listing [13].

Particle	Mass	year
Λ_b^0	5619.5 ± 0.4 MeV	1991
Σ_b^+	5811.3 ± 1.9 MeV	2007
Σ_b^-	5815.5 ± 1.8 MeV	2007
Σ_b^{*+}	5832.1 ± 1.9 MeV	2007
Σ_b^{*-}	5835.1 ± 1.9 MeV	2007
Ξ_b^-	5794.9 ± 0.9 MeV	2007
Ω_b^-	6048.8 ± 3.2 MeV	2008
Ξ_b^0	5793.1 ± 2.5 MeV	2011
Ξ_b^{*0}	$5945.0 \pm 0.7 \pm 0.3 \pm 2.7$ MeV [14]	2012
Ξ_b^{*-}	$5955.33 \pm 0.12 \pm 0.06 \pm 0.50$ MeV [15]	2015

Although these bottom baryons are discovered, there are still a small number of candidates and the properties of the baryons are not yet known. For example, the claimed mass of the Ω_b^- baryon is different between the measurements (CDF: 6054 MeV [12], D0: 6165 MeV [10]). Figure 2.8 shows the measured Ω_b^- mass distributions from three experiments. The top left plot shows the result of D0, the top right plot shows that of CDF, and the bottom plot shows that of LHCb. Although the latest result from LHCb at the LHC supports the CDF result, new measurements are highly awaited for confirmation. Especially, it is interesting to measure the production rate at the LHC energy.

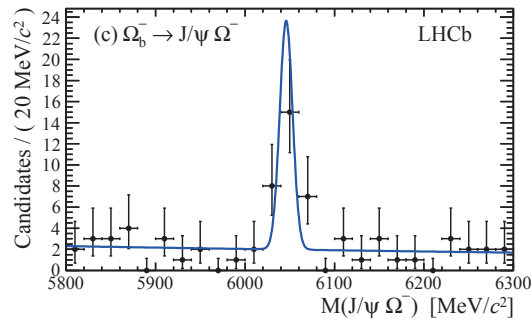
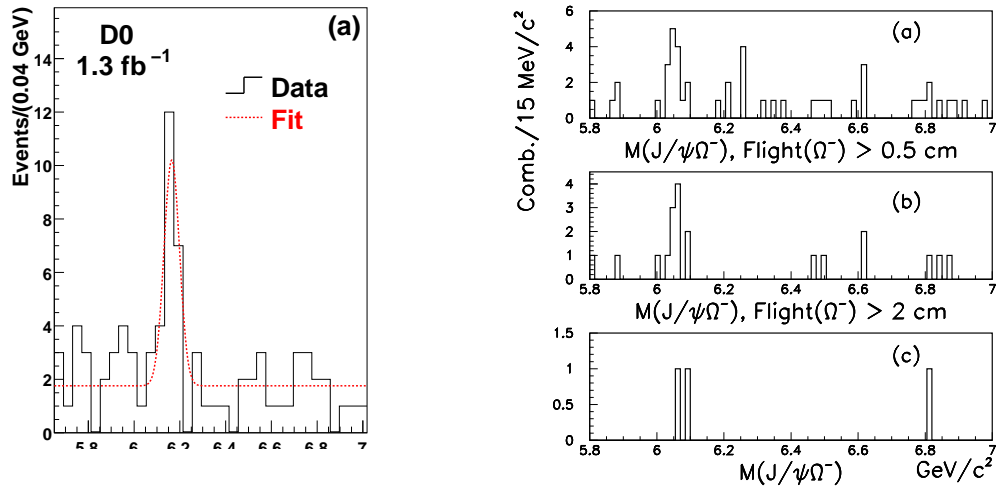


Figure 2.8: Ω_b^- mass distributions at the D0, CDF, and LHCb experiments [4] [10] [12].

Chapter 3

LHC and ATLAS experiment

3.1 Large Hadron Collider

The Large Hadron Collider (LHC) is the largest proton-proton collider in the world, having been built by the European Organization for Nuclear Research (CERN) located near Geneva in Switzerland. The purpose is to explore particle physics at the TeV scale; especially, to prove or disprove the existence of the Higgs boson, and it turned out that the Higgs boson does exist in 2012 [16] [17]. The mass is now determined to be 125.09 GeV by combining the ATLAS and CMS analyses [18].

The LHC is a circular accelerator. The design beam energy is 7TeV ($\sqrt{s} = 14\text{TeV}$) and the design luminosity is $10^{34} \text{ cm}^{-2}\text{s}^{-1}$. Here, \sqrt{s} represents the total center-of-mass energy. To accomplish these performances, main 1232 superconducting dipole magnets cooled to 1.9 K by superfluid helium to provide a magnetic field intensity of 8.33 T are arranged along the ring of 26.6 km in circumference [19]. Figure 3.1 shows an overall view of the LHC and its injectors. The proton beams from the linac are injected to the Proton Synchrotron (PS) via PS-booster to be accelerated to 26 GeV. The beams are then sent to Super Proton Synchrotron (SPS) and accelerated to 450 GeV. Finally, the beams are sent to the LHC ring, accelerated, and stored for collisions. In November 2009, proton beams were circulated and the first proton-proton collisions were recorded with the beam energy of 450 GeV ($\sqrt{s} = 900 \text{ GeV}$). In March 2010, the highest-energy particle collisions with the beam energy of 3.5TeV ($\sqrt{s} = 7\text{TeV}$) were recorded. Table 3.1 shows some values of the LHC design parameters and those of 2011 operation achievements.

Table 3.1: Details of the LHC parameters [21].

	Design	2011
Circumferential length of the ring	27 km	-
Proton beam energy	7 TeV	3.5 TeV
Peak luminosity/cm ⁻² s ⁻¹	10 ³⁴	3.65 × 10 ³³
The number of bunches	2808	1331
Time between bunch crossings	25 nsec	50 nsec
The number of proton particles per bunch	1.2 × 10 ¹¹	1.2 × 10 ¹¹

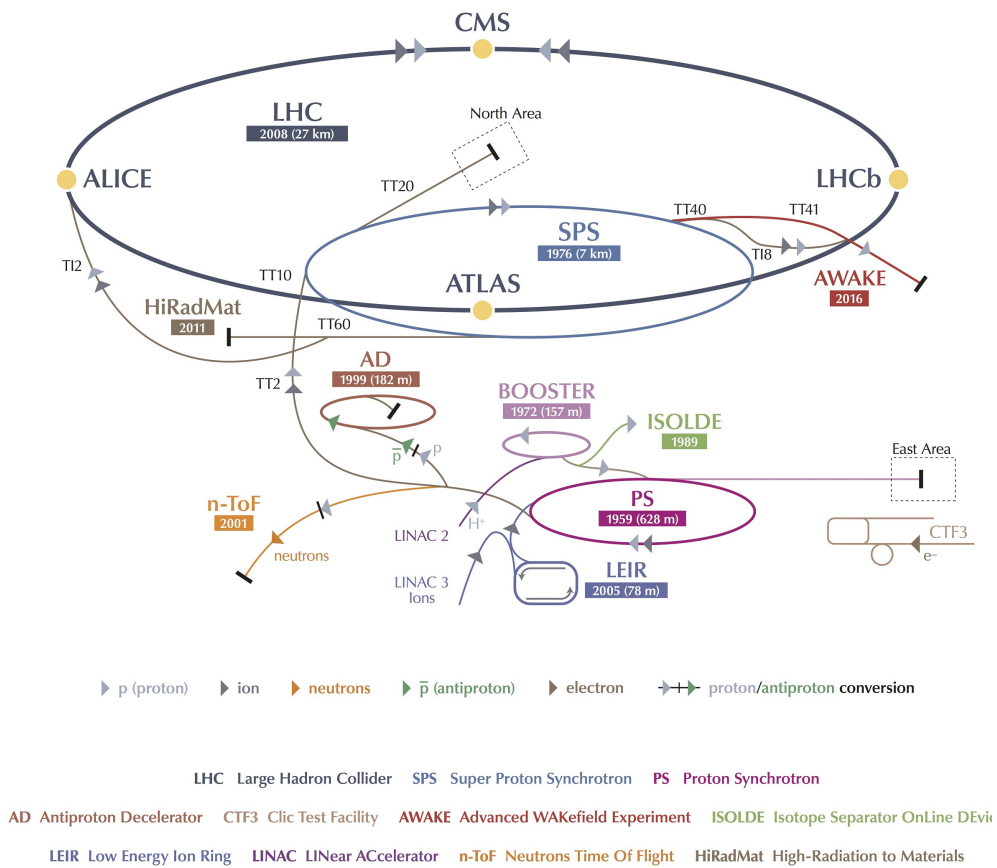


Figure 3.1: Overall view of the LHC and its injectors [20].

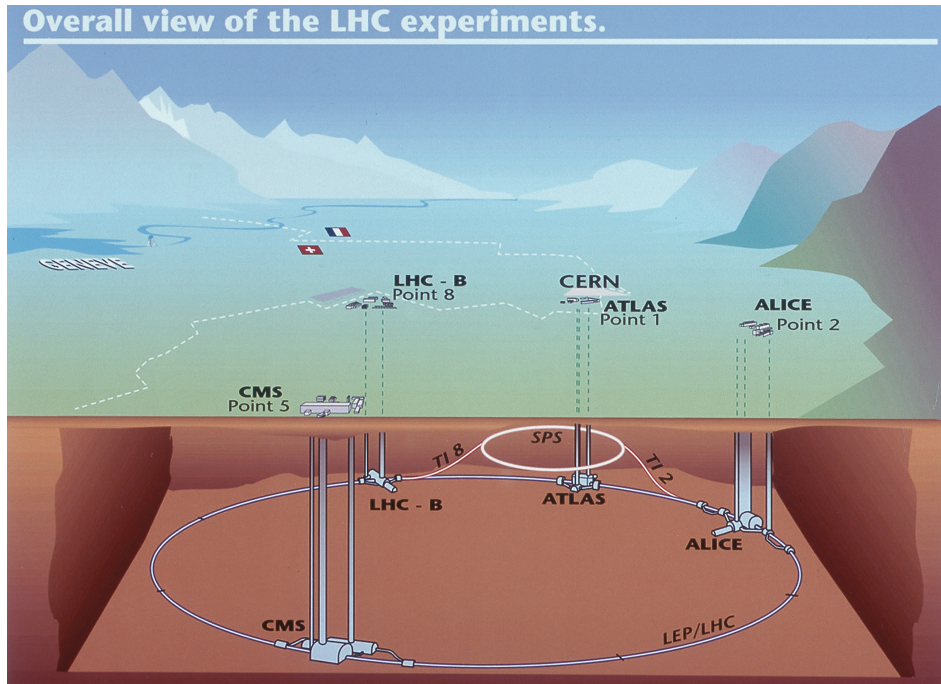


Figure 3.2: Overall view of the LHC experiments [22].

The LHC reuses a tunnel built for the Large Electron-Positron Collider (LEP, operated from 1989 to 2000) located about 100 m below ground. The LHC has four beam collision points, and four large detectors are placed at these collision points. Two of them are general-purpose particle physics detectors: ATLAS (A Toroidal LHC ApparatuS) and CMS (the Compact Muon Solenoid). The others are ALICE (A Large Ion Collider Experiment) and LHCb (Large Hadron Collider beauty). ALICE is a detector for heavy-ion (Pb-Pb) collisions, and LHCb aims for precise measurements of b -hadrons, especially on their CP violations. Figure 3.2 shows the locations of the four detectors.

3.2 ATLAS Detector

Figure 3.3 shows a cutaway view of the ATLAS detector. Its diameter is 25m, length is 44m, and all-up weight is 7000t. The inner track detectors, the calorimeters, and the muon track detectors are placed from the inside to the outside. The ATLAS detector is the largest detector in the world for collider physics and it is able to measure signals of electrons, muons, hadron jets, and missing transverse energy precisely under a severe high-luminosity condition.

The ATLAS detector adopts a right-handed coordinate system of which the z -axis is defined along the beam direction. The x -axis is defined to be the direction from the

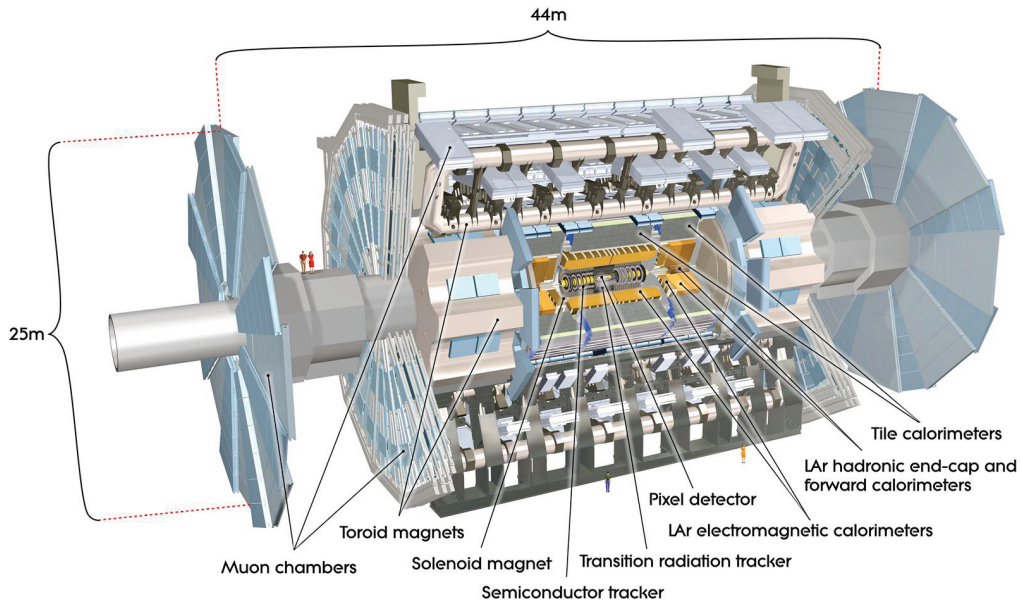


Figure 3.3: Cutaway view of the ATLAS detector [23].

interaction point to the center of the LHC ring and the y -axis points upward. A polar coordinate system is also frequently used, in which the polar angle θ is measured from the z -axis and the azimuthal angle ϕ is defined as $x = r \sin \phi$ and $y = r \cos \phi$ with $r^2 = x^2 + y^2$.

The rapidity y is defined by the energy E and the longitudinal momentum $p_{\parallel} = p_z$ of a particle:

$$y \equiv \frac{1}{2} \ln \left(\frac{E + p_{\parallel}}{E - p_{\parallel}} \right) = \ln \left(\frac{E + p_z}{\sqrt{p_T^2 + m^2}} \right), \quad (3.1)$$

where, m denotes the mass and p_T is the transverse momentum ($p_T \equiv \sqrt{p_x^2 + p_y^2}$). When the particle mass is negligible compared to the momentum, the pseudo-rapidity η is often used instead of the rapidity. The pseudo-rapidity is defined by the $m \rightarrow 0$ limit of the rapidity as

$$\eta = \frac{1}{2} \ln \frac{p + p_z}{p - p_z} = - \ln \left(\tan \frac{\theta}{2} \right). \quad (3.2)$$

The barrel region of the detector covers an angular region of $|\eta| < 1.05$ and the end-cap regions cover $|\eta| > 1.05$. The whole ATLAS detector covers a wide range of η up to 4.5 and the full azimuthal angle.

3.2.1 Magnet systems

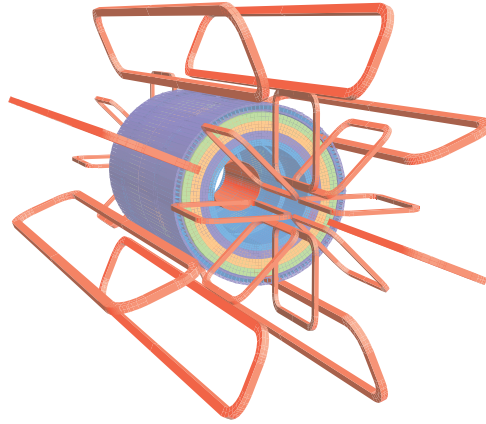


Figure 3.4: Geometry of the ATLAS magnet windings [23].

A large magnet system is incorporated in the ATLAS detector for precise measurements of charged particle momenta. Figure 3.4 shows a geometry of the ATLAS magnet windings. The ATLAS magnet system is composed of one solenoidal magnet located at the center of the detector and three sets of toroidal magnets around the calorimeters. All of them are superconducting magnets. The toroidal magnets are arranged to be an eight-fold azimuthal symmetry and generate an integrated magnetic field of 2 to 6 Tm at the barrel region and 4 to 8 Tm at the end-cap regions. The solenoidal magnet is arranged to cover the inner track detectors and generate an integrated magnetic field of 2 T at the center. Using a curvature of charged particles by the magnetic forces, the momenta are measured.

3.2.2 Inner detectors

The inner detector are located in the magnetic field produced by the solenoid magnet. Figure 3.5 shows a cutaway view of the inner detectors. They cover the pseudorapidity range of $|\eta| < 2.5$. From the inside to the outside, pixel detectors, Semi-Conductor Trackers (SCTs), and Transition Radiation Trackers (TRTs) are arranged. They measure the trajectories of charged particles in the magnetic field to obtain their momentum information.

- Pixel detectors:

The pixel detectors are located at the most interior of the ATLAS detector with different arrangements in the barrel and end-cap regions to provide three measurement points for each particle produced inside the coverage. The pixel

detectors have a high resolution ability to measure the produced vertices of charged particles. The size of one pixel is $50 \mu\text{m} \times 300 \mu\text{m}$ in the z and ϕ directions. The pixel detectors are placed very close to the interaction point, so that the occupancy is decreased by exploiting a benefit of ‘pixelated’ detectors. The tracking resolution near the interaction point is $10 \mu\text{m}$ in $r\phi$ and $115 \mu\text{m}$ along the z direction.

- SCT:

SCT is composed of long and thin microstrip silicon sensors arranged in parallel rows. The distance between the strips is $80 \mu\text{m}$. In each layer, the two sensors are paired and tilted with 40 mrad to allow a 2-dimensional position determination. The sensors are arranged in four cylindrical layers in the barrel region, and nine disks in each end-cap region. The position resolution is $17 \mu\text{m}$ in $r\phi$ and $580 \mu\text{m}$ along z in the barrel region, and $17 \mu\text{m}$ in $r\phi$ and $580 \mu\text{m}$ in r in the end-cap region.

- TRT:

TRT is composed of thirty-six layers of thin straw tube detectors covering a radius of 4 mm . TRT has the capability of identifying electrons by detecting X-rays of the transition radiations. TRT provides only $r\phi$ information with the resolution of $130 \mu\text{m}$.

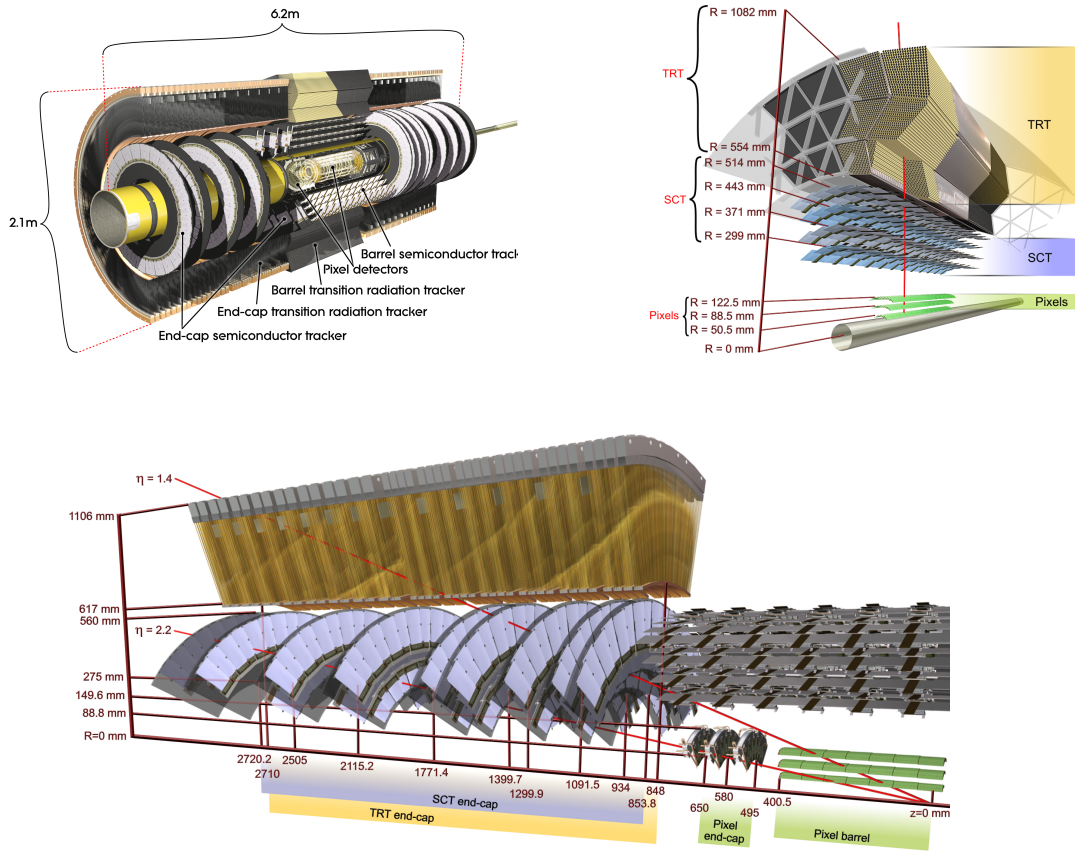


Figure 3.5: Cutaway view of the ATLAS inner detectors [23].

3.2.3 Calorimeters

The energies of electrons, photons, and hadrons are measured with calorimeters. Figure 3.6 shows a cutaway view of the ATLAS calorimeter system. The calorimeters cover the pseudorapidity range of $|\eta| < 4.9$. They are located at the outside the solenoid magnet and longitudinally divided into electromagnetic and hadron calorimeters. The electromagnetic calorimeters measure energies and positions of electrons and photons. The hadron calorimeters surround the electromagnetic calorimeters and measure the energy of hadrons.

- Electromagnetic calorimeter:

The ATLAS electromagnetic calorimeter is composed of accordion-shaped lead absorbers and liquid argon as the active detection material. It has good radiation resistance and covers all regions, i.e., the barrel region and the end-cap

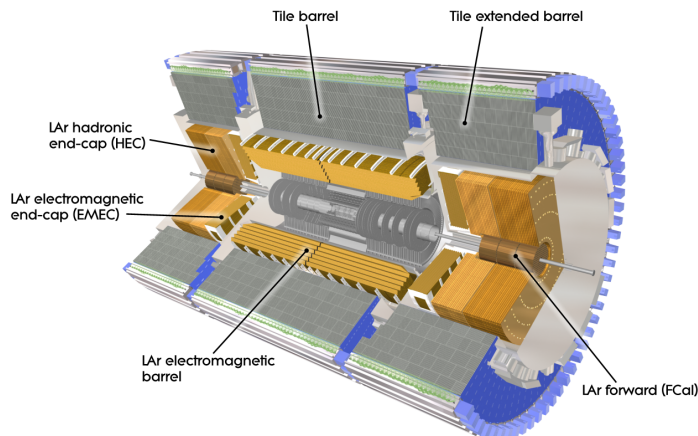


Figure 3.6: Cutaway view of the ATLAS calorimeter system [23].

regions. The energy resolution is expressed as a function of the energy E [GeV] in the following formula,

$$\frac{\Delta\sigma_E}{E} = \frac{9.5\%}{\sqrt{E}} \oplus 0.7\%, \quad (3.3)$$

where \oplus denotes the quadratic sum of the terms. The first term comes from statistical fluctuation of shower tracks and the second constant term mainly comes from an accuracy of the calibration.

- Hadronic calorimeter:

Compositions of the hadron calorimeter are different in each region. The barrel calorimeters are composed of iron absorbers and tiled plastic scintillators, while the end-cap calorimeters are composed of copper absorbers and liquid argon to preserve a good radiation resistance. The tungsten absorbers are also used in a foremost part of the end-cap regions, where higher energy particles are to be measured. The energy resolution is parameterized in the following formulae:

$$\frac{\Delta\sigma_E}{E} = \frac{52.3\%}{\sqrt{E}} \oplus 1.7\% \quad (\text{Barrel}), \quad (3.4)$$

$$\frac{\Delta\sigma_E}{E} = \frac{62.4\%}{\sqrt{E}} \oplus 3.6\% \quad (\text{End-Cap}). \quad (3.5)$$

3.2.4 Muon detectors

The muon lifetime is long and it seldom interacts with materials compared to other charged particles. Therefore, muons pass through the hadronic and electromagnetic

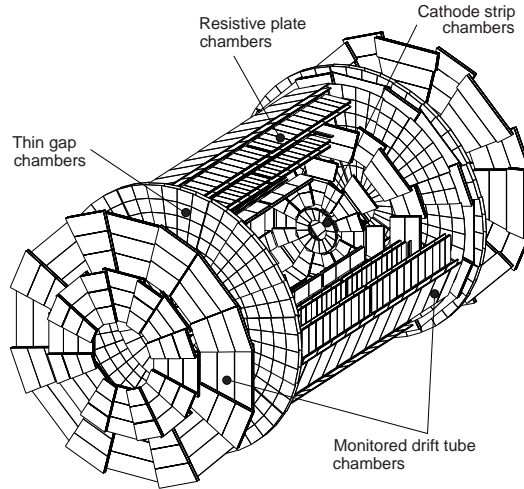


Figure 3.7: 3-dimensional view of the ATLAS muon detectors [24].

calorimeters of the ATLAS detector. The muon detectors are located outside all the other detectors to detect penetrated muons. Figures 3.7 and 3.8 show the ATLAS muon detectors. The muon detector system is composed of two types of detectors. One is used for generating trigger signals and the other is used for the position measurements. The former are Resistive Plate Chambers (RPCs) and Thin Gap Chambers (TGCs), and the latter are Monitored Drift Tubes (MDTs) and Cathode Strip Chambers (CSCs). RPCs are located in the barrel region and TGCs in the end-cap region. MDTs are placed in both barrel and end-cap regions with three stations to measure muon momenta. CSCs are located in a foremost part of the end-cap region to measure positions and angles of muons before entering into the end-cap toroidal magnets. The muon detectors cover the pseudorapidity range of $|\eta| < 2.7$ for the momentum measurements and $|\eta| < 2.4$ for the triggers.

- RPC:

RPC is a parallel plate gas chamber without wires for the anode, in which the $C_2H_2F_4$ gas is filled between bakelite boards. The applied electric field between the boards is kept to a few kV/mm to produce spark-like signals in the passages of charged particles. The signals are read out from metal strips attached outside the bakelite boards. The strips in the two sides are arranged to be perpendicular to each other to provide a 2-dimensional measurement.

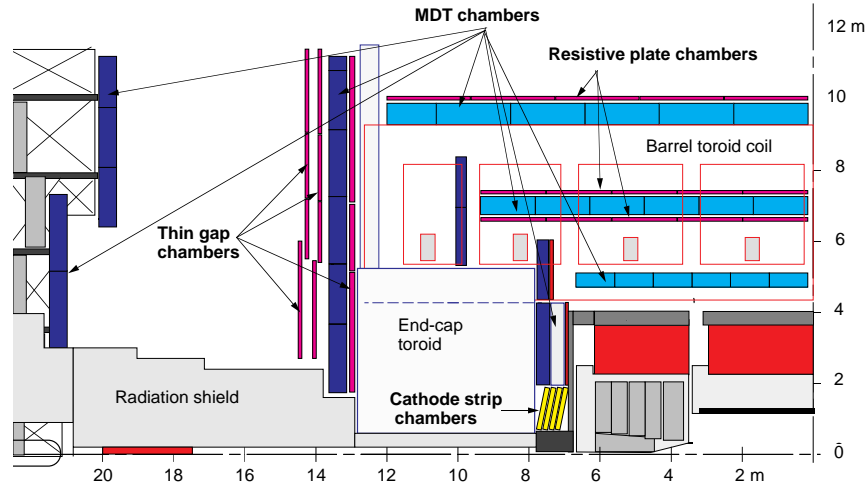


Figure 3.8: Side view of the ATLAS muon detectors [24].

- **TGC:**
TGC is a ‘Thin’ Multiwire Proportional Chamber (MWPC) filled with a mixed gases of CO_2 and n-Pentane. The applied electric field is 3000 V. Tungstenic wires with a radius of $25 \mu\text{m}$ are used as the anodes. The interval of the wire is 1.8 mm. Glass epoxy boards of carbons with the electrical resistance $1 \text{ M}\Omega$ are used as the cathodes. A 2-dimensional measurement is achieved by the readout of signals from the anode wires and metal strips attached outside the carbon cathodes. The position resolution is about 1 cm. Chambers composing TGC have a trapezoidal shape to cover the end-cap regions. The size of the chambers ranges from $1 \text{ m} \times 1 \text{ m}$ to $2 \text{ m} \times 2 \text{ m}$.
- **MDT:**
MDT is composed of six or eight layers of drift tubes with a radius of 15 mm. They are fastened on to a rigid frame. The filled gases is a composition of Ar and CO_2 under a pressure of 3 atm. An electric field of 3270 V is applied to the anode wire string at the center of each tube. The position resolution is $80 \mu\text{m}$ and the maximum drift time is 500 ns.
- **CSC:**
CSC is a cathodic readout MWPC. The distance between the wires is 2.5 mm and the distance between the strips is 5.3mm or 5.6mm. The position resolution is $60 \mu\text{m}$ and the maximum drift time is 30 ns. The filled gases is a composition of Ar, CO_2 , and CF_4 under a pressure of 3 atm with an anode voltage of 2600 V. CSCs are located in a foremost part of the end-cap regions corresponding to $2.0 < |\eta| < 2.7$, because CSC has a low sensitivity to neutrons and photons

which disturb the muon measurement.

3.3 Trigger system

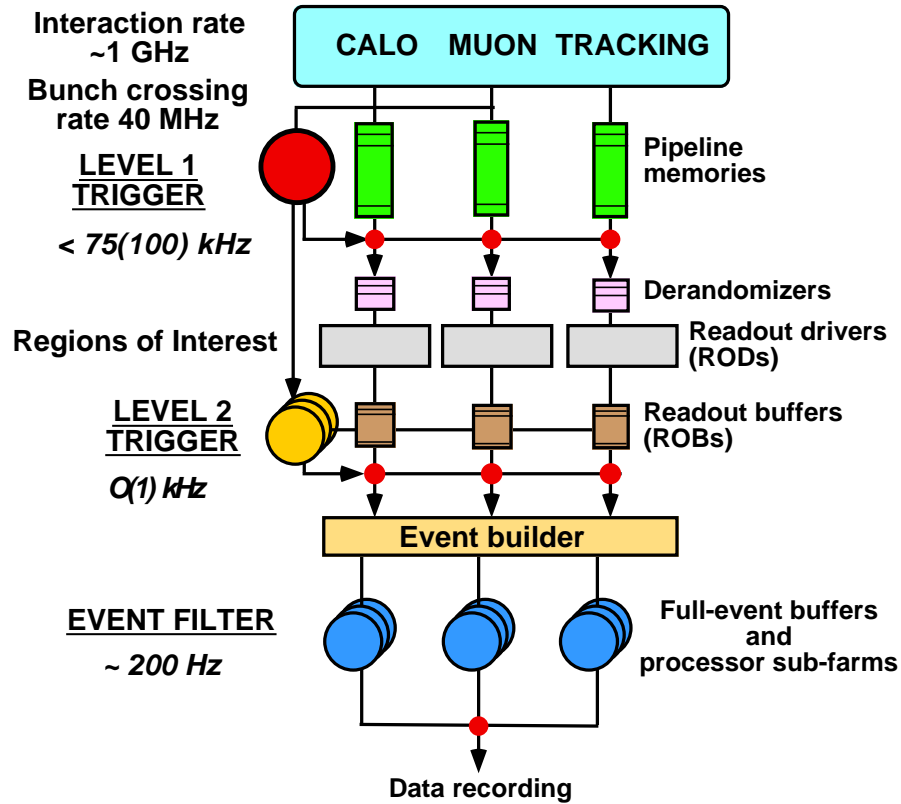


Figure 3.9: Block diagram of the ATLAS trigger system [25].

On average, about twenty proton-proton collisions occur at each 40 MHz beam crossing in the design luminosity of the LHC. This corresponds to about 1 GHz proton-proton collisions. Therefore, it is important to select targeted physics events very effectively. Figure 3.9 shows a block diagram of the ATLAS trigger system.

The trigger system is composed of three levels of triggers, and the trigger rate is reduced at each step. The steps are called as, ‘Level-1 trigger’, ‘Level-2 trigger’, and ‘Event Filter’. A task of the Level-1 trigger is to make a decision whether to start the readout or not, that of the Level-2 trigger is to make a decision whether to start an event building, and that of the Event Filter is to make decision whether to save the event.

- Level-1 trigger:

The decision in the Level-1 trigger to each bunch crossing is mainly performed

by using the information from the muon detectors and the calorimeters, to catch high- p_T muons, electrons/photons, jets, or transverse missing momentum. After receiving the trigger signals, triggered data of each event are collected on the Read Out Driver (ROD) and transferred to the Read Out Buffer (ROB). The location information of the trigger signal sources, which is called Region of Interest (RoI), is transferred to the Level-2 trigger. Here, the maximum trigger rate is reduced to 100 kHz.

- Level-2 trigger:

The Level-2 trigger is a software-base trigger performed in a computer form. The detector regions which should be examined are narrowed by using RoI transferred from the Level-1 trigger. Momenta and positions of the objects detected by the Level-1 trigger are recalculated in accordance with detailed information from the read-out data. At this stage, inner detectors information within RoI is available for reconstructing charged particle tracks. The decision of the Level-2 trigger is carried out using the result of the reconstruction. At this step, the trigger rate is reduced to a few kHz.

- Event Filter:

The event information which passed through the Level-2 trigger is transferred to the Event Filter after the event building. The Event Filter is also software-based. The decision of the Event Filter is carried out using the complete information from the whole detectors. Contrary to the Level-2 trigger, only the information in RoI is available. Conclusions of the information from different detector components are re-examined to identify interesting objects in each event. At this step, the trigger rate is finally reduced to about 200 Hz, to record the entire event data for effective analyses.

Chapter 4

Track parameters and vertex fit

Charged particle trajectories are reconstructed as helical tracks in the solenoidal magnetic field, to obtain their 3-dimensional momentum information. An appropriate assumption of the production vertex improves the reconstruction performance. For particles produced promptly, the production vertex is identical to the beam-beam collision point. However, such an assumption is not appropriate for decay products of long-lived particles that are considered in this analysis. The decay vertices, i.e., the production vertices of the decay products may be displaced from the collision point. The decay vertices are obtained from a simultaneous fit of the decay particle trajectories in the present study in order to optimize the momentum resolution for measured particles. Therefore, the vertex fit plays an important role in the analysis.

4.1 Track parameters

4.1.1 Parameterization of helical motion

The trajectory of charged particles in a magnetic field can be obtained by solving an equation,

$$\frac{\partial}{\partial t} \left(m\gamma \frac{\partial \vec{r}}{\partial t} \right) = kc^2 q \vec{v}(t) \times \vec{B}(\vec{r}), \quad (4.1)$$

where $\vec{B}(\vec{r})$ is the magnetic field, \vec{r} is a position of the particle, \vec{v} is the particle velocity, q is the signed charge, m is the rest mass, c is the velocity of light, t is the time, γ is the relativistic Lorentz factor, and k is the proportionality factor. In the ATLAS inner detector, the magnetic field $\vec{B}(\vec{r})$ is almost parallel to the z -axis, so that the charged particle follows a spiral path (helix) in it. Therefore, the solution

of the above equation can be described as [26]

$$x(l) = x(0) + R_H \left\{ \cos \left(\Phi(0) + \frac{hl \sin \Theta}{R_H} \right) - \cos \Phi(0) \right\}, \quad (4.2)$$

$$y(l) = y(0) + R_H \left\{ \sin \left(\Phi(0) + \frac{hl \sin \Theta}{R_H} \right) - \sin \Phi(0) \right\}, \quad (4.3)$$

$$z(l) = z(0) + l \cos \Theta. \quad (4.4)$$

Here, $\Theta = \sin^{-1} \left(\frac{\partial z}{\partial l} \right)$, $R_H = \frac{p \sin \Theta}{|kqB|}$, and $h = -\text{sign}(qB_z)$. Equations (4.2), (4.3), and (4.4) denote the so-called parameterization of a helical motion in a global coordinate system. If the trajectory of a particle at the perigee is close enough to the origin, Equations (4.2), (4.3), and (4.4) can be written as the second order Taylor expansion around the perigee [26],

$$x \simeq -d_0 \sin \phi_0 + (l \sin \theta_0) \cos \phi_0 + \frac{l^2 \sin^2 \theta_0}{2hR_H} \sin \phi_0, \quad (4.5)$$

$$y \simeq d_0 \cos \phi_0 + (l \sin \theta_0) \sin \phi_0 - \frac{l^2 \sin^2 \theta_0}{2hR_H} \cos \phi_0, \quad (4.6)$$

$$z \simeq z_0 + l \cos \theta_0, \quad (4.7)$$

where variables denoted by the index 0 represent the values at the perigee and d_0 represents the transverse impact parameter to the z -axis.

4.1.2 Five track parameters

Five track parameters are necessary to define a track as can be expected from the discussion in the previous subsection. The five variables are following:

- $\frac{q}{p}$: the charge over the momentum magnitude at the perigee.
- θ_0 : the polar angle at the perigee.
- ϕ_0 : the azimuthal angle at the perigee.
- z_0 : the z coordinate of the perigee.
- d_0 : the transverse impact parameter at the perigee.

These parameters are usually called the perigee parameters, and they can be calculated from Equations (4.5), (4.6), and (4.7). Introducing the parameters, $L_0 \equiv$

$l_0 \sin \theta_0$ and $R_V \equiv y_V \cos \phi_V - x_V \sin \phi_V$, the perigee parameters can be obtained as the following functions:

$$\phi_0 = \phi_V - \frac{L_0}{hR_H}. \quad (4.8)$$

$$z_0 = z_V - L_0 \cot \theta_0. \quad (4.9)$$

$$d_0 = R_V + \frac{L_0^2}{2hR_H}. \quad (4.10)$$

Here, the variables denoted by the index V represent values at the origin V . Note that $\frac{q}{p}$ and θ_0 do not change when going from V to the perigee.

4.2 Vertex fit

4.2.1 Fit procedure

The five (5-dimensional) track parameters, \mathbf{q}_i described in the previous section and their weight matrix W_i at the perigee obtained by individual track fits are used for the 3-dimensional vertex fit. If a particle is originated from a vertex \vec{V} , its track parameters \mathbf{q}_i are able to be expressed as a function of the vertex position \vec{V} and the modified particle momentum \vec{p}_i at the vertex. To find \vec{V} and \vec{p}_i , minimization of the following equation for χ^2 is required:

$$\chi^2 = \sum_{i=1}^{N_{\text{tracks}}} (\mathbf{q}_i - \mathbf{T}(\vec{V}, \vec{p}_i))^T W_i (\mathbf{q}_i - \mathbf{T}(\vec{V}, \vec{p}_i)). \quad (4.11)$$

Here, $\mathbf{T}(\vec{V}, \vec{p}_i)$ means trajectory parameters at a birthplace of the particle: $\mathbf{q}'_i = \mathbf{T}(\vec{V}, \vec{p}_i)$. If $\mathbf{T}(\vec{V}, \vec{p}_i)$ is linearly related to the variations $\delta\vec{V}$ and $\delta\vec{p}_i$ around the first approximation \vec{V}_0 and \vec{p}_{0i} , $\mathbf{T}(\vec{V}, \vec{p}_i)$ can be written as follows:

$$\mathbf{T}(\vec{V}, \vec{p}_i) = \mathbf{T}(\vec{V}_0 + \delta\vec{V}, \vec{p}_{0i} + \delta\vec{p}_i) = \mathbf{T}(\vec{V}_0, \vec{p}_{0i}) + D_i \delta\vec{V} + E_i \delta\vec{p}_i. \quad (4.12)$$

Here, $D_i \equiv \frac{\partial \mathbf{T}(\vec{V}, \vec{p}_i)}{\partial \vec{V}}$ and $E_i \equiv \frac{\partial \mathbf{T}(\vec{V}, \vec{p}_i)}{\partial \vec{p}_i}$ are matrices of the derivatives. Then, Equation (4.12) can be written as

$$\chi^2 = \sum_{i=1}^{N_{\text{tracks}}} (\delta\mathbf{q}_i - D_i \delta\vec{V} - E_i \delta\vec{p}_i)^T W_i (\delta\mathbf{q}_i - D_i \delta\vec{V} - E_i \delta\vec{p}_i), \quad (4.13)$$

where $\delta\mathbf{q}_i = \mathbf{q}_i - \mathbf{T}(\vec{V}_0, \vec{p}_{0i})$. To minimize Equation (4.13), $\frac{\partial\chi^2}{\partial\vec{V}} = 0$ and $\frac{\partial\chi^2}{\partial\vec{p}_i} = 0$ are required, and the system of equations for $\delta\vec{V}$ and $\delta\vec{p}_i$ are derived:

$$\left(\sum_{i=1}^{N_{\text{tracks}}} D_i^T W_i D_i \right) \delta\vec{V} + \sum_{i=1}^{N_{\text{tracks}}} (D_i^T W_i E_i) \delta\vec{p}_i = \sum_{i=1}^{N_{\text{tracks}}} D_i^T W_i \delta\mathbf{q}_i, \quad (4.14)$$

$$(E_i^T W_i D_i) \delta\vec{V}_i + (E_i^T W_i E_i) \delta\vec{p}_i = E_i^T W_i \delta\mathbf{q}_i. \quad (4.15)$$

Now, the vertex position \vec{V} is equal to $\vec{V}_0 + \delta\vec{V}$ and the modified particle momentum \vec{p}_i equal to $\vec{p}_{0i} + \delta\vec{p}_i$, so that a goal of the fit is to solve the above equations and the solution of $\delta\vec{V}$ is [27]

$$\delta\vec{V} = \left(A - \sum_{i=1}^{N_{\text{tracks}}} B_i C_i^{-1} B_i^T \right)^{-1} \left(F - \sum_{i=1}^{N_{\text{tracks}}} B_i C_i^{-1} U_i \right), \quad (4.16)$$

where

$$A \equiv \sum_{i=1}^{N_{\text{tracks}}} D_i^T W_i D_i, B_i \equiv D_i^T W_i E_i, C_i \equiv E_i^T W_i E_i,$$

$$F \equiv \sum_{i=1}^{N_{\text{tracks}}} D_i^T W_i \delta\mathbf{q}_i, U_i \equiv E_i^T W_i \delta\mathbf{q}_i.$$

$\delta\vec{p}_i$ is able to be obtained by substituting $\delta\vec{V}$ back into Equation (4.15).

If the first approximation of \vec{V}_0 is far from the fitted vertex, the track parameters should be extrapolated to the fitted point, all derivatives recalculated, and all fit procedures repeated. The weight matrices W_i should also be translated to the new vertex position [28]. This method is completely the same as the Kalman filter based approach.

4.2.2 Fit constraint

The vertex fit procedure without constraints is explained in Subsection 4.2.1. In this subsection, a vertex fit procedure with constraints on some variables is explained.

It is beneficial to impose some constraints in order to obtain more precise vertex positions and particle momenta. For example, when tracks are originating from well-known particles, a particle mass constraint is often imposed. The vertex fit with constraint $A_j(\vec{V}, \vec{p}_1, \dots, \vec{p}_n) = \text{Const.}$ is executed by using the Lagrange multipliers method, i.e., using the following modified χ^2 definition:

$$\chi^2 = \chi_0^2 + \sum_j \lambda_j A_j^2. \quad (4.17)$$

Here, χ_0^2 is given by Equation (4.13), and λ_j denotes the Lagrange multiplier. If A_j^2 can be linearized around the point $(\vec{V}_0, \vec{p}_{0i})$ which is the solution without the constraints (i.e. the case $\chi^2 = \chi_0^2$), the above equation can be rewritten as

$$\chi^2 = \chi_0^2 + \sum_j \lambda_j (A_{j0}^2 + H_j^T \delta V + \delta V^T H_j + F_{ij}^T \delta p_i + \delta p_i^T F_{ij}), \quad (4.18)$$

where $H_j = \frac{\partial A_j}{\partial \vec{V}}$, $F_{ij} = \frac{\partial A_j}{\partial \vec{p}_i}$, $A_{j0} = A_j(\vec{V}_0, \vec{p}_{0i})$, $\delta \vec{V} = \vec{V} - \vec{V}_0$, and $\delta \vec{p}_i = \vec{p}_i - \vec{p}_{0i}$. To solve Equation (4.18), minimization of χ^2 is carried out in the same way as the case without constraints by substituting $\vec{V} = \vec{V}_0 + \vec{V}_1$ and $\vec{p}_i = \vec{p}_{0i} + \vec{p}_{1i}$. The term \vec{V}_1 is the second part of the solution and can be obtained from the following relational expression [28]:

$$\vec{V}_1 = - \sum_j \lambda_j C_{\text{cov}} L_j, \quad (4.19)$$

where

$$\begin{aligned} \lambda_j &= M_j \left(\sum_i F_{ij}^T C_i^{-1} F_{ij} + L_j^T C_{\text{cov}} L_j \right)^{-1}, \\ L_j &= \sum_i B_i C_i^{-1} F_{ij} - H_j, \\ M_j &= A_{j0}^2 - H_j^T \vec{V}_0 - \sum_i F_{ij}^T \vec{p}_{0i}, \\ C_{\text{cov}} &= \left(K - \sum_i B_i C_i^{-1} B_i^T \right)^{-1}, \\ K &= \sum_i D_i^T W_i D_i. \end{aligned}$$

The definitions of the matrices B_i and C_i are the same as those in Subsection 4.2.1, and \vec{p}_{1i} can be obtained in the same way. The vectors \vec{V}_0 and \vec{p}_{0i} are already solved in the previous subsection, so that a goal of the fit with constraints is accomplished as $\vec{V} = \vec{V}_0 + \vec{V}_1$ and $\vec{p}_i = \vec{p}_{0i} + \vec{p}_{1i}$.

In this analysis, the calculations of the vertex fit are executed using a tool in the ATLAS software framework [28]. The details of the actual application are described in the next chapter for the event reconstruction.

Chapter 5

Event reconstruction

5.1 Decay kinematics

The muon lifetime is long and it penetrates dense materials since it does not feel the strong force, i.e., the particle is clear enough to identify. In addition, the ATLAS detector has a good trigger efficiency on muons. Therefore, decay modes including muons in the final state are suitable for studies of bottom baryons. The target decay modes in the present analysis are

$$\begin{aligned}\Omega_b^- &\rightarrow J/\psi + \Omega^-, \\ J/\psi &\rightarrow \underline{\mu^+} + \underline{\mu^-}, \quad \Omega^- \rightarrow \Lambda^0 + \underline{K^-}, \\ &\quad \Lambda^0 \rightarrow \underline{p} + \underline{\pi^-},\end{aligned}$$

for the Ω_b^- baryon, and

$$\begin{aligned}\Xi_b^- &\rightarrow J/\psi + \Xi^-, \\ J/\psi &\rightarrow \underline{\mu^+} + \underline{\mu^-}, \quad \Xi^- \rightarrow \Lambda^0 + \underline{\pi^-}, \\ &\quad \Lambda^0 \rightarrow \underline{p} + \underline{\pi^-}.\end{aligned}$$

for the Ξ_b^- baryon. The five charged particles denoted by underlines are the objects to be observed. The three particles other than the two muons can be distinguished by identifying the parent hadrons having a long lifetime. The vertex fit described in Chapter 4 is used to identify these cascade decays. An image of these decays are illustrated in Figure 5.1. The Ω_b^- or Ξ_b^- baryon is produced by a pp collision at the collision point. The produced bottom baryon decays with a lifetime of $O(\text{ps})$ [3] to the J/ψ meson and the Ω^-/Ξ^- baryon. The J/ψ meson immediately decays to a $\mu^+\mu^-$ pair and the muons are observed by the muon detectors. The Ω^-/Ξ^- baryon decays

to the Λ^0 baryon and the K^-/π^- meson with $c\tau = 2.461\text{ cm}/4.91\text{ cm}$ [3]. Here, the K^-/π^- meson can be detected by the inner detectors. Finally, the Λ^0 baryon decays to the proton and the pion with $c\tau = 7.89\text{ cm}$ [3] and they can also be observed by the inner detectors. Table 5.1 summarizes the masses and $c\tau$ values of the participating particles and Table 5.2 summarizes the relevant branching fractions.

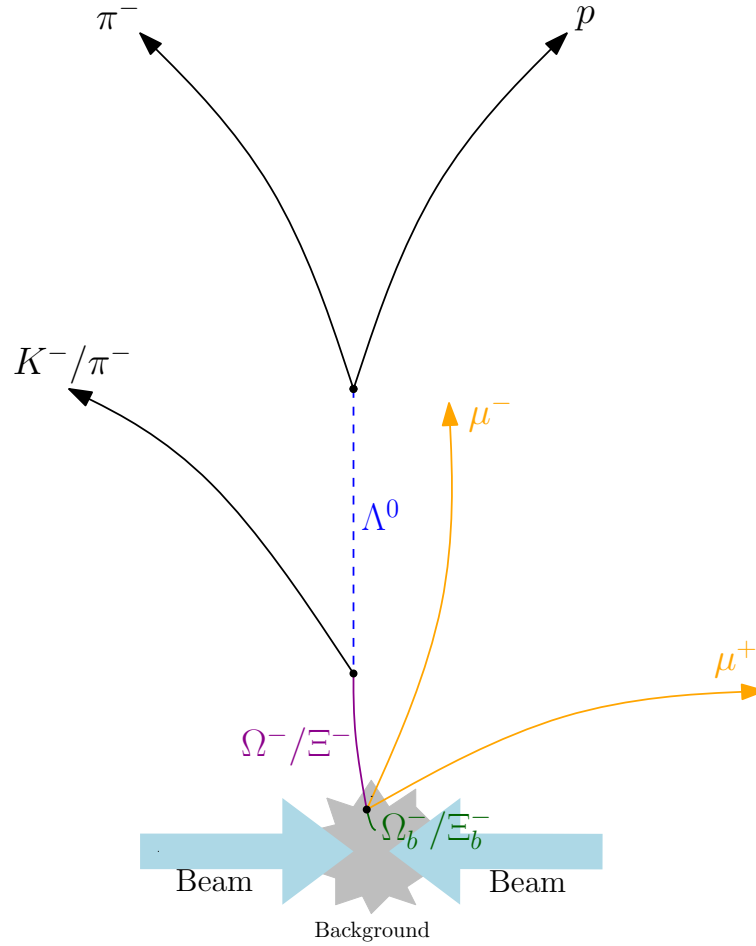


Figure 5.1: Image of the Ξ_b^- and Ω_b^- decay chains.

Table 5.1: Masses and $c\tau$ values of the particles relevant to the analysis [3].

Particle	Mass	$c\tau$ /Lifetime(τ)
J/ψ	3096.916 MeV	-
Ξ^-	1321.71 MeV	4.91 cm
Ω^-	1672.45 MeV	2.461 cm
Λ^0	1115.683 MeV	7.89 cm
μ^\pm	105.658 MeV	658.6 m
K^-	493.677 MeV	3.7 m
p	938.272 MeV	$\tau > 10^{31}$ to 10^{33} yrs.
π^-	139.570 MeV	7.8 m

Table 5.2: Branching ratios of the particles relevant to the analysis [3].

Decay mode	Fraction
$J/\psi \rightarrow \mu^+ \mu^-$	5.93%
$\Xi^- \rightarrow \Lambda^0 \pi^-$	99.9%
$\Omega^- \rightarrow \Lambda^0 K^-$	67.8%
$\Lambda^0 \rightarrow p \pi^-$	63.9%

5.2 Monte-Carlo simulation

The properties of bottom baryons are still ambiguous because they have been discovered very recently. In order to understand the acceptance of the event selections, it is important to use a reasonable model of the bottom baryon production and to have the simulated event samples which are generated according to the model. pp collision interactions are simulated using the PYTHIA event generator. PYTHIA simulates physics processes and the cross sections evaluated by using parton distribution functions of the initial state particles, matrix elements of parton-level hard interactions, and fragmentations of produced partons.

In this analysis, generated events which include (anti-) Ω_b^- or (anti-) Ξ_b^- baryons decaying to the final states described in Section 5.1 are used. The bottom baryons are selected through the fragmentation of b -quarks from $gg \rightarrow b\bar{b}$ and $q\bar{q} \rightarrow b\bar{b}$. They have $p_T > 6$ GeV in $|\eta| < 2.7$.

At least one of the two muons from the J/ψ decay has $p_T > 3.5$ GeV in $|\eta| < 2.5$ for the Level-1 trigger threshold. These fractions to the total generated events are

0.13 for the Ω_b^- simulation and 0.14 for the Ξ_b^- simulation. The efficiency plots are shown in Figure A.1 in Appendix A.1. The number of selected Ω_b^- signal events is 366,998 and that of Ξ_b^- events is 517,119.

In the simulations, the Ω_b^- invariant mass is set to 6071.0 MeV, the world average value in 2012 [3], and that of the Ξ_b^- mass is set to 5791.1 MeV. The Ω_b^- $c\tau$ is set to 0.339 mm and the Ξ_b^- $c\tau$ is set to 0.447 mm.

The generated events are processed through the ATLAS detector simulation [30] based on GEANT4 [31]. Figure 5.2 show the p_T and η distributions of the MC samples before the detector simulation.

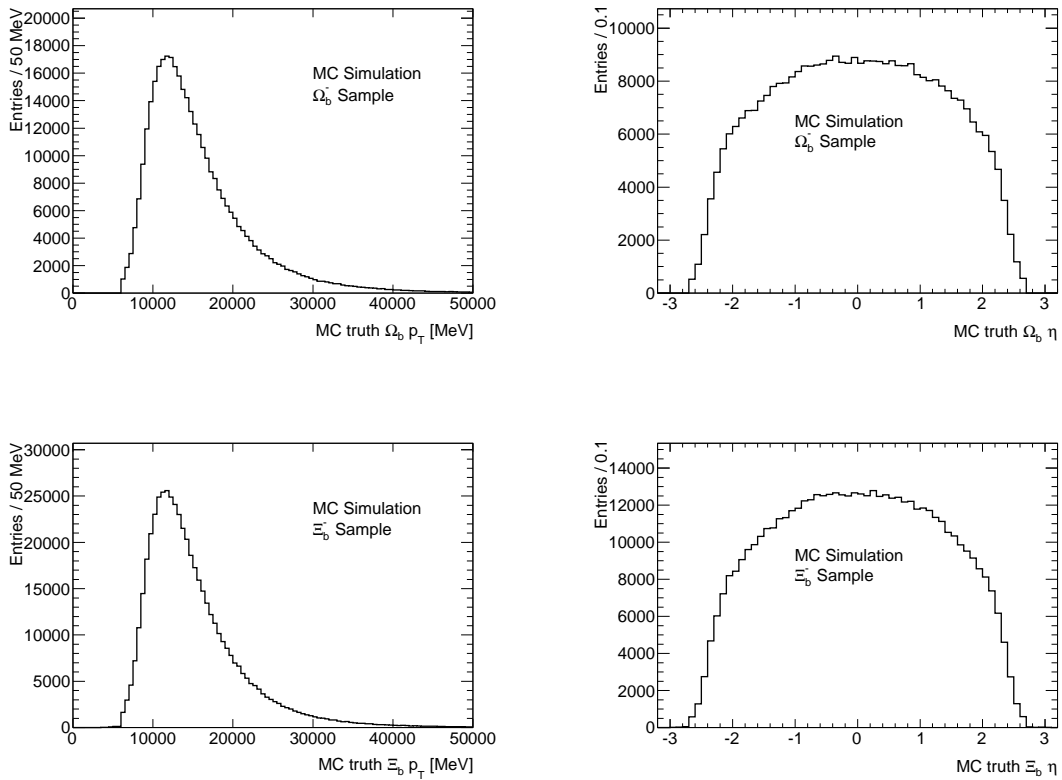


Figure 5.2: p_T (left) and η (right) distributions of the Ω_b^- (top) and Ξ_b^- (bottom) samples before the detector simulation.

5.3 Data samples

The data used in the present analysis were collected in the year 2011 with a center-of-mass energy of 7 TeV of pp collisions. Those data were taken when the LHC beams were stable and all relevant detectors and magnets were running normally. Among the data, the events triggered by the J/ψ trigger are selected. The J/ψ trigger requires a detection of an opposite charge muon pair having an invariant mass within the range of $2.5 < m_{\mu\mu} < 4.3$ GeV [32]. The p_T threshold of the muons is 4 GeV. This trigger mode was prescaled in higher luminosity runs in 2012, whereas it was not prescaled during the 2011 data taking. As a reference, Figure 5.3 shows the muon reconstruction efficiency of the trigger at 7 TeV in 2010 evaluated on candidate $J/\psi \rightarrow \mu^+\mu^-$ events with respect to offline muon reconstruction. The data efficiency evaluated at plateau $p_T > 8$ GeV is 0.41 ± 0.05 while the MC efficiency is 0.39 ± 0.04 , statistical errors only [33].

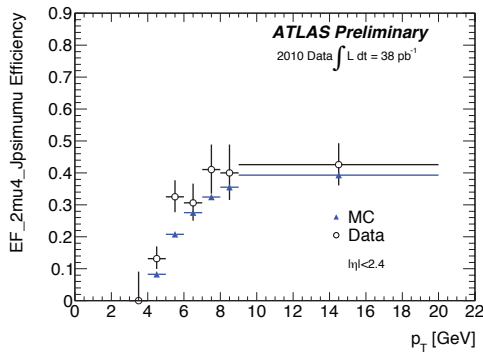


Figure 5.3: Muon reconstruction efficiency of the J/ψ trigger [33].

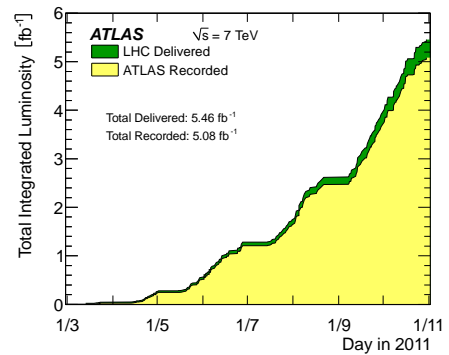


Figure 5.4: Integrated luminosity as a function of the day in 2011 [34].

The used data correspond to an integrated luminosity of 4.5 fb^{-1} . Figure 5.4 shows the increase of the total integrated luminosity as a function of the day in 2011. The integrated luminosity corresponding to the recorded data is 5.08 fb^{-1} , and the data committed by the J/ψ trigger are about 90% of them.

5.4 Muon track reconstruction

5.4.1 Muon reconstruction

Muons which pass the trigger system are reconstructed in the offline software. They are classified into two types of muons: Stand Alone (SA) muons and ComBined (CB)

muons. The SA muons are reconstructed by the Muon Spectrometer (MS) only. The CB muons, which are used in this analysis, are reconstructed by combining MS and ID track parameters. A combined fit is performed using MS and ID track elements that make a nice accompaniment to each other in the (η, ϕ) plane by minimizing the χ^2 equation which is defined as:

$$\chi^2 = (\mathbf{P} - \mathbf{P}_{\text{ID}})^T \times \mathbf{W}_{\text{ID}} \times (\mathbf{P} - \mathbf{P}_{\text{ID}}) + (\mathbf{P} - \mathbf{P}_{\text{MS}})^T \times \mathbf{W}_{\text{MS}} \times (\mathbf{P} - \mathbf{P}_{\text{MS}}), \quad (5.1)$$

where \mathbf{P}_{ID} and \mathbf{P}_{MS} are the two muon track parameters, \mathbf{W}_{ID} and \mathbf{W}_{MS} are their weight matrices, and \mathbf{P} is the combined parameters to be optimized. The optimization is tried for all candidate combinations, and the combination that gives the smallest χ^2 is retained. The optimized \mathbf{P} of the best combination is taken as the parameter of the combined muon track [25], and the combined muons with p_T above 2.5 GeV are retained.

5.4.2 Muon selections

In order to obtain the final muon sample, the reconstructed muon tracks are regarded to be composed of a sufficient number of ID hits. This requirement is effective for reducing backgrounds from the pion and kaon in-flight decays and ensuring a good quality of the muon tracks. The requirements are [35]:

- $n_{\text{Pixel}} \geq 2$:
 n_{Pixel} is the number of hits in the pixel detector plus the number of dead pixel sensors crossed by the track.
- $n_{\text{SCT}} \geq 6$:
 n_{SCT} is the number of hits in SCT plus the number of dead SCT sensors crossed by the track.
- $n_{\text{Pixel}}^{\text{Hole}} + n_{\text{SCT}}^{\text{Hole}} < 3$:
 $n_{\text{Pixel}}^{\text{Hole}} + n_{\text{SCT}}^{\text{Hole}}$ is the number of missing hits in active layers of the pixel detector and SCT.
- $n_{\text{b-layer}} \geq 1$:
 $n_{\text{b-layer}}$ is the number of hits in the innermost layer (b-layer) of the pixel detector. If the track is expected to pass outside the b-layer, this requirement is not applied.
- Number of TRT hits:
 If the track is contained within the coverage of TRT ($|\eta| < 1.9$), $n > 5$ and $n_{\text{TRT}}^{\text{outliers}} < 0.9n$ are required. Here, n is the number of TRT hits used for the

track reconstruction ($n_{\text{TRT}}^{\text{hits}}$) plus that of TRT hits associated with the track but not used ($n_{\text{TRT}}^{\text{outliers}}$), i.e., $n = n_{\text{TRT}}^{\text{hits}} + n_{\text{TRT}}^{\text{outliers}}$.

If $|\eta| \geq 1.9$ and $n \leq 5$, this requirement is not applied. If $|\eta| \geq 1.9$ and $n > 5$, $n_{\text{TRT}}^{\text{outliers}} < 0.9n$ is required.

If two opposite sign muons in an event satisfy the above requirements, the pair is used for the J/ψ reconstruction.

5.5 J/ψ reconstruction

Before starting the J/ψ vertex fit, the invariant mass of the selected muon pairs is required to be within the range of $|M_0(\mu^+\mu^-) - M_{\text{PDG}}(J/\psi)| < 200$ MeV. This requirement reduces a lot of irrelevant combinations of muons. Here, the index 0 of M_0 denotes the value calculated at the perigee. This requirement is loose enough to retain almost all J/ψ signals. The invariant mass distribution is shown in Figure 5.5 and the PDG average value is indicated as the red line. A partial sample corresponding to the integrated luminosity of 11.6pb^{-1} is used for the plot. A clear peak corresponding to the J/ψ signal can be seen, but the sample is still contaminated with background.

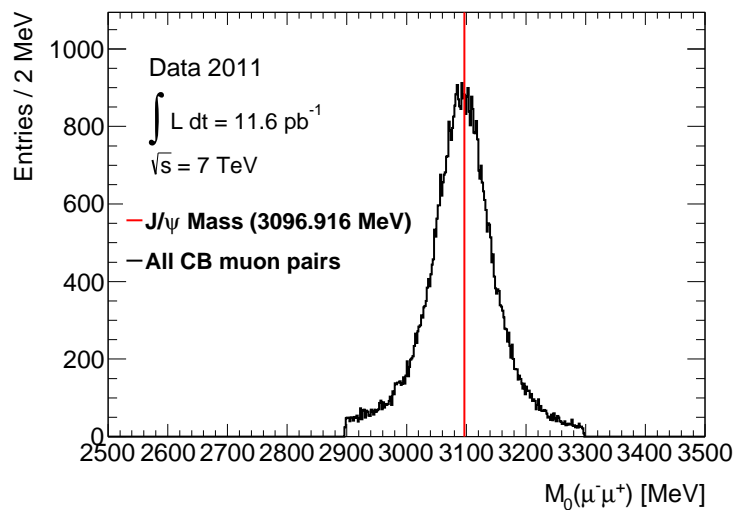


Figure 5.5: Invariant mass distributions of the combined muon pairs.

Track parameters such as p_T , η , and ϕ of the preselected muons are fitted with a constraint of the known J/ψ mass as described in Section 4.2. The fit is carried out by assuming that the muon pair originates from a common vertex. Then, the following requirements are imposed to select a pure J/ψ sample. The requirements are

- $\chi_m^2 < 4$,
- $|\eta_m| < 2.5$,

where the index m denotes a value after the ‘m’ass constraint. Figure 5.6 shows the invariant mass distributions evaluated by using the original track parameters of the muon pairs. The distributions are separately shown for the muon pair samples with $\chi_m^2 > 4$ or $|\eta_m| > 2.5$, and $\chi_m^2 < 4$ and $|\eta_m| < 2.5$. The $\chi_m^2 > 4$ or $|\eta_m| > 2.5$ pairs are rejected as the background. The obtained signal ($\chi_m^2 < 4$ and $|\eta_m| < 2.5$) distribution is compared with simulation results in Figure 5.7. The left side plot shows the comparison with the Ω_b^- simulation and the right side one shows that with the Ξ_b^- simulation. The simulations are normalized to the number of entries. The distributions are basically in good agreement with a small shift of the peak position. The peak position is 3095.1 ± 0.2 MeV for the data, and 3101.1 ± 0.1 MeV and 3100.8 ± 0.1 MeV for the Ω_b^- and Ξ_b^- simulations, respectively. These mass differences are used for estimating the systematic uncertainties in Subsection 6.1.4.

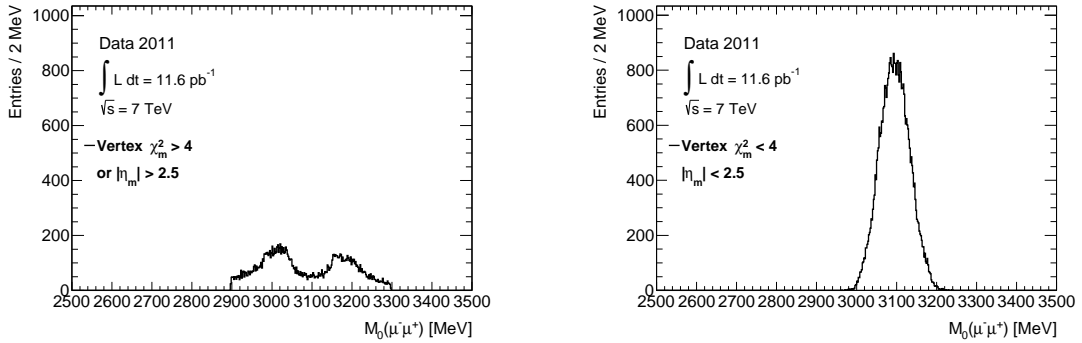


Figure 5.6: Invariant mass distributions of the combined muon pairs satisfying the quality requirements.

Figure 5.8 shows the p_{Tm} , η_m , and ϕ_m distributions of the muons composing the selected J/ψ candidates. There is no significant bias depending on the sign of the charge. The effective threshold of the selected muons is approximately 4 GeV due to the trigger. The dips at $|\eta_m| \sim 0$ and 1 are due to the boundaries in the muon detector system and those at $-2.5 \lesssim \phi_m \lesssim -1.5$ are due to the supporting columns of the ATLAS detector. In both angular distributions, the shapes of μ^+ and μ^- are slightly different. This difference reflects the effect of the magnetic field. Figure 5.9 shows the χ_m^2 , p_{Tm} , η_m , and ϕ_m distributions of the J/ψ candidates. The shaded areas represent the distributions after all requirements. The structures in the η_m and ϕ_m distributions reflect the distributions of composing muons.

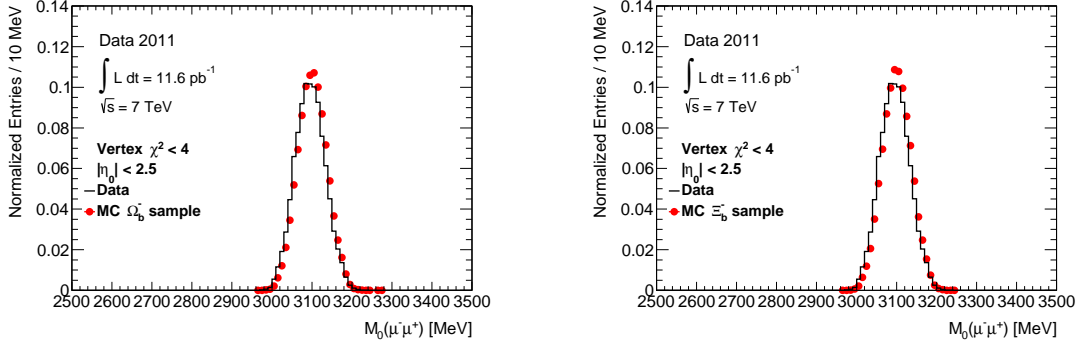


Figure 5.7: Invariant mass distributions of the combined muon pairs in the data and the MC samples.

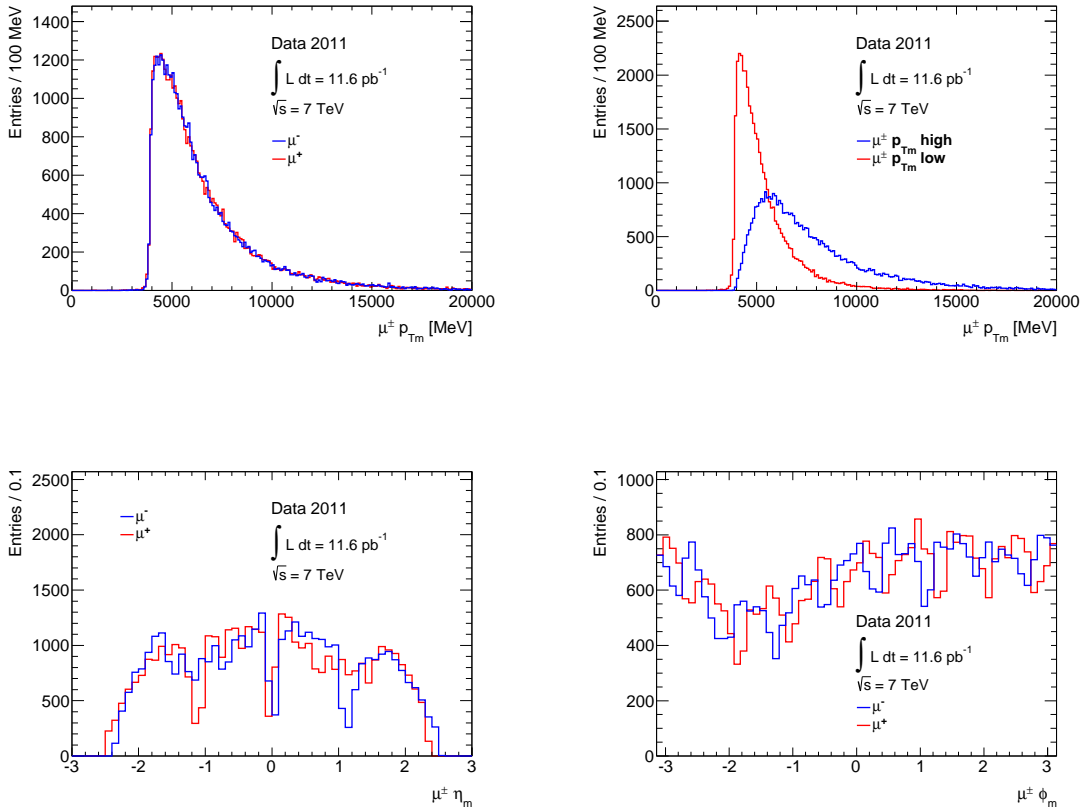


Figure 5.8: p_{Tm} , η_m , and ϕ_m distributions of the muons composing the J/ψ candidates.

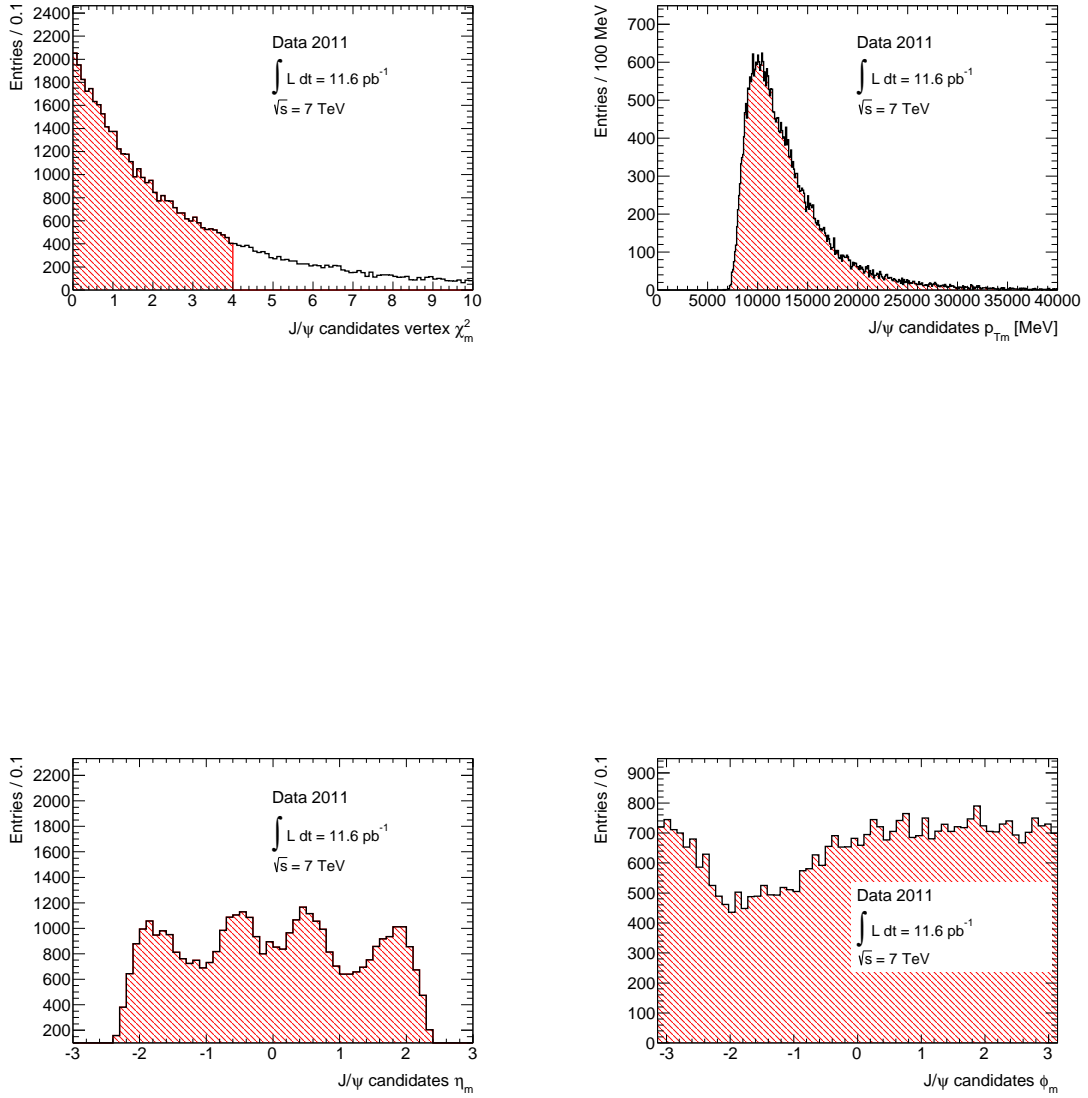


Figure 5.9: χ_m^2 , p_{Tm} , η_m , and ϕ_m distributions of the J/ψ candidates. Those pairs having $\chi_m^2 > 4$ are included in the χ_m^2 distribution.

Figure 5.10 shows the distributions of the angular distance (dR) between the truth and the reconstructed J/ψ candidates in the MC simulations. Here, the truth values correspond to the production point in the event generation and dR is defined as $dR \equiv \sqrt{(\eta_{\text{truth}} - \eta_{\text{reco.}})^2 + (\phi_{\text{truth}} - \phi_{\text{reco.}})^2}$. In the distributions, almost all of the reconstructed J/ψ candidates have $dR < 0.01$ and this value corresponds to the difference of 0.57° ($dR \sim d\phi = 0.01[\text{rad}]$). When $dR < 0.05$ is required as a condition of matching between the truth J/ψ and the reconstructed J/ψ candidates, the efficiencies and the distributions in p_T , η , and ϕ are shown in Figure 5.11. The left side plots are the Ω_b^- simulation and the right side ones from the Ξ_b^- simulation. The efficiencies which depend on η and ϕ are roughly flat except for regions of the detector boundaries and columns, and the efficiency in p_T depends on the p_T value; the efficiency increases from 0 to ~ 0.3 in the p_T range of $8 < p_T < 14$ GeV, and the efficiency of approximately 0.3 is kept in $14 < p_T < 30$ GeV.

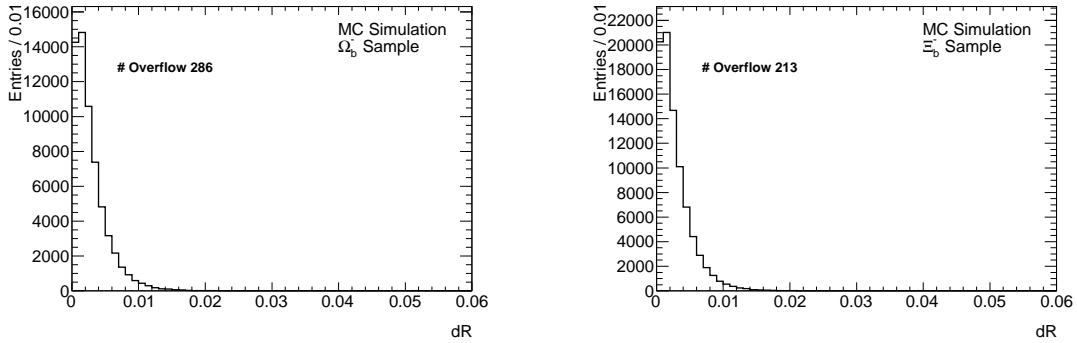


Figure 5.10: dR distributions between the truth J/ψ and the reconstructed J/ψ candidates.

In the MC simulations, 61,377 and 85,827 J/ψ candidates are matched in the Ω_b^- and Ξ_b^- MC samples, respectively. Also, the corresponding J/ψ reconstruction efficiencies are 16.7% and 16.6%. In total, 1.5×10^7 events are selected at this stage from the data corresponding to the full luminosity.

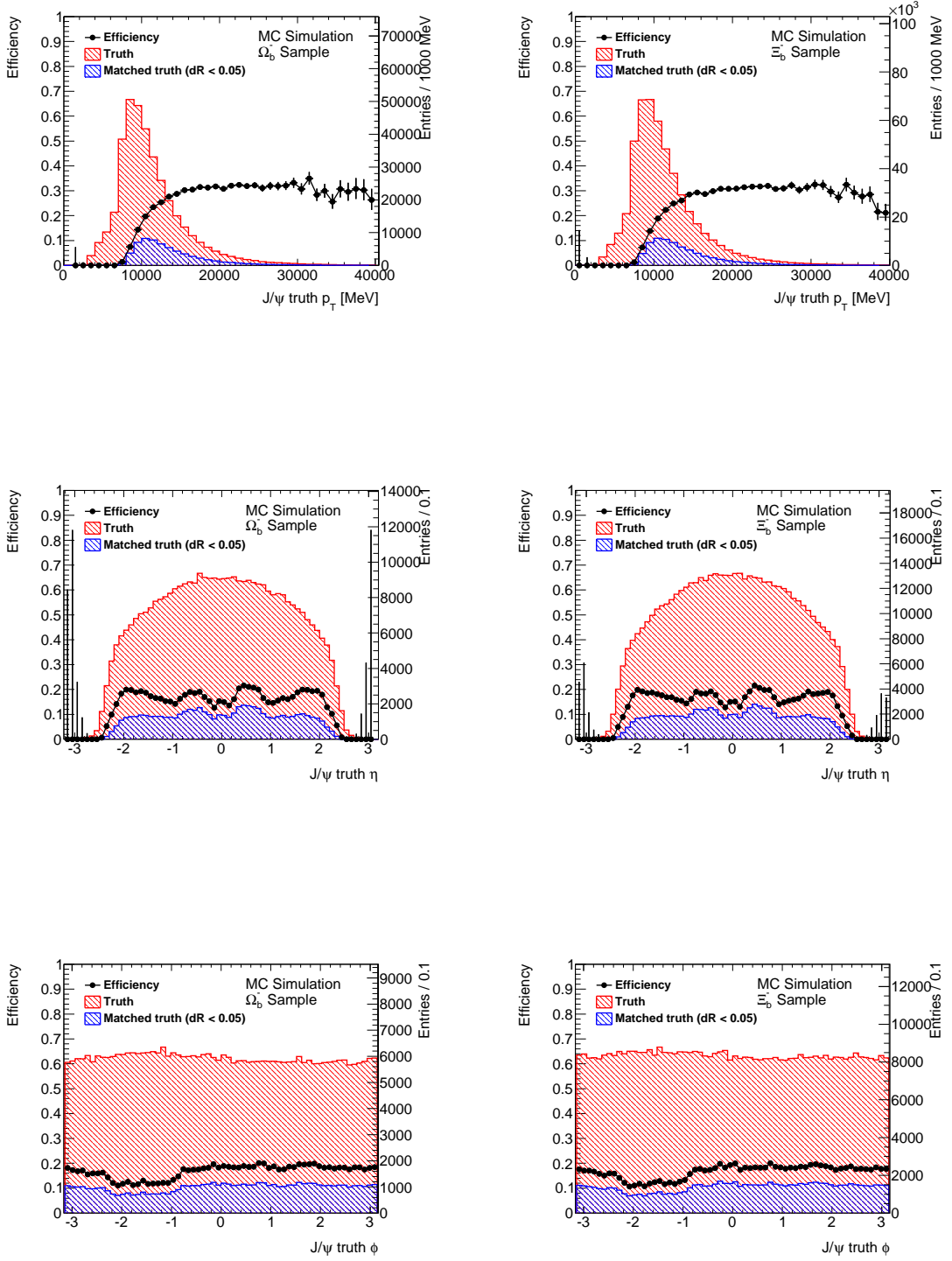


Figure 5.11: J/ψ reconstruction efficiencies.

5.6 Baryon reconstruction

The vertex fit for reconstructing Λ^0 , Ξ^- , and Ω^- candidates is applied to the events including the selected J/ψ candidates described in the previous section. Three tracks reconstructed in the inner detector are used for the fit. The used track are required to satisfy the conditions, $p_{T0} > 400$ MeV and $|\eta_0| < 2.5$.

In order to save the CPU time, opposite charged track pairs having the invariant mass within the range of $|M_0(p\pi^-) - M_{\text{PDG}}(\Lambda^0)| \leq 25$ MeV are preselected to apply the Λ^0 -vertex fit because there are a lot of irrelevant track combinations. The proton (pion) mass is assumed for the positive (negative) charged track in this preselection. The vertex fit is applied to this track pair and another track simultaneously by taking into account the Λ^0 , Ξ^- , and Ω^- decay kinematics described in Section 5.1.

In this analysis, antiparticles of the Λ^0 , Ξ^- , and Ω^- baryons are also considered. However, in the following section (and chapter), the description is made only for the particles for the sake of simplicity since the antiparticle discussions are the same. Plots which are shown in the next subsections are the results after merging the particles and the antiparticles, unless explicitly commented.

5.6.1 Λ^0 reconstruction

The proton mass is assigned to the positive charged track and the pion mass to the negative charged track to reconstruct the Λ^0 candidate. A good quality is required to the proton and pion tracks to be used for the reconstruction. The requirements are

- $n_{\text{SCT}} \geq 6$ for the proton and pion tracks,
- $p_{Tn} > 500$ MeV for the proton tracks and $p_{Tn} > 250$ MeV for the pion tracks,
- $|\eta_n| < 2.5$ for the proton and pion tracks,

where the index n denotes a value measured at the fitted $p\pi$ vertex with ‘n’o constraint on the Λ^0 mass. After applying the vertex fit, the Λ^0 candidates are selected by requiring

- $\chi_n^2 < 4$,
- $|\eta_n| < 2.5$.

Figure 5.12 shows the invariant mass distribution of the Λ^0 candidates satisfying the above requirements. A clear Λ^0 peak is observed on a smooth background. The background can be well described by a quadratic function illustrated with a magenta

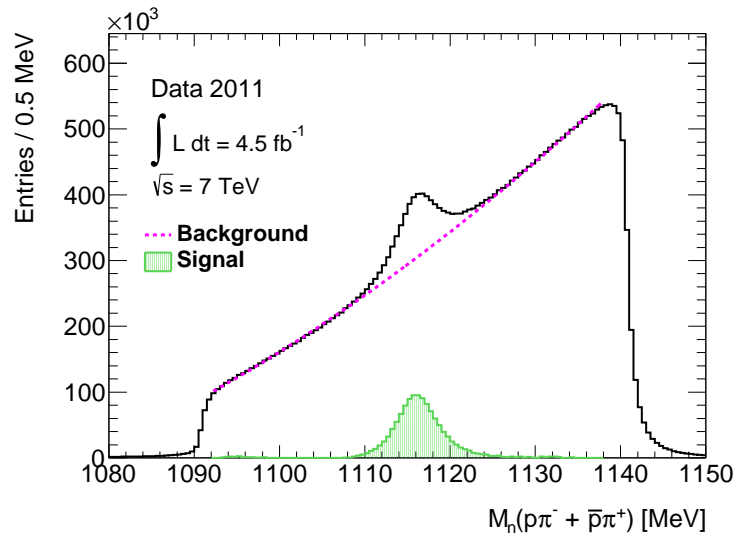


Figure 5.12: Invariant mass distributions of the Λ^0 candidates satisfying the quality requirements.

line. The fitted ranges are $1092 < M_n < 1107$ MeV and $1125 < M_n < 1138$ MeV. The green area shows the distribution after the subtraction of the background.

The $c\tau$ of the Λ^0 baryon is about 7.89 cm. Therefore, requirements utilizing the long lifetime is expected to be very effective for reducing the background. L_{xy} , the 2-dimensional flight distance, is used for this. The definition of L_{xy} is illustrated in Figure 5.13. Figure 5.14 shows the L_{xy} distribution of the Λ^0 candidates. The red line is the distribution within the range of $|M_n(p\pi^-) - M_{\text{PDG}}(\Lambda^0)| \leq 9$ MeV (signal region), while the blue one is within the range of $12 \leq |M_n(p\pi^-) - M_{\text{PDG}}(\Lambda^0)| \leq 21$ MeV (sideband region), where the distributions are normalized to the background contributions estimated by the fit in Figure 5.12. The difference between these two distributions approximately show the distribution of the signal. Therefore, from the figure, the L_{xy} threshold of 10 to 20mm will reject a dominant part of the background with rejection of only a small portion of the signal. The L_{xy} requirement which is actually applied for the Λ^0 reconstruction is

- $L_{xy} > 15$ mm.

In the L_{xy} distribution in Figure 5.14, three peaks around $L_{xy} \sim 50, 90,$ and 120 mm are seen. These peaks correspond to the positions of the pixel detectors (see Figure 3.5). The vertices forming these peaks originate from secondary interactions of particles in the pixel detectors. A 2-dimensional distribution of the vertex position of the candidate track pairs in the sideband region is shown in Figure 5.15. In the plot, x and y represent the relative position with respect to the J/ψ vertex. Since

the J/ψ vertex is always very close to the x - y origin of the ATLAS coordinate, the x and y values almost coincide with actual coordinates of the Λ^0 candidate vertex. The distribution around $r = 50$ mm clearly shows the fine structure of the pixel detectors.

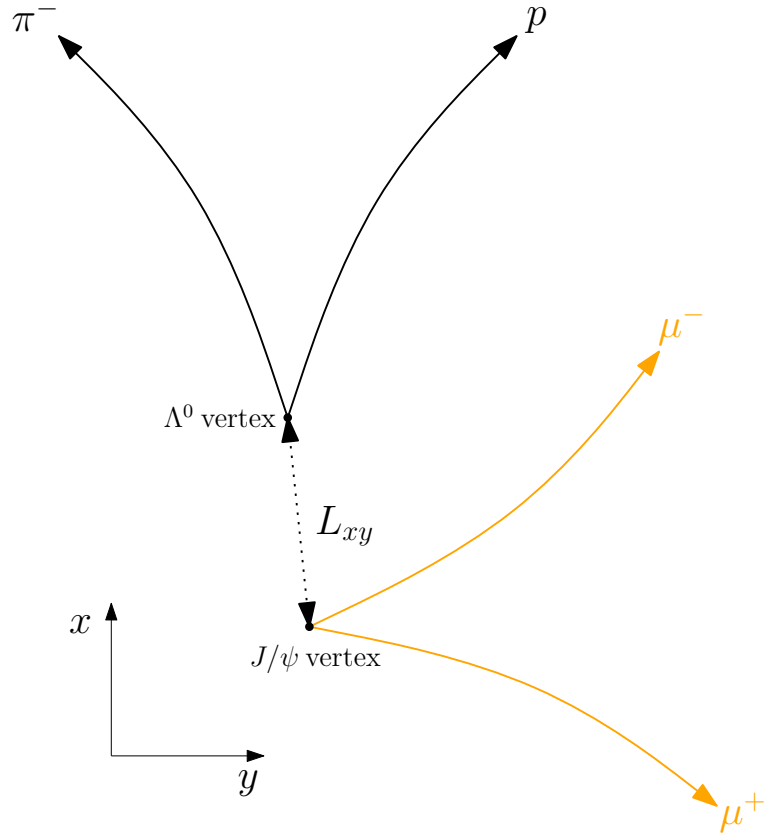
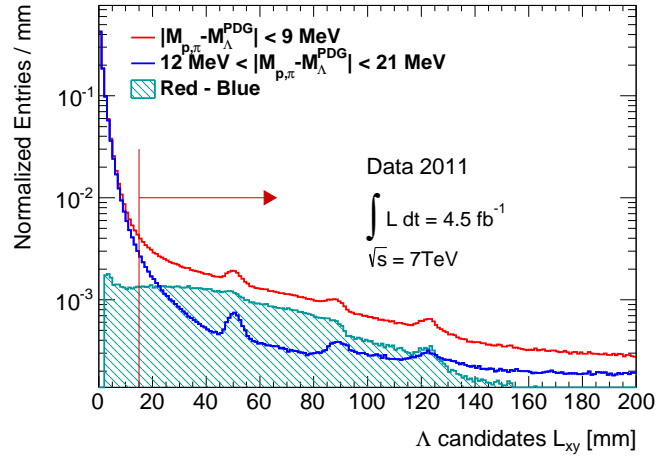
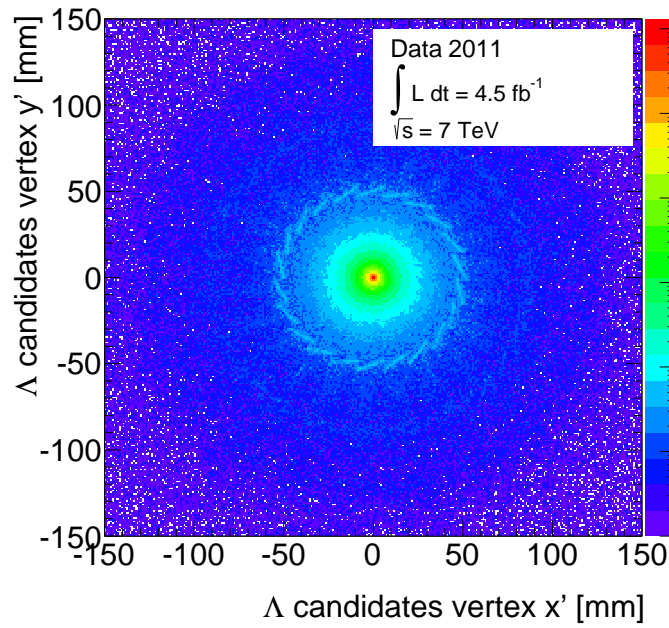


Figure 5.13: Illustration of L_{xy} for the Λ^0 analysis.

Figure 5.14: L_{xy} distribution of the Λ^0 candidates.Figure 5.15: 2-dimensional vertex position distribution of the Λ^0 candidates in the sideband region.

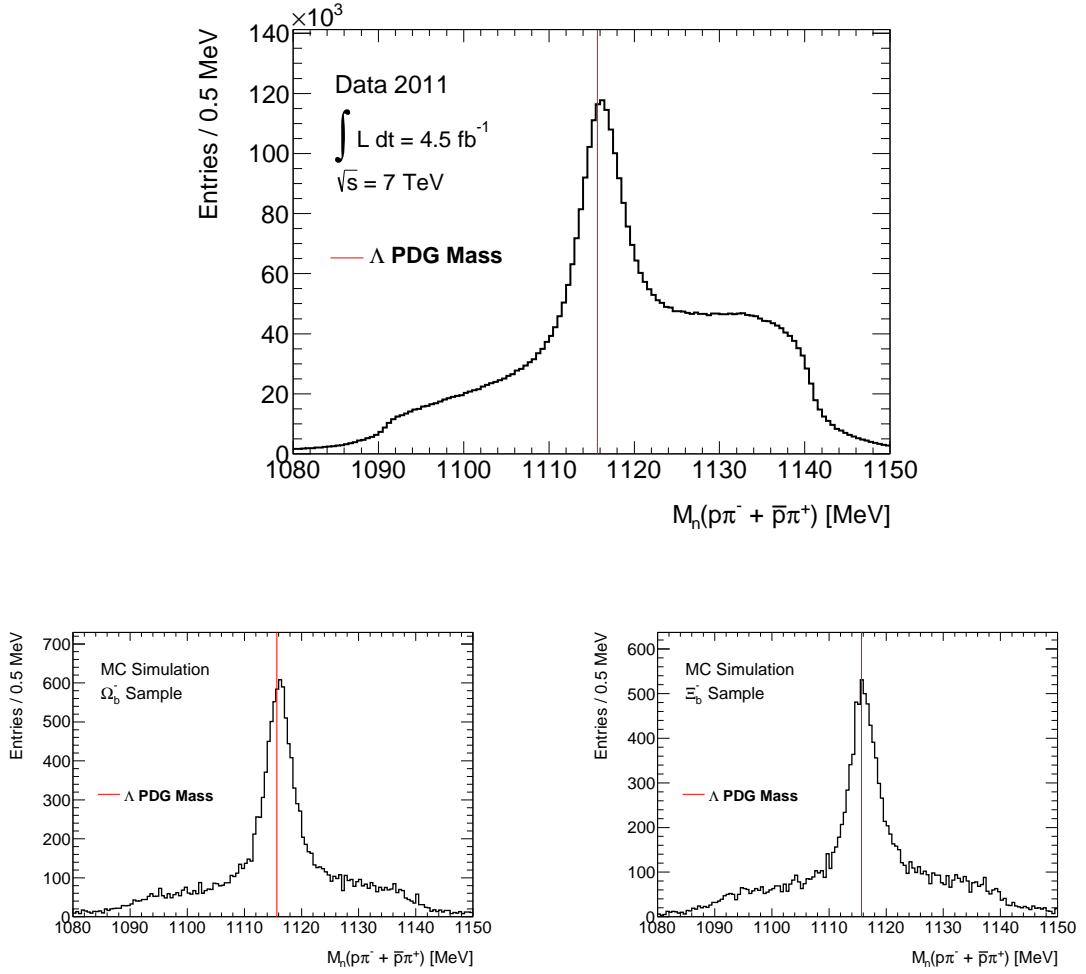


Figure 5.16: Invariant mass distributions of the Λ^0 candidates satisfying all requirements in the data and the MC samples.

The top of Figure 5.16 shows the invariant mass distribution of the Λ^0 candidates satisfying the L_{xy} requirement for the data sample shown in Figure 5.12, and the bottom panel shows the corresponding results from the MC simulations. The red line shows the Λ^0 mass of PDG. The L_{xy} requirement has significantly reduce the background compared to Figure 5.12. Figure 5.17 shows the χ_n^2 , p_{Tn} , η_n , and ϕ_n distributions of the Λ^0 candidates in the signal region. The η_n and ϕ_n distributions are almost flat in the range of detection. All Λ^0 candidates have a threshold of approximately 1.4 GeV.

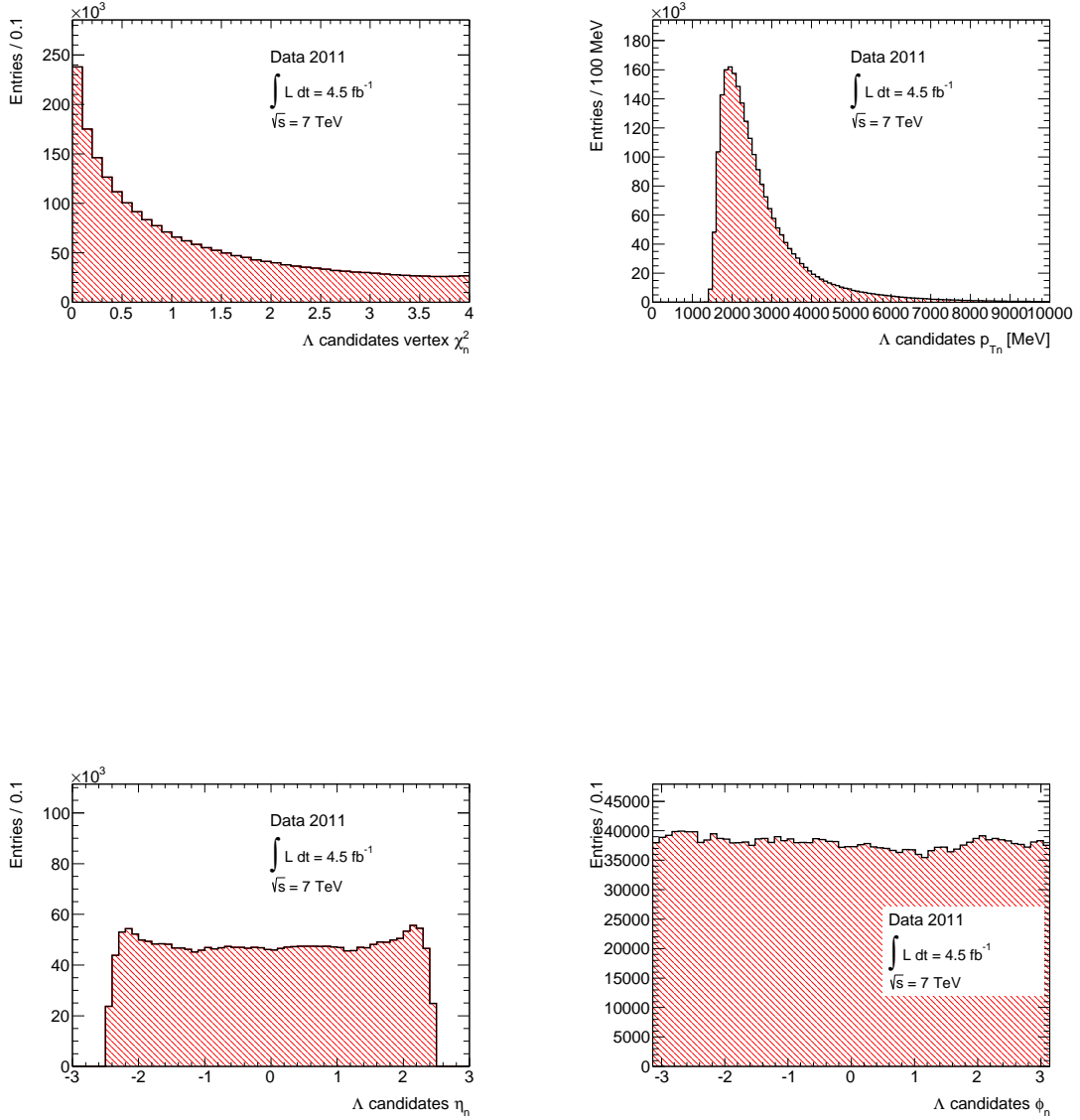


Figure 5.17: χ_n^2 , p_{Tn} , η_n , and ϕ_n distributions of the Λ^0 candidates after the L_{xy} requirement in the signal region.

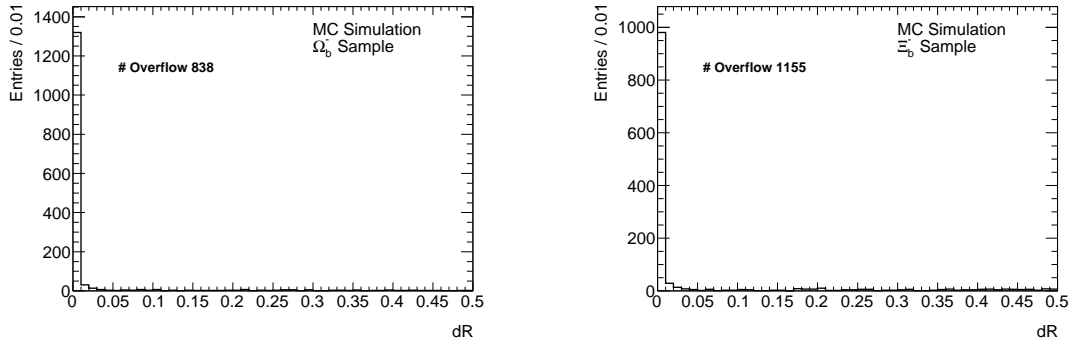
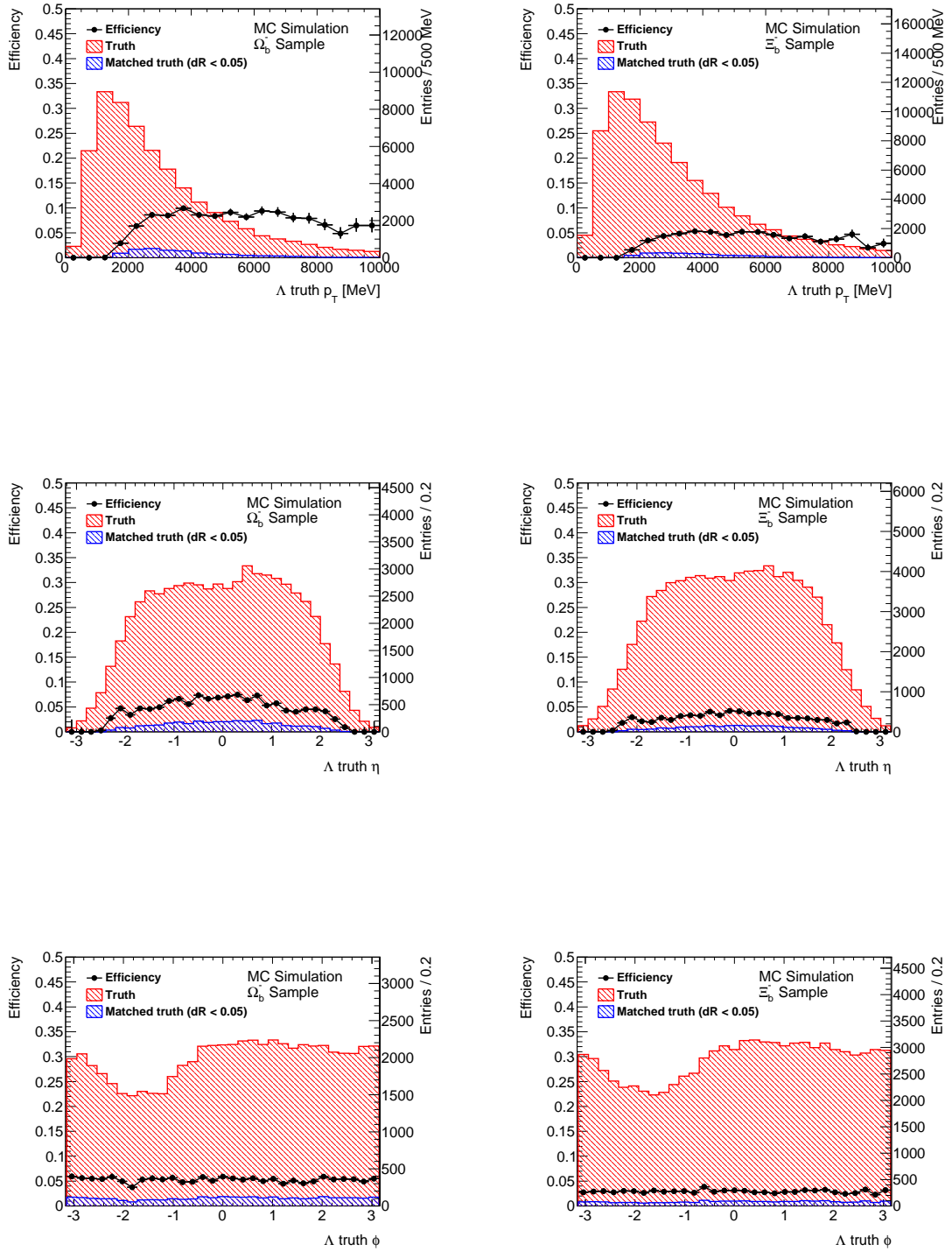


Figure 5.18: dR distributions between the truth Λ^0 and the reconstructed Λ^0 candidates.

Figure 5.18 shows the distributions of dR between the truth Λ^0 and reconstructed Λ^0 vertices in the simulations. The matching condition of $dR < 0.05$ is again required to evaluate the Λ^0 selection conditions. The efficiency of the Λ^0 selection is evaluated by applying the same selection requirements to the simulation samples. Figure 5.19 shows the generated and selected truth Λ^0 distributions in the events containing the J/ψ candidates. The efficiency evaluated as the ratio between the two distributions is also plotted. Figure 5.20 show the L_{xy} distributions at the truth level for the Ω_b^- and Ξ_b^- MC samples. The efficiencies drop to zero for $L_{xy} > 300$ mm because of the n_{SCT} requirement.

In total, 2.4×10^6 events are selected at this stage from the data. In the MC simulations, 3,252 Ω_b^- events and 2,508 Ξ_b^- events are selected. The corresponding Λ^0 reconstruction efficiencies are estimated to be 5.2% and 2.9%, respectively.

Figure 5.19: Λ^0 reconstruction efficiencies.

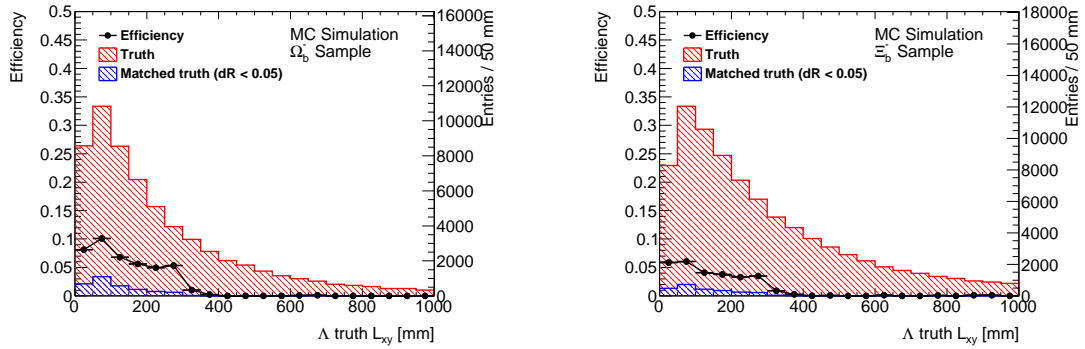


Figure 5.20: Λ^0 reconstruction efficiencies in L_{xy} at the truth level.

5.6.2 Ξ^- reconstruction

The Ξ^- baryon in the Ξ_b^- decay chain is reconstructed using the selected Λ^0 candidates in the signal region $|M_n(p\pi^-) - M_{\text{PDG}}(\Lambda^0)| \leq 9 \text{ MeV}$. The vertex fit is applied to the combination of the Λ^0 candidates and another negative charged particle satisfying the conditions;

- $n_{\text{Pixel}} \geq 1$,
- $n_{\text{SCT}} \geq 6$,
- $p_{Tn} > 250 \text{ MeV}$,
- $|\eta_n| < 2.5$.

The pion mass is assumed for the additional particle in the fit. Using the fit results, those combinations satisfying the conditions

- Ξ^- candidates vertex $\chi_n^2 < 4$,
- Ξ^- candidates $|\eta_n| < 2.5$,

are selected as Ξ^- candidates. Figure 5.21 shows the invariant mass distribution of the Ξ^- candidates. The Ξ^- signal is clearly observed on a smooth background. The green area shows the signal contribution after subtracting the background fitted to the function $f(x) = a + bx + c \log(x + d)$.

The $c\tau$ of the Ξ^- baryon is about 4.91 cm, therefore L_{xy} cut is again effective for reducing the background as in the case of the Λ^0 analysis. In addition, a requirement on the angle between the Ξ^- momentum direction and the vertex direction with respect

to the J/ψ vertex, i.e., the pointing angle $\cos\theta$ cut, is also effective. The definition of the pointing angle is illustrated in Figure 5.22. Figure 5.23 shows the L_{xy} distribution of the Ξ^- candidates and Figure 5.24 shows the $\cos\theta$ distribution. The red line is the distribution within the range of $|M_n(\Lambda^0\pi^-) - M_{\text{PDG}}(\Xi^-)| \leq 11$ MeV (signal region), and the blue one is within the range of $16 \leq |M_n(\Lambda^0\pi^-) - M_{\text{PDG}}(\Xi^-)| \leq 27$ MeV (sideband region). The plots are also normalized to the background contributions estimated by the fit. The following requirements are imposed to the Ξ^- candidates to reduce the background:

- Ξ^- candidates $L_{xy} > 10$ mm.
- Ξ^- candidates $\cos\theta > 0.9$.

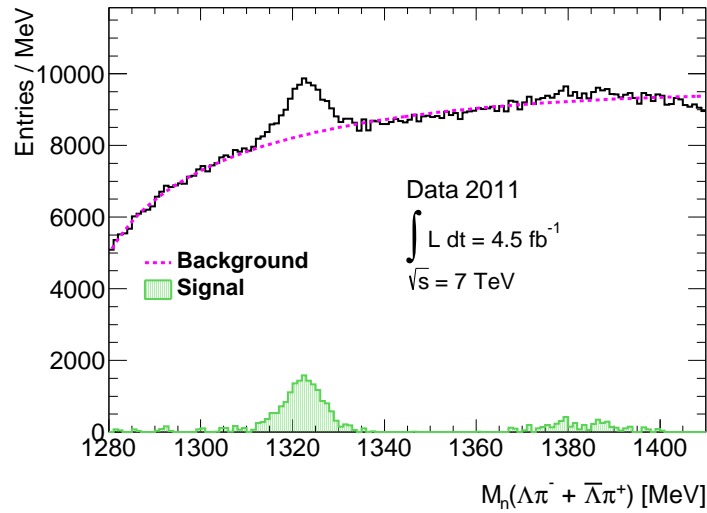


Figure 5.21: Invariant mass distributions of the Ξ^- candidates satisfying the quality requirements.

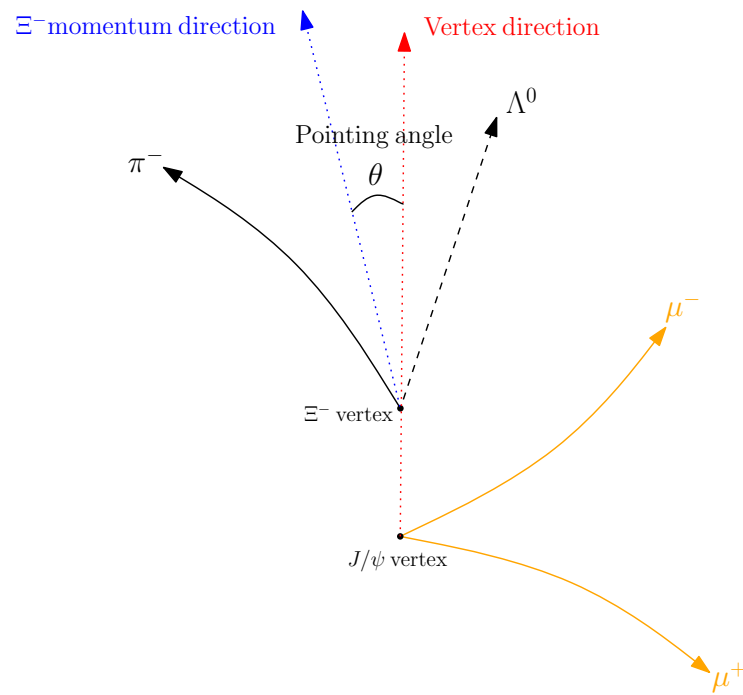


Figure 5.22: Illustration of the pointing angle for the Ξ^- analysis.

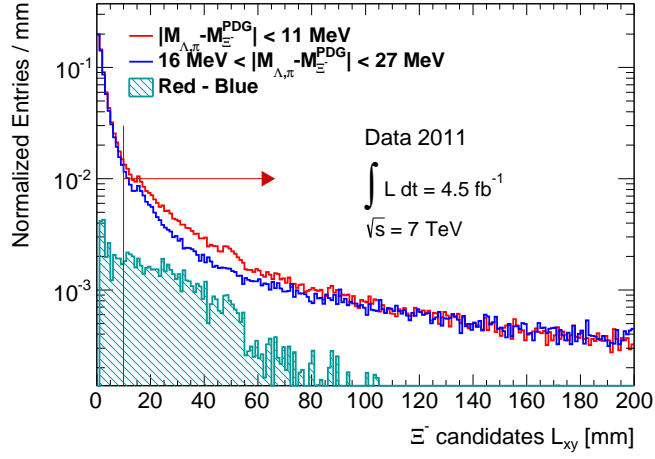
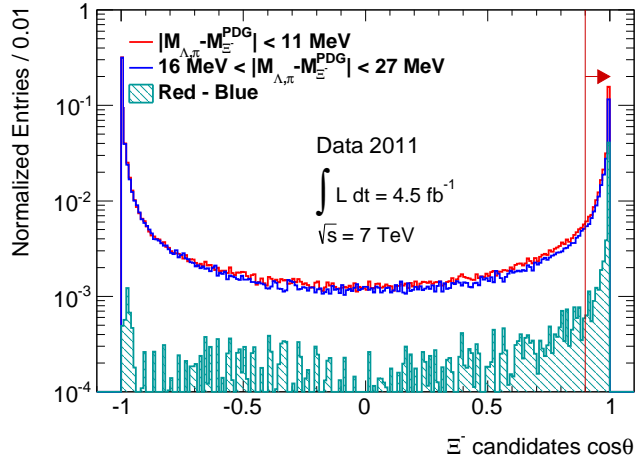
Figure 5.23: L_{xy} distribution of the Ξ^- candidates.Figure 5.24: $\cos\theta$ distribution of the Ξ^- candidates in the signal region.

Figure 5.25 shows the invariant mass distributions of the Ξ^- candidates satisfying all requirements. Figure 5.26 shows the χ_n^2 , p_{Tn} , η_n , and ϕ_n distributions of the selected Ξ^- candidates. The η_n distribution has an enhancement at the large $|\eta_n|$ (detailed in Section 5.7). The ϕ_n distribution is almost flat in the range of detection. The Ξ^- candidates are $p_{Tn} \gtrsim 1.8$ GeV.

In total, 1.9×10^4 events that include the Ξ^- candidates in the signal region are selected at this stage from the data. From the MC sample, 1,225 events are retained. The corresponding Ξ^- reconstruction efficiency is 45%. Further details are described in Appendix A.3. Table 5.3 shows the summary of the selected events at each stage.

Table 5.3: Summary table of the selected Ξ_b events in the signal regions at each stage.

	data	MC
Generated	-	517,119
J/ψ	1.5×10^7	85,827
$\Lambda^0 + \bar{\Lambda}^0$	2.4×10^6	2,508
$\Xi^- + \bar{\Xi}^-$	1.9×10^4	1,225

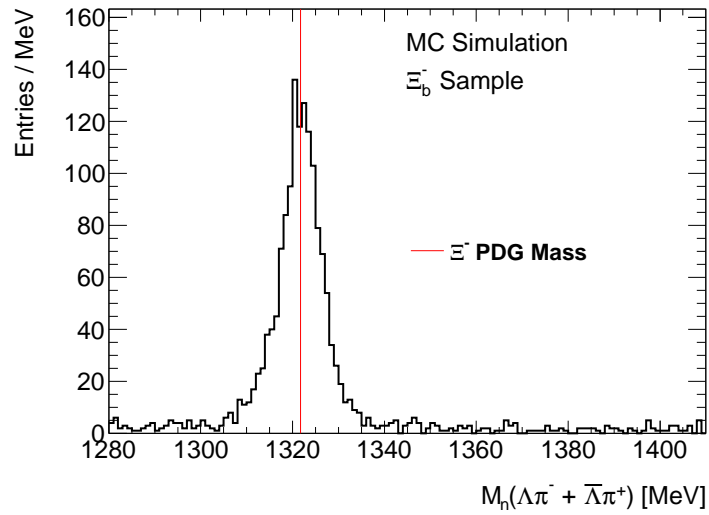
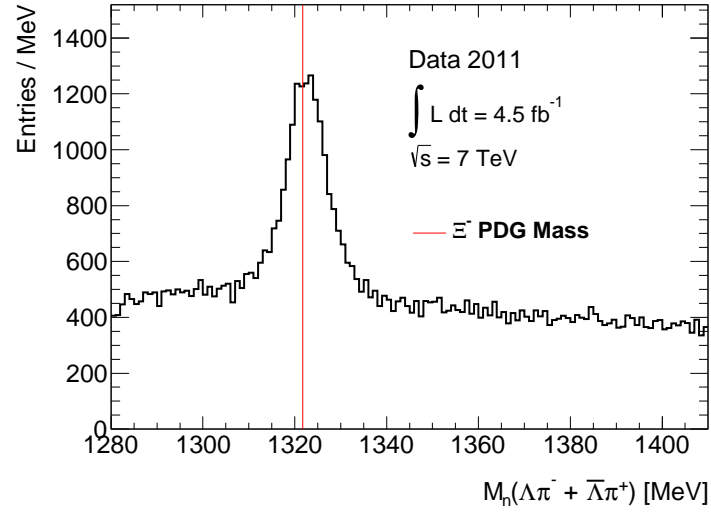


Figure 5.25: Invariant mass distributions of the Ξ^- candidates satisfying all requirements in the data and the MC sample.

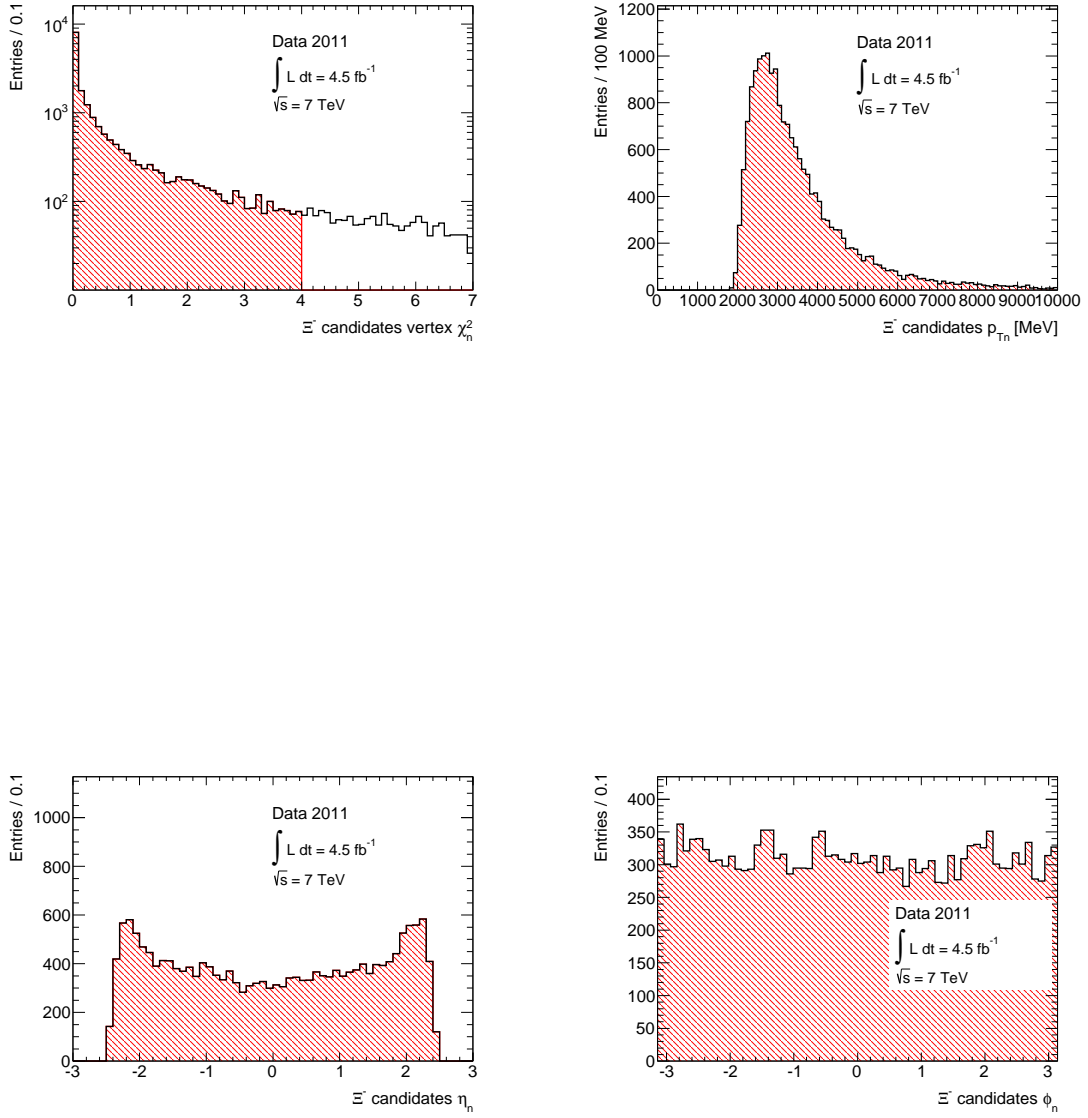


Figure 5.26: χ_n^2 , p_{Tn} , η_n , and ϕ_n distributions of the Ξ^- candidates in the signal region.

5.6.3 Ω^- reconstruction

The method of the Ω^- reconstruction is basically the same as that of the Ξ^- reconstruction. The kaon mass is assumed for the additional negative charged track and the track is combined with the Λ^0 candidate in the signal region $|M_n(p\pi^-) - M_{\text{PDG}}(\Lambda^0)| \leq 9\text{MeV}$. Quality requirements to the kaon tracks and the Ω^- candidates are also same, except for the p_{T_n} requirement. The kaon p_T is required to be $p_{T_n} > 400\text{ MeV}$.

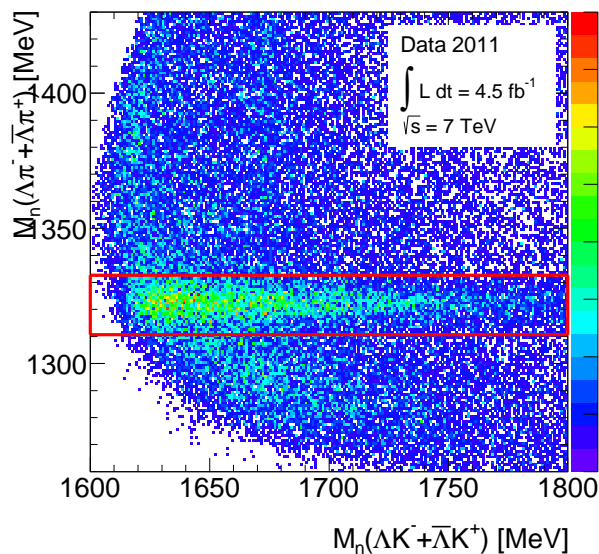


Figure 5.27: 2-dimensional invariant mass distribution for the Ξ^- kinematics reflection.

The decay kinematics of the Ω^- baryon which is tagged in the present analysis is identical to that of the Ξ^- baryon. As the production cross section of the Ω^- baryon is generally smaller than the Ξ^- baryon, the Ξ^- candidates are a potential background of the Ω^- reconstruction. To reduce this reflection, the following kinematical cut is applied to the Ω^- candidates:

- The Ω^- candidates are excluded if $|M_n(\Lambda^0 K^-) - M_{\text{PDG}}(\Xi^-)| \leq 11\text{ MeV}$ is satisfied when the pion mass is assigned to the ‘kaon’ track.

Figure 5.27 shows the 2-dimensional distribution of the evaluated invariant mass; the x value is the mass with the K^- assumption and the y value with the π^- assumption. The combinations in the red rectangular are excluded for the Ω^- candidates. Figure 5.28 shows the invariant mass distribution of the remaining Ω^- candidates. Although it is small, the Ω^- signal is visible on the smooth background.

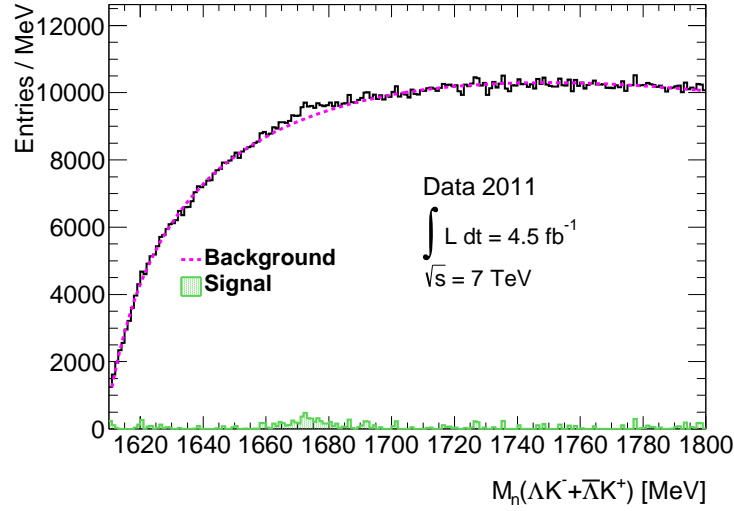


Figure 5.28: Invariant mass distributions of the Ω^- candidates satisfying the quality requirements and removing the Ξ^- kinematics reflection.

The $c\tau$ of the Ω^- baryon is about 2.461 cm. The L_{xy} and pointing angle $\cos\theta$ cuts are effective to reduce the background as in the case of the Ξ^- analysis. Figure 5.29 shows the L_{xy} distribution of the Ω^- candidates and Figure 5.30 shows the $\cos\theta$ distribution. The red line is the distribution of the candidates within the range of $|M_n(\Lambda^0 K^-) - M_{\text{PDG}}(\Omega^-)| \leq 11$ MeV (signal region), and the blue one is within the range of $16 \leq |M_n(\Lambda^0 K^-) - M_{\text{PDG}}(\Omega^-)| \leq 27$ MeV (sideband region). The plots are also normalized to the background contributions estimated by the fit. The following requirements are additionally imposed to the Ω^- candidates:

- Ω^- candidates $L_{xy} > 10$ mm.
- Ω^- candidates $\cos\theta > 0.9$.

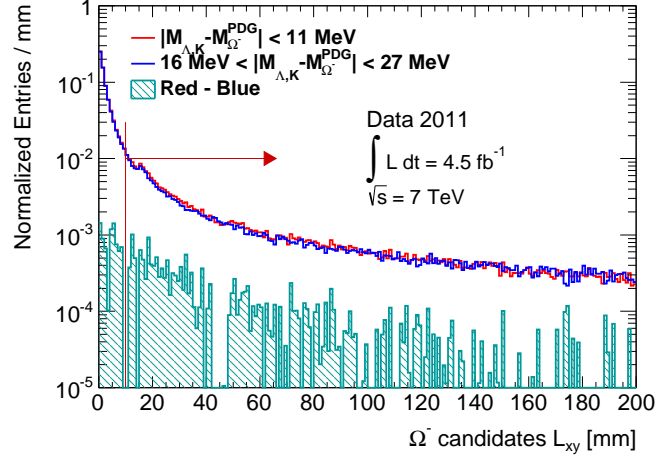
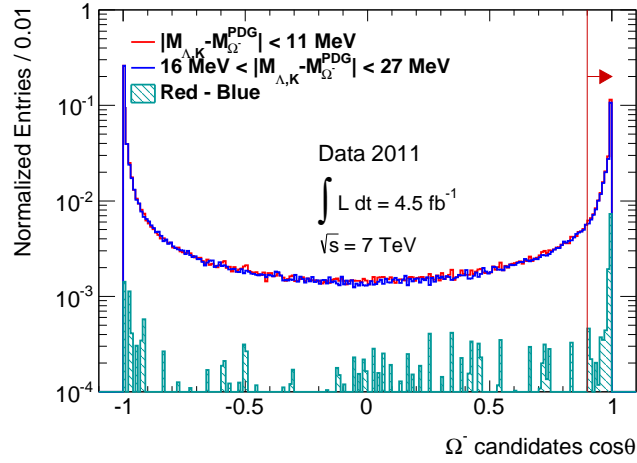
Figure 5.29: L_{xy} distribution of the Ω^- candidates.Figure 5.30: $\cos \theta$ distribution of the Ω^- candidates.

Figure 5.31 shows the invariant mass distribution of the Ω^- candidates satisfying these requirements, together with the corresponding distribution from the simulation. The signal distribution has been significantly clarified by the L_{xy} and $\cos\theta$ requirements. Figure 5.32 shows the χ_n^2 , p_{Tn} , η_n , and ϕ_n distributions of the Ω^- candidates in the signal region. The distributions look very similar to the ones of the Ξ^- candidates in Figure 5.26.

In total, 1.1×10^4 events that include the Ω^- candidates in the signal region are selected at this stage. From the MC simulation, 1,972 events are selected, and the corresponding Ω^- reconstruction efficiency is 57%. Further details are described in Appendix A.3. Table 5.4 shows the summary of the selected events at each stage. The numbers of the J/ψ and Λ^0 candidates in the data are the same as those in the Ξ_b^- analysis.

Table 5.4: Summary table of the selected events in the signal region at each stage about the Ω_b^- analysis.

	data	MC
Generated	-	366,998
J/ψ	1.5×10^7	61,377
$\Lambda^0 + \bar{\Lambda}^0$	2.4×10^6	3,252
$\Omega^- + \bar{\Omega}^-$	1.1×10^4	1,972

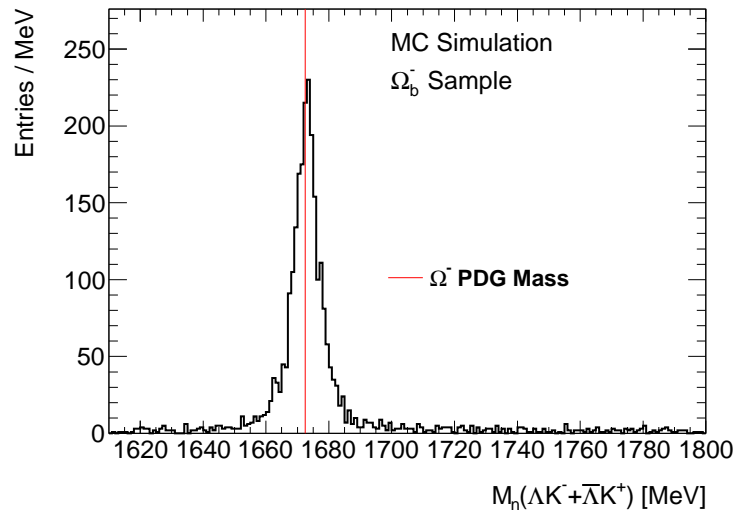
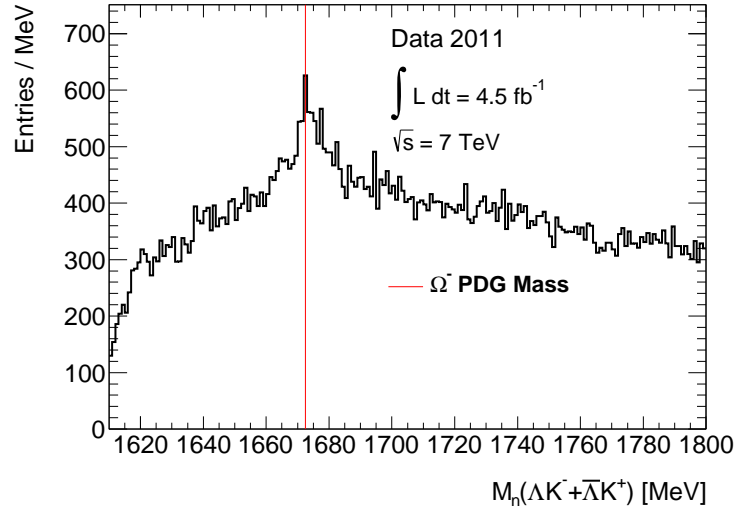


Figure 5.31: Invariant mass distributions of the Ω^- candidates satisfying all requirements in the data and the MC sample.

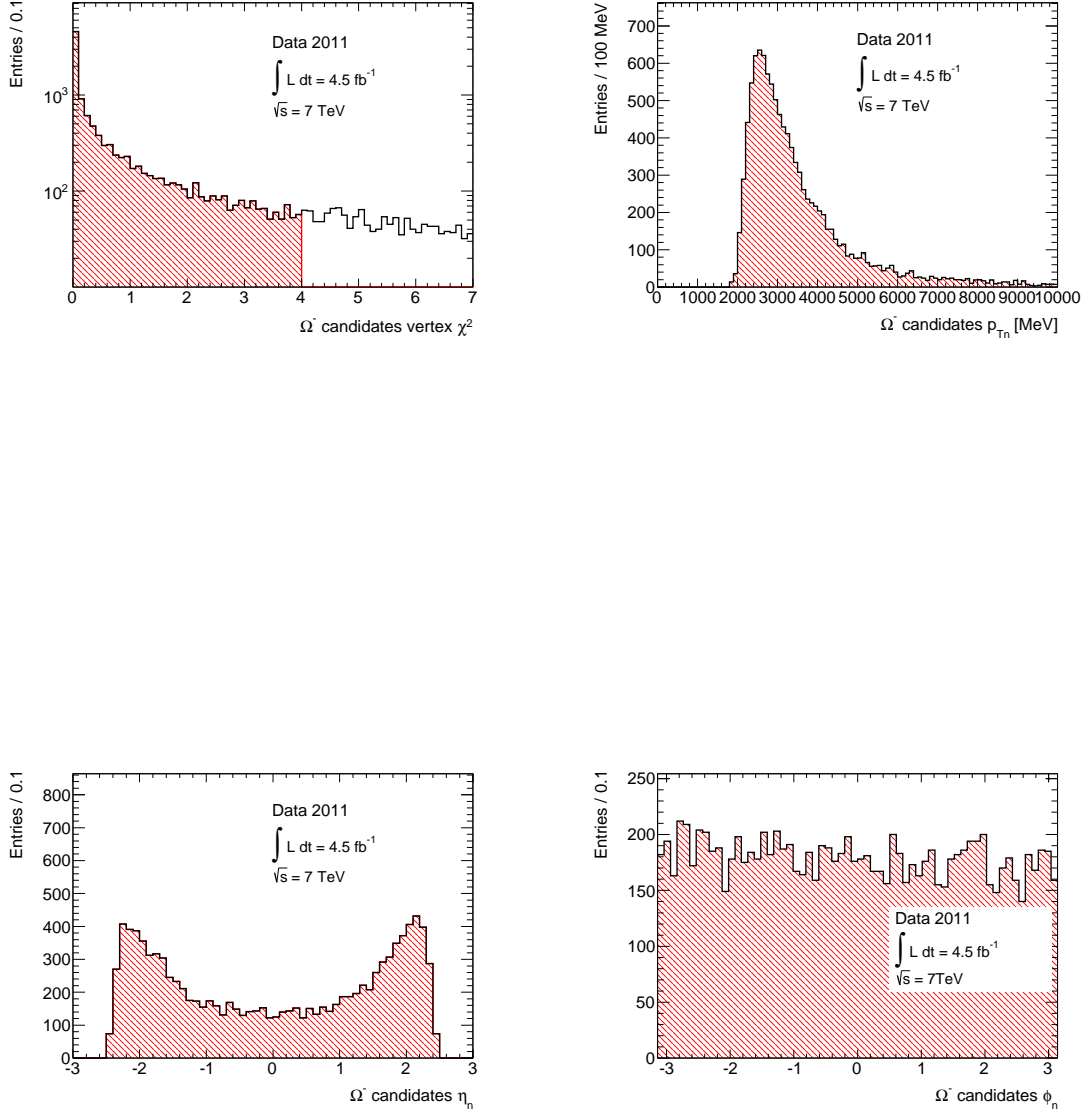


Figure 5.32: χ_n^2 , p_{Tn} , η_n , and ϕ_n distributions of the Ω^- candidates in the signal region.

5.7 Bottom baryon reconstruction

The bottom baryons are reconstructed by refitting the three tracks used in the baryon reconstruction with constraints of the intermediate particle masses of Λ^0 and Ω^-/Ξ^- baryons and the becoming point of the Ω^-/Ξ^- candidate. The point is set to the already reconstructed J/ψ vertex as shown in the image of Figure 5.1. The refit is executed by using the track parameters.

5.7.1 Ω_b^- reconstruction

The proton and pion tracks of the Λ^0 candidate and the kaon track that form the Ω^- candidate in the signal region ($|M_n(\Lambda^0 K^-) - M_{\text{PDG}}(\Omega^-)| \leq 11 \text{ MeV}$) are refitted with constraints of the Λ^0 and Ω^- masses and the becoming point which can be identified as the J/ψ vertex position. Figure 5.33 shows the distributions of the proton and pion track parameters, p_{T0} , η_0 , and ϕ_0 used for the refit. The left side plots show the properties of the proton tracks and the right side for the pion tracks. The black lines show the distributions of all examined tracks and the red ones show those of the tracks successfully refitted. The failure rate is larger in large $|\eta_0|$ regions because the background fraction is large at large $|\eta_0|$.

In total, 5.5×10^3 combinations of the J/ψ and Ω^- candidates are successfully refitted in the data. The refit fails very scarcely in the simulation, as shown in Figure 5.34, because the simulation is applied to the signal samples only. Therefore, these results show that the refit is effective for reducing the background.

Figure 5.35 shows the χ_{pm}^2 distributions for the Λ^0 and Ω^- candidates. The index pm denotes values of the refit with the mass and position constraints. The top plots show the distribution for the Λ^0 candidates and the bottom plots for the Ω^- candidates with a constraint of $\chi_{pm}^2(\Lambda^0) < 30$. The right side plots are those for the data and the left side plots for the MC sample. From a comparison with the MC result, the following quality requirements are applied to purify the Ω_b^- candidates:

- Λ^0 candidates vertex $\chi_{pm}^2 < 30$.
- Ω^- candidates $\chi_{pm}^2 < 15$.

Figure 5.36 shows the p_{Tpm} , η_{pm} , and ϕ_{pm} distributions of the Λ^0 and Ω^- candidates. The left side plots are those for the Λ^0 candidates and the right side plots are for the Ω^- candidates satisfying the condition of $\chi_{pm}^2(\Lambda^0) < 30$.

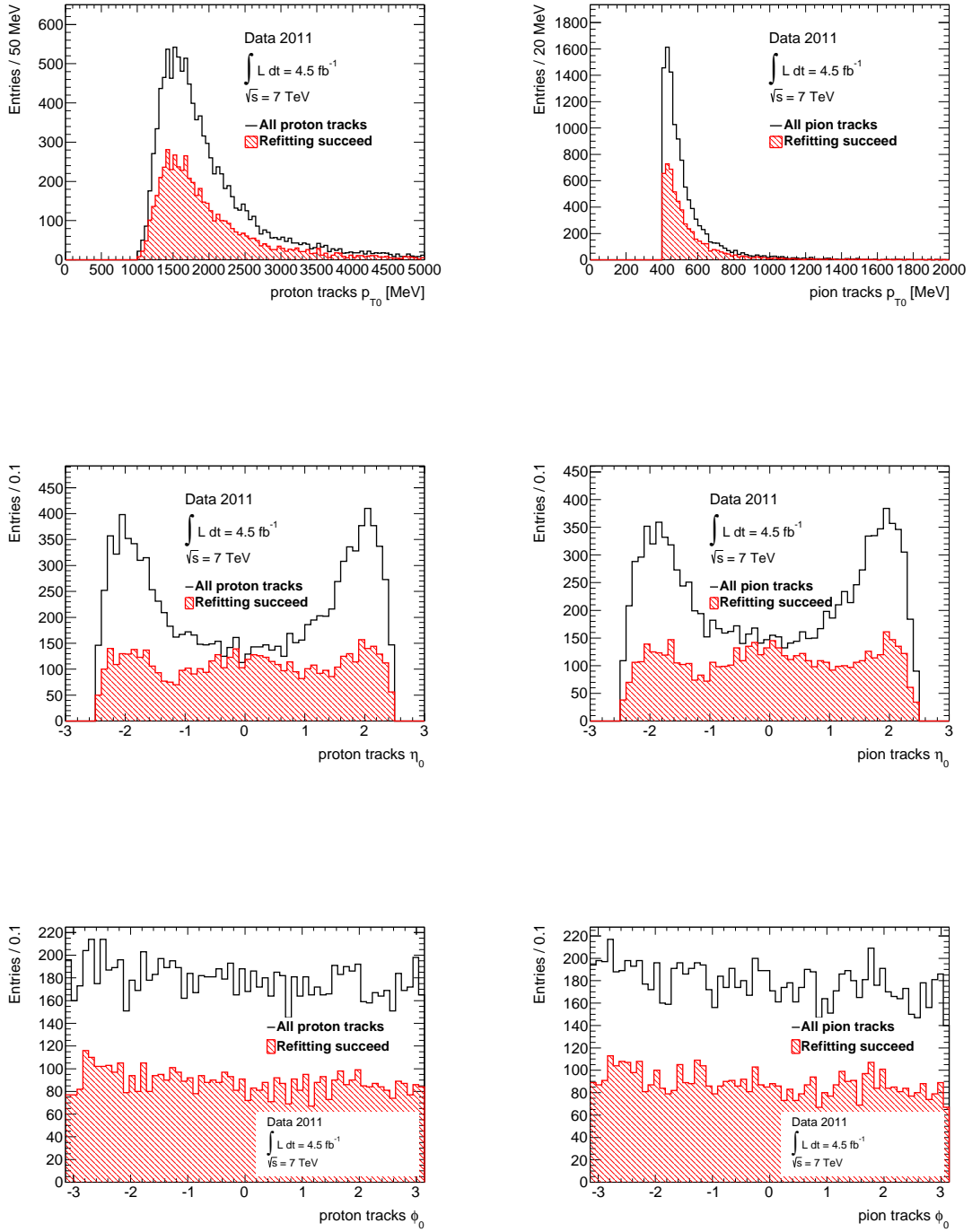


Figure 5.33: p_{T0} , η_0 , and ϕ_0 distributions of the proton and pion track parameters used for the refit for the data.

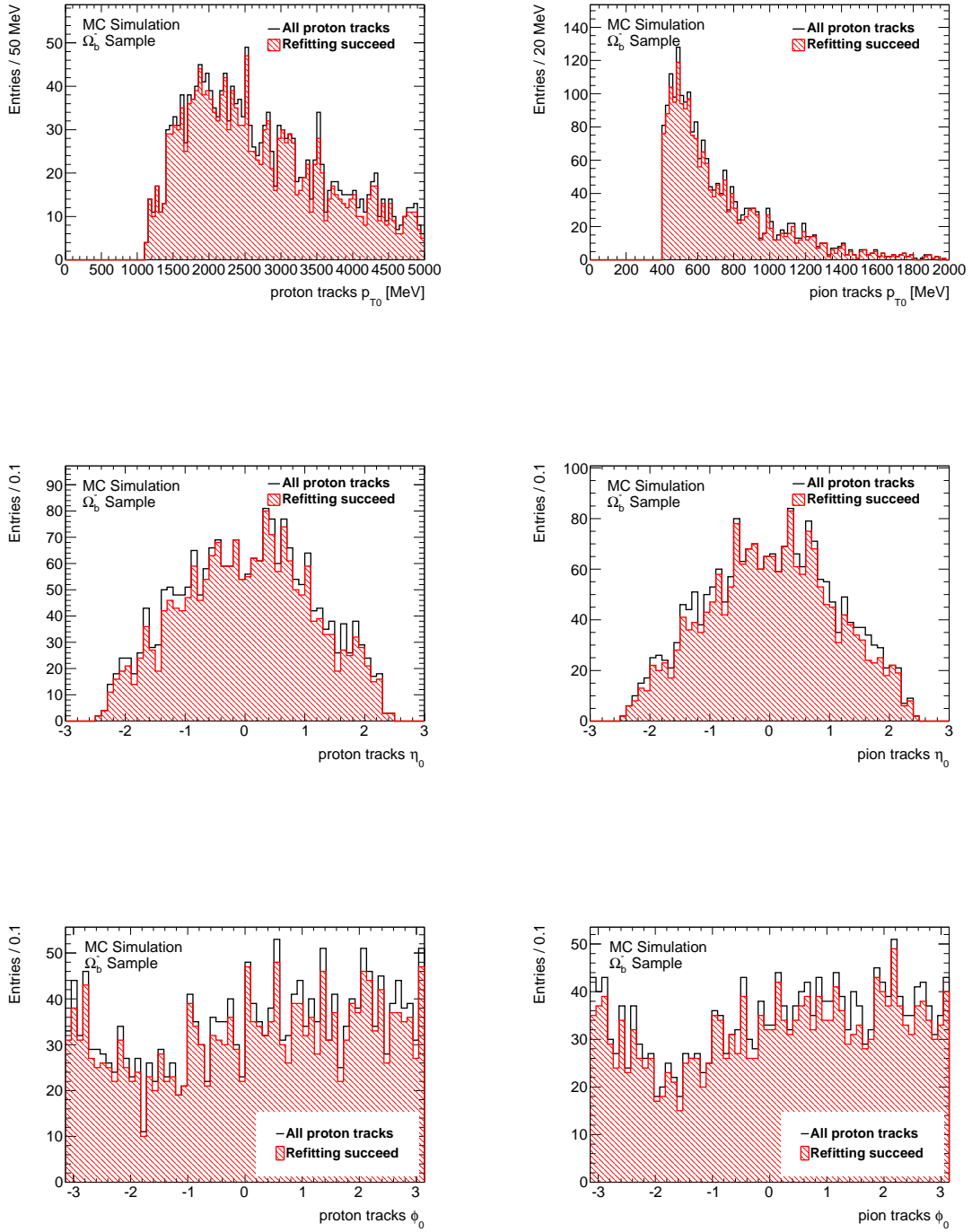


Figure 5.34: p_{T0} , η_0 , and ϕ_0 distributions of the proton and pion track parameters used for the refit for the MC sample.

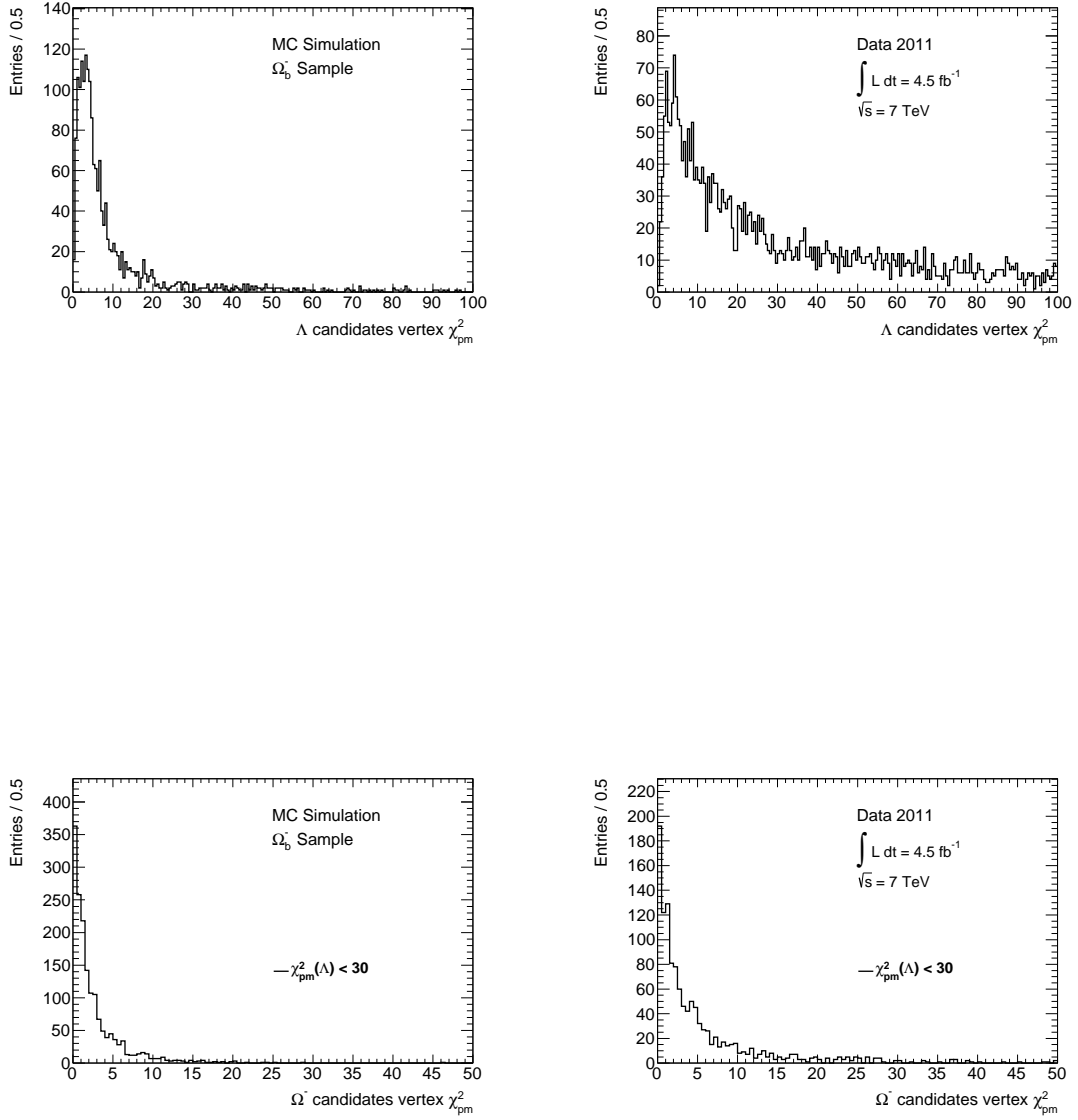


Figure 5.35: χ_{pm}^2 distributions of the Λ^0 and Ω^- candidates in the data and the MC sample.

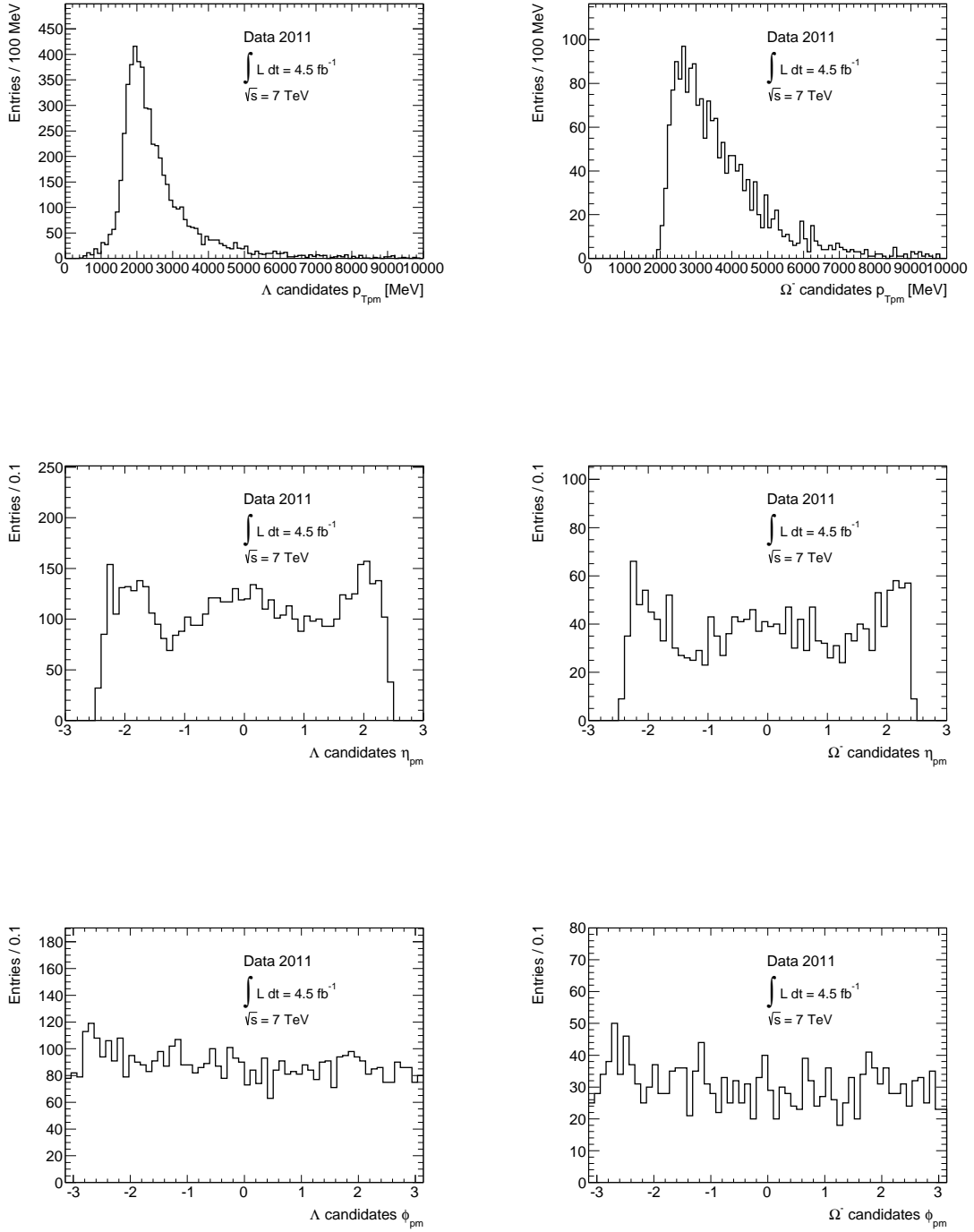


Figure 5.36: p_{Tpm} , η_{pm} , and ϕ_{pm} distributions of the Λ^0 and Ω^- candidates after the refit for the data.

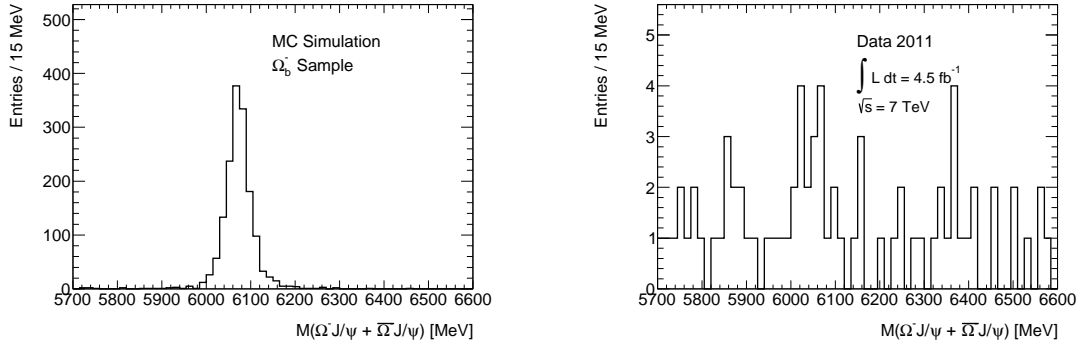


Figure 5.37: Invariant mass distributions of the Ω_b^- candidates in the data (right) and the MC sample (left) satisfying the quality requirements.

The refitted Ω^- candidates and the J/ψ candidates are combined to reconstruct the Ω_b^- candidates. Figure 5.37 shows the invariant mass distributions of the Ω_b^- candidates satisfying the χ_{pm}^2 requirements in the data and the MC sample.

One of the bottom baryons, Λ_b^0 , has been observed by the ATLAS experiment [32] and it has a long lifetime enough ($c\tau = 427 \mu\text{m}$) to distinguish the production point from the decay point. Therefore, it must be natural to consider that other bottom baryons, Ω_b^- and Ξ_b^- , also have $c\tau \sim O(100 \mu\text{m})$, and the requirements on the pointing angle $\cos\theta$ and L_{xy} between the J/ψ vertex and the primary vertex would be effective for reducing the background. Here, the primary vertex is defined as the vertex point that has the largest p_{T0} -sum. The illustration is also shown in Figures 5.38. Figures 5.39 and 5.40 show the $\cos\theta$ and L_{xy} distributions. The MC result within the range of $5970 < M(\Omega^- J/\psi) < 6070 \text{ MeV}$ (signal region), $\pm 100 \text{ MeV}$ around the generated Ω_b^- mass, is plotted in the left side, and the data within all range is plotted.

The following requirements are applied to the Ω_b^- candidates:

- Ω_b^- candidates $\cos\theta > 0.98$.
- Ω_b^- candidates $L_{xy} > 0.08 \text{ mm}$.

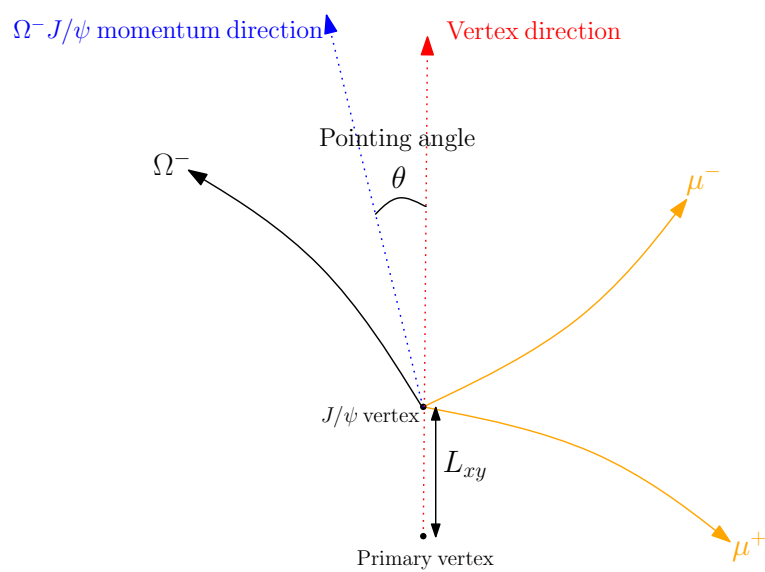


Figure 5.38: Illustration of the pointing angle and L_{xy} for the Ω_b^- analysis.

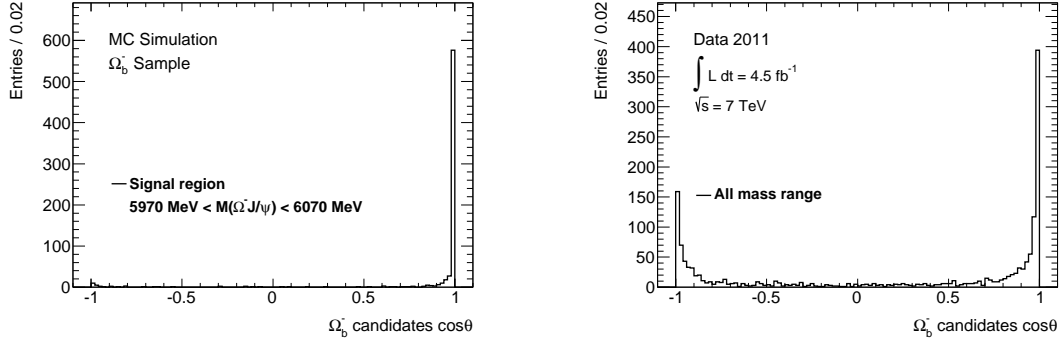


Figure 5.39: $\cos\theta$ distributions of the Ω_b^- candidates in the data and the MC sample.

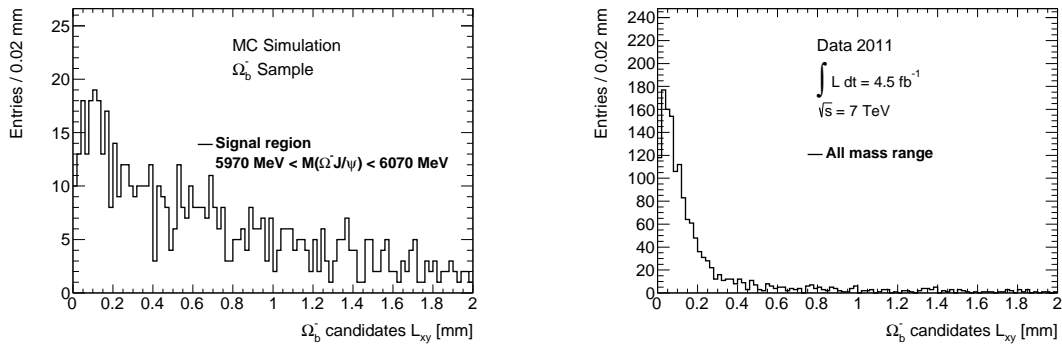


Figure 5.40: L_{xy} distributions of the Ω_b^- candidates in the data and the MC sample.

Figure 5.41 shows the invariant mass distributions of the Ω_b^- candidates that show the effects of these two requirements. The top left plot is the result after applying $\cos\theta > 0.98$, the top right is after applying $L_{xy} > 0.08$ mm, and the bottom is after applying both of them. As you can see, the pointing angle requirement is more effective to reduce the background. A concentration of the candidates around 6050 MeV is visible above a continuous background.

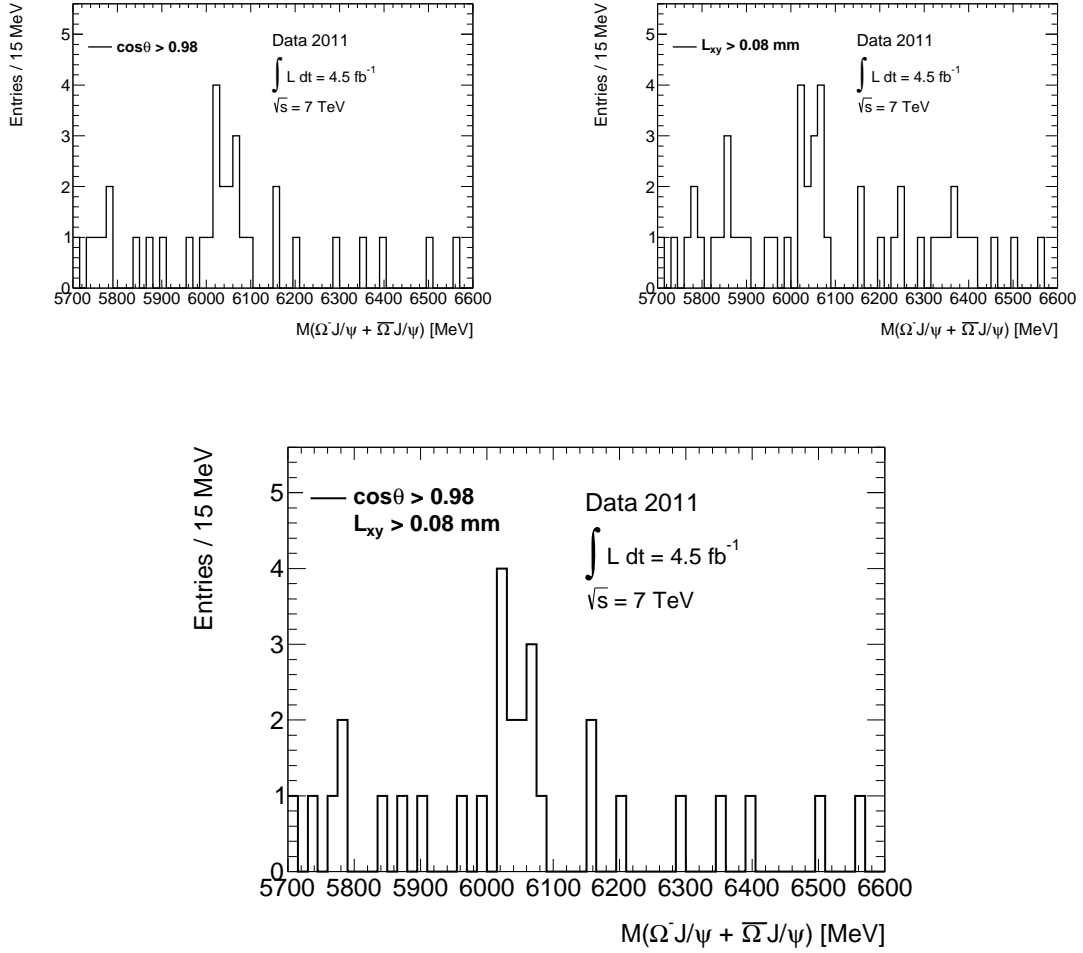


Figure 5.41: Invariant mass distributions of the Ω_b^- candidates satisfying the $\cos\theta$ and L_{xy} requirements.

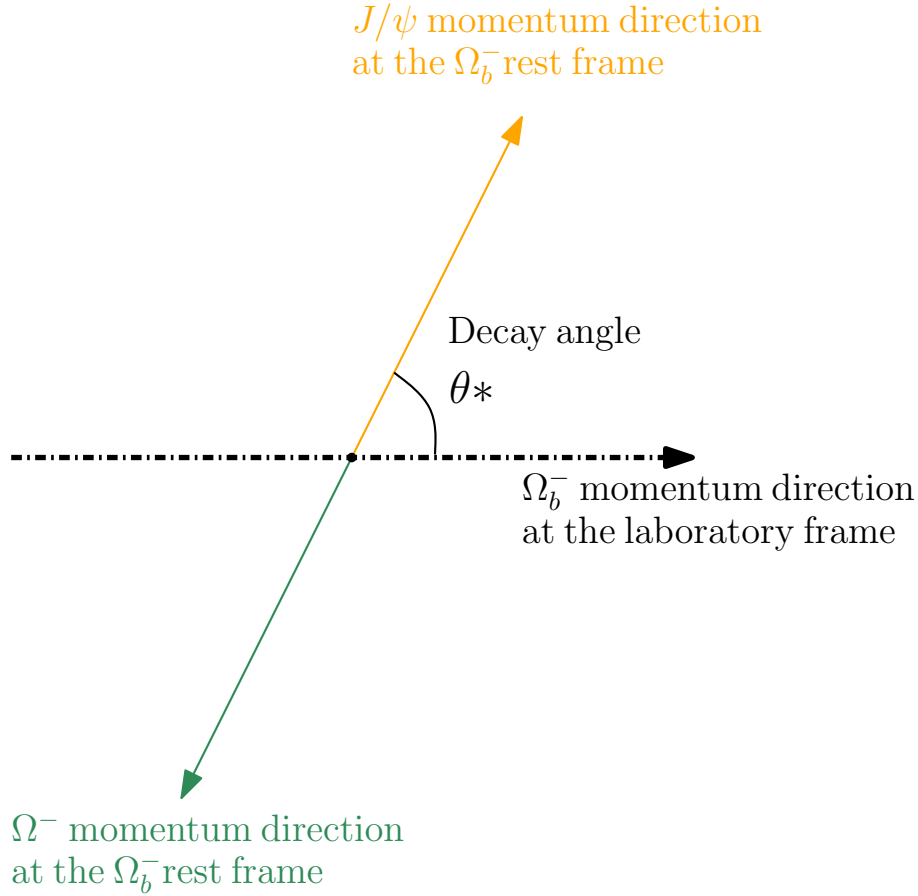


Figure 5.42: Definition of the decay angle.

In order to further reduce the background, another angular requirement is imposed to the Ω_b^- candidates. The decay angle, θ^* , is defined as the angle between the momentum direction of the Ω_b^- candidate in the laboratory frame and that of the J/ψ candidate in the Ω_b^- rest frame, as illustrated in Figure 5.42. Figure 5.43 shows the $\cos\theta^*$ distributions of the candidates in the data and the MC sample. The simulation result, which is dominated by the signal, has a peak at $\cos\theta \sim 0.7$ with a gentle curve, while the data has an enhancement at $\cos\theta \sim 1$. Therefore, a cut using this quantity is applied:

- $\cos\theta^* < 0.9$.

Figure 5.44 shows the invariant mass distributions of the Ω_b^- candidates after applying this requirement to the Ω_b^- candidates shown in Figure 5.41 (bottom). Figure 5.45 shows the invariant mass distribution of the corresponding Ω_b^- signals in the MC sample. In total, 23 candidates are retained in the draw range of Figure 5.44 and 1,208 candidates remain in the MC sample. The p_T , η , and ϕ distributions are shown in Figure A.10 in Appendix A.4.

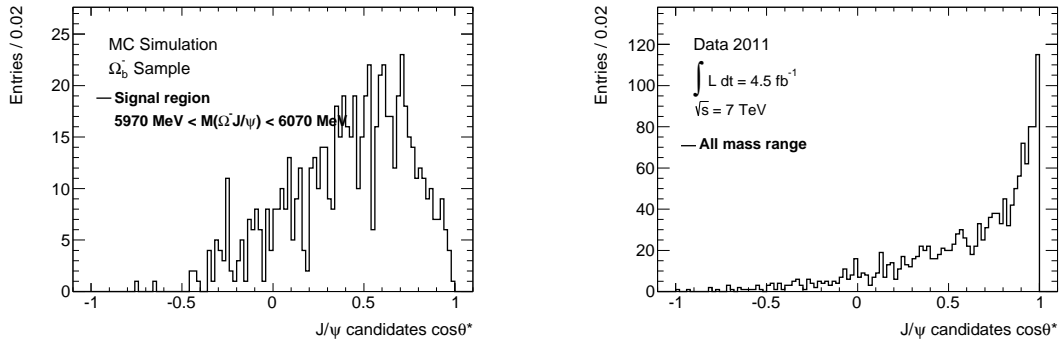


Figure 5.43: $\cos \theta^*$ distributions of the Ω_b^- candidates in the data and the MC sample.

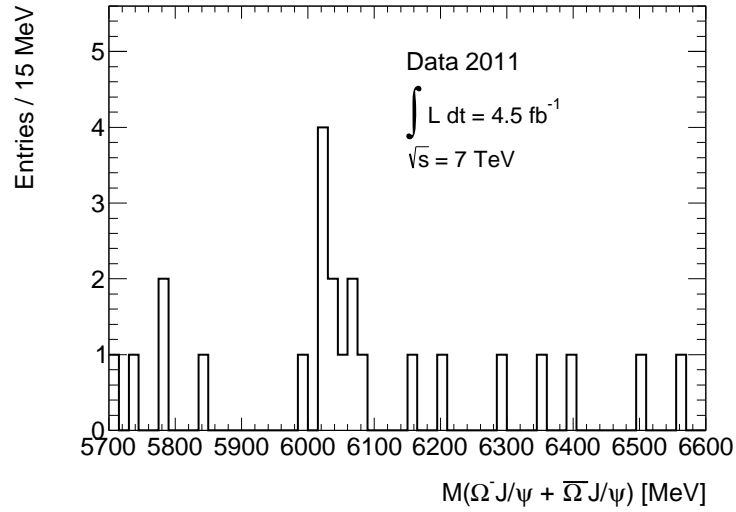


Figure 5.44: Invariant mass distribution of the final Ω_b^- candidates in the data.

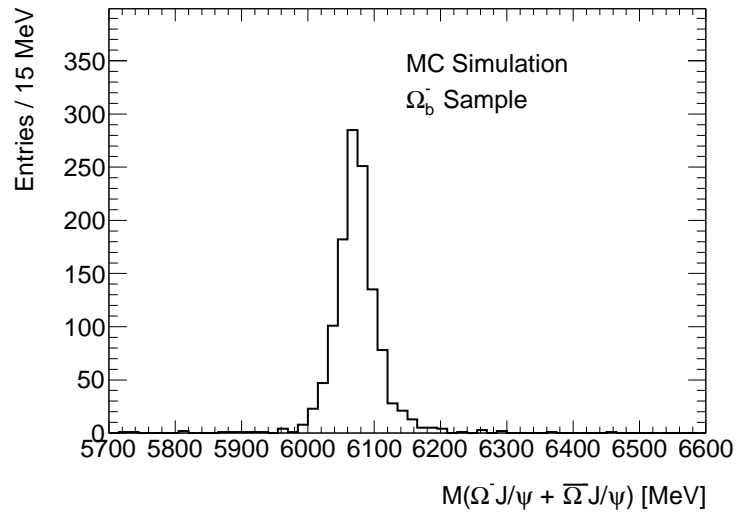


Figure 5.45: Invariant mass distribution of the Ω_b^- candidates in the MC sample after applying all requirements.

5.7.2 Ξ_b^- reconstruction

The Ξ_b^- candidates are selected using the method similar to that for the Ω_b^- analysis. Figure 5.46 shows the χ_{pm}^2 distributions of the Λ^0 and Ξ^- candidates. The top plots show those for the Λ^0 candidates and the bottom plots show for the Ξ^- candidates satisfying $\chi_{pm}^2(\Lambda^0) < 30$. The right side plots show those for the data and the left side plots show for the MC sample. Other relevant plots are shown in Appendix A.5.

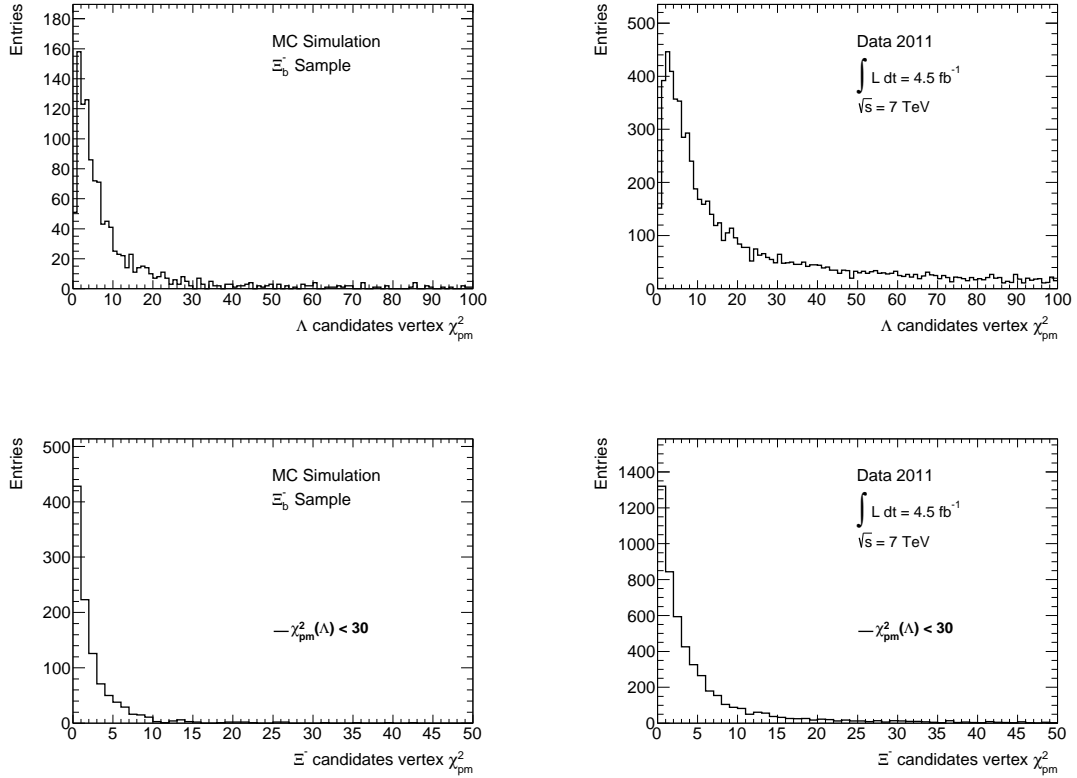


Figure 5.46: χ_{pm}^2 distributions of the Λ^0 and Ξ^- candidates in the data and the MC sample.

The following conditions are required in the Ξ_b^- reconstruction:

- Λ^0 candidates vertex $\chi_{pm}^2 < 30$.
- Ξ^- candidates $\chi_{pm}^2 < 15$.

The Ξ_b^- candidates are reconstructed by combining the refitted Ξ^- candidates and the J/ψ candidates. Figure 5.47 shows the invariant mass distributions of the Ξ_b^- candidates in the data and the MC sample. The Ξ_b^- signal is still unclear in this plot.

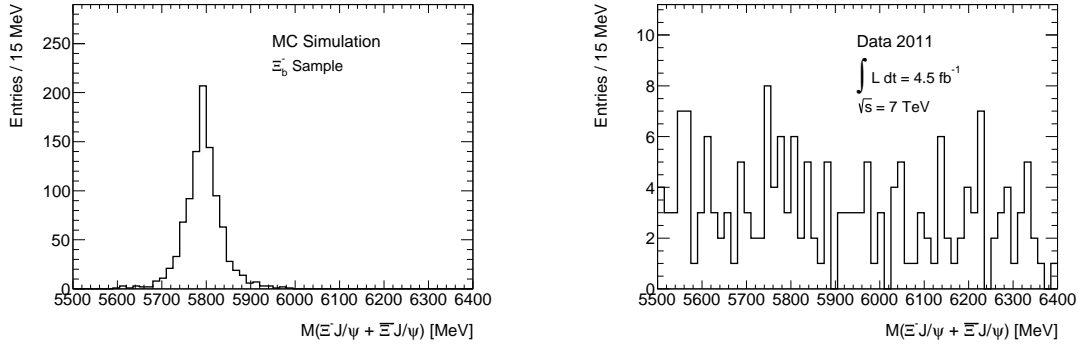


Figure 5.47: Invariant mass distributions of the Ξ_b^- candidates satisfying the quality requirements in the data (right) and the MC sample (left).

The requirements on the pointing angle $\cos\theta$, L_{xy} , and $\cos\theta^*$ are also applied to reduce the background. Figures 5.48, 5.49, and 5.50 show the corresponding distributions. In these figures, the left side plots show the MC results within the range of $5690 < M(\Xi^- J/\psi) < 5890$ MeV (signal region), which is ± 100 MeV around the generated Ξ_b^- mass. The requirements applied in the Ξ_b^- reconstruction are

- Ξ_b^- candidates $\cos\theta > 0.98$,
- Ξ_b^- candidates $L_{xy} > 0.1$ mm,
- $\cos\theta^* < 0.9$.

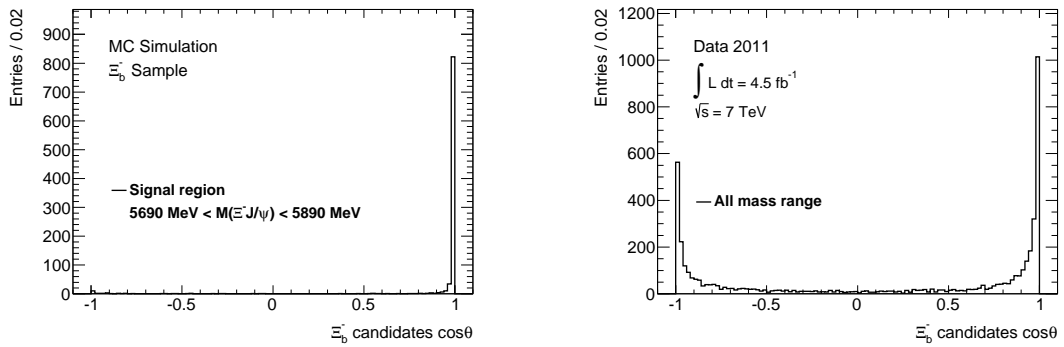


Figure 5.48: $\cos\theta$ distribution of the Ξ_b^- candidates in the data and the MC sample.

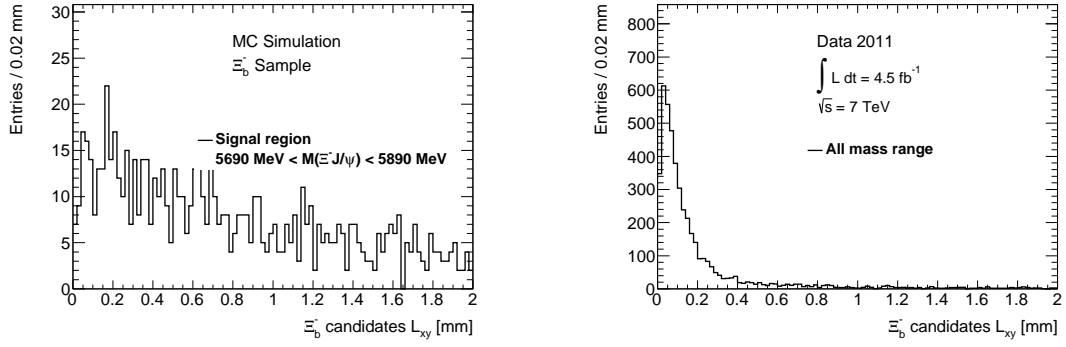


Figure 5.49: L_{xy} distribution of the Ξ_b^- candidates in the data and the MC sample.

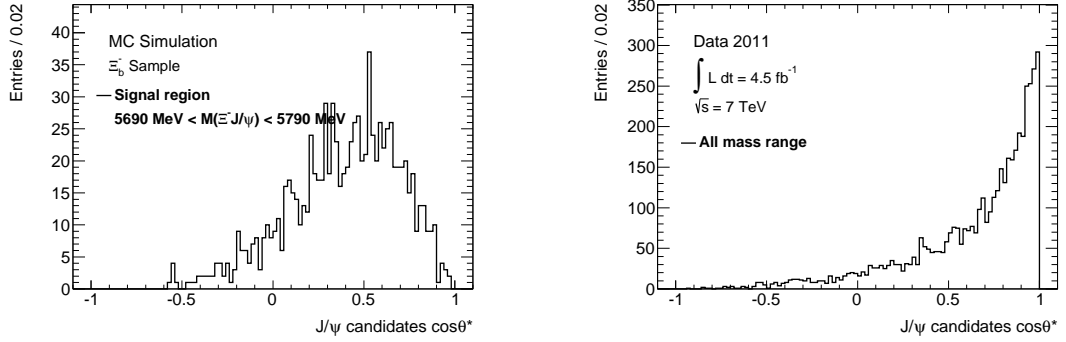


Figure 5.50: $\cos\theta^*$ distribution of the Ξ_b^- candidates in the data and the MC sample.

Figure 5.51 shows the invariant mass distributions of the Ξ_b^- candidates satisfying the listed requirements. The top left plot is obtained with $\cos\theta > 0.98$, the top right plot is obtained with $L_{xy} > 0.1$ mm, and the bottom plot is obtained with the both. The distribution of the final Ξ_b^- candidates satisfying all three requirements is shown in Figure 5.52 and the corresponding distribution of the MC sample is shown in Figure 5.53. A concentration of the candidates around 5800 MeV, which corresponds to the Ξ_b^- signal, is visible in the data.

Finally, in total of 45 candidates are retained within the draw range of Figure 5.52, while 835 candidates in the MC sample are selected. The p_T , η , and ϕ distributions are shown in Figure A.14 in Appendix A.6.

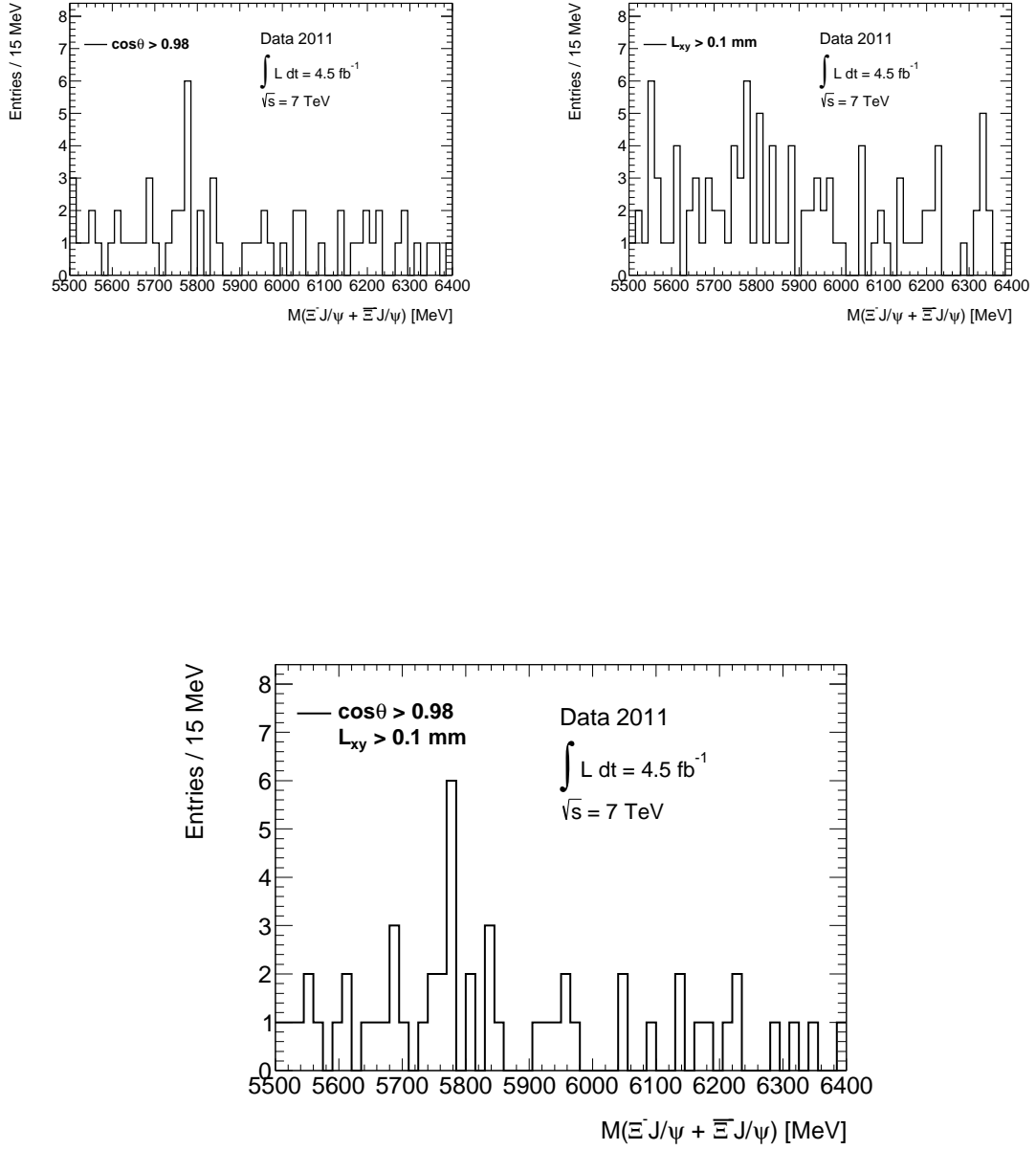


Figure 5.51: Invariant mass distributions of the Ξ_b^- candidates satisfying the $\cos\theta$ and L_{xy} requirements.

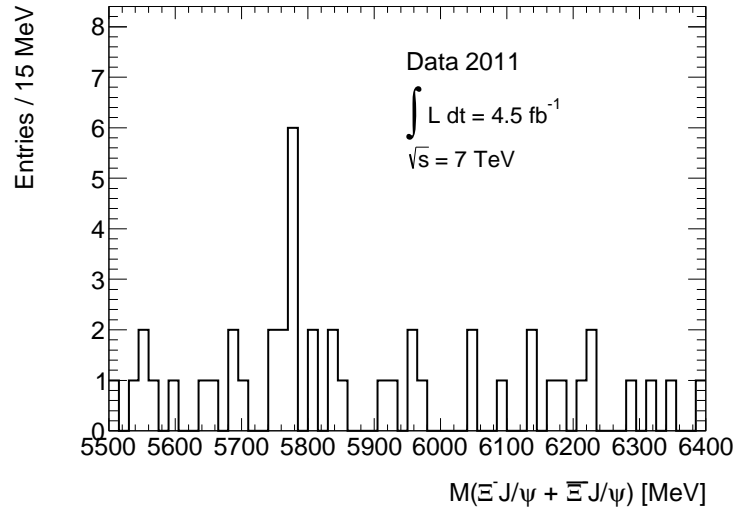


Figure 5.52: Invariant mass distribution of the Ξ_b^- candidates satisfying all requirements in the data.

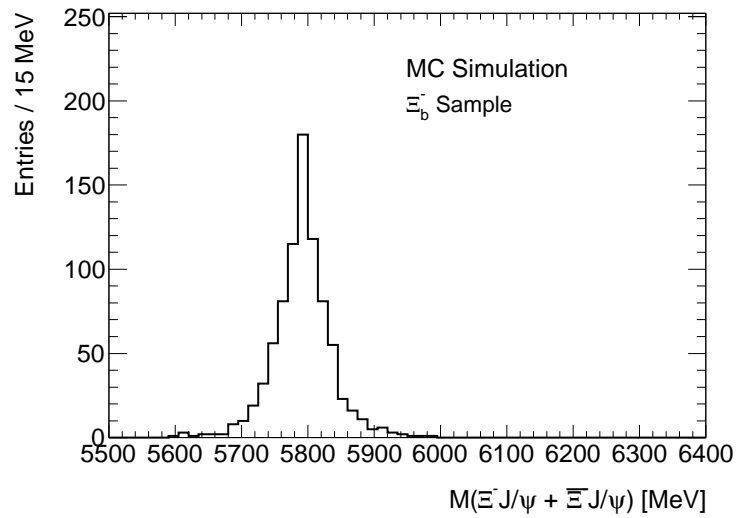


Figure 5.53: Invariant mass distribution of the Ξ_b^- candidates satisfying all requirements in the MC sample.

Chapter 6

Results

6.1 Mass measurements

As a faint but peak-like structures have been observed in each invariant mass distribution, the masses and signal strengths of the Ω_b^- and Ξ_b^- signals are determined from the obtained mass distributions show in Figures 5.44 and 5.52.

6.1.1 Unbinned maximum likelihood fit

The mass distributions are fitted with a probability density function (*p.d.f.*) $P(M)$ [37]:

$$P(M) = fS(M) + (1 - f)B(M). \quad (6.1)$$

Here, the parameter f is the fraction of the signal to be solved by the fit. The function $S(M)$ is a shape of the signal and the function $B(M)$ is that of the background. Both of the functions $S(M)$ and $B(M)$ are normalized to one, and a range for f is $0 < f < 1$. As the number of events are small, the unbinned maximum likelihood fit is used. Details of the fit procedure is described in Appendix B. In this analysis, the function $S(M)$ is hypothesized to be the *Double Gaussian* as discussed in the next subsection and the function $B(x)$ is a *Constant*. This fit has been performed using The RooFit toolkit [38].

6.1.2 Signal *p.d.f.*

The signal function form can not be determined by the data themselves, so that the function form is determined by the mass distributions of the MC samples shown in Figure 5.45 for the Ω_b^- analysis and in Figure 5.53 for the Ξ_b^- analysis. The double Gaussian form is used as the function $S(M)$ because the distributions show longer

tails than the Gaussian form;

$$S(M) = f'G(m^G, \sigma^1; M) + (1 - f')G(m^G, \sigma^2; M), \quad (6.2)$$

where $G(m^G, \sigma)$ is the Gaussian function, m^G is its mean value, and σ is the Gaussian width. A range for f' is $0 < f' < 1$.

The fit range of Equation (6.1) is between 5700 MeV and 6600 MeV for the Ω_b^- candidates and is between 5500 MeV and 6400 MeV for the Ξ_b^- candidates. Table 6.1 shows the summary of the obtained fit parameters. Each obtained m^G value is consistent with the generated mass which is also shown in the table. Figure 6.1 shows the results overlaid on the MC samples shown in Figures 5.45 and 5.53.

Table 6.1: Summary table of the fit parameters (MC).

Particle	Ω_b^-	Ξ_b^-
Generated	6071.0 MeV	5791.1 MeV
m_{MC}^G	6072.0 ± 0.8 MeV	5791.9 ± 1.3 MeV
σ^1	20.6 ± 1.6 MeV	27.8 ± 2.0 MeV
σ^2	47.3 ± 4.7 MeV	70.7 ± 5.9 MeV
f'	0.67 ± 0.08	0.71 ± 0.06
f	0.98 ± 0.01	1.0 ± 0.0

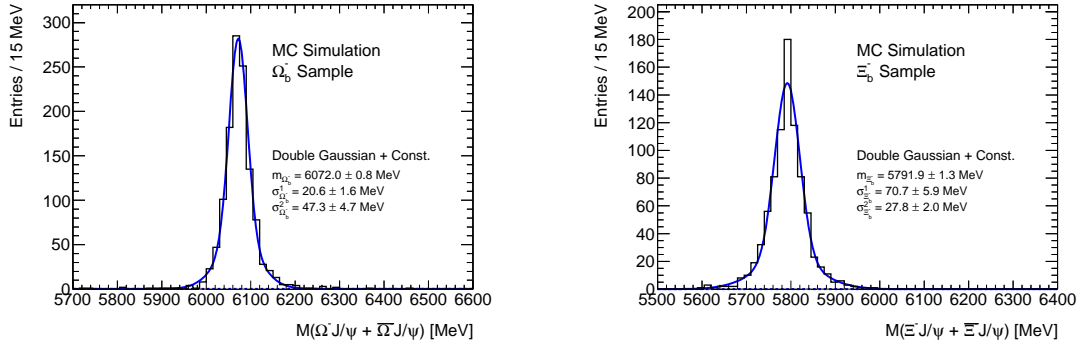


Figure 6.1: Invariant mass distributions of the Ω_b^- (left) and Ξ_b^- (right) candidates with the fit for the MC samples.

For a cross check, a fit with the single Gaussian function was tested, too. The fit to the MC samples is worse as shown in Figure C.1 in Appendix C, but the final results of the determination of the masses and the signal strengths for the data change little compared with their statistical errors.

6.1.3 Fit results

As the function form of $S(M)$ is determined, fit to the invariant mass distributions for the Ω_b^- candidates (Figure 5.44) and the Ξ_b^- candidates (Figure 5.52) are performed. The fit ranges are the same as those of the MC samples. Obtained m^G , f , and the number of events $N_{\text{data}}^{\text{All}}$ in the fit range are shown in Table 6.2. The number of signals $N_{\text{data}}^{\text{Sig}}$ is obtained as $f \times N_{\text{data}}^{\text{All}}$ and is also shown in the table, as well as the number of the background $N_{\text{data}}^{\text{Bkg}}$.

Table 6.2: Summary table of the obtained parameters (Data).

Particle	$N_{\text{data}}^{\text{All}}$	m_{data}^G	f	$N_{\text{data}}^{\text{Sig}}$	$N_{\text{data}}^{\text{Bkg}}$
Ω_b^-	23 ± 4.8	$6035.8 \pm 10.6 \text{ MeV}$	0.39 ± 0.12	9.0 ± 3.3	14.0 ± 4.0
Ξ_b^-	45 ± 6.7	$5775.9 \pm 12.8 \text{ MeV}$	0.24 ± 0.09	10.9 ± 4.2	34.1 ± 6.4

Figures 6.2 and 6.3 show the fit results. The background components are indicated in the blue dashed lines. In these plots, the fitted lines are normalized with the adopted bin width, which is 15 MeV. The statistical significance of the peak appears with the expected width at the obtained mass position is determined by yields of the signal and background events in a limited mass window. Here, the mass range is set between $m_{\text{data}}^G - 2\sigma$ and $m_{\text{data}}^G + 2\sigma$. The results are shown in Table 6.3. The significance of the Ω_b^- signals is 3.6 standard deviations and that of the Ξ_b^- signals is 2.9 standard deviations. These calculations have been performed using `RooStats` [39].

Although the significance level is below 5 sigma so that one cannot claim the ‘discovery’ of the either Ω_b^- or Ξ_b^- state, the obtained peaks are located to the positions which are consistent with those claimed by the other experiments.

An attempt was made if the significance could increase by optimizing the selection cut. In Appendix D.1, the significance as a function of the $\cos\theta^*$ cut is shown. It is found that the default cut position of $\cos\theta^* < 0.9$ is nearly optimal.

Table 6.3: Summary table of the signal and background yields.

Particle	Signal	Background	Significance
Ω_b^-	8.6 ± 3.2	1.8 ± 0.5	3.6
Ξ_b^-	10.4 ± 4.0	6.1 ± 1.1	2.9

In summary, the peak structures in the $\Omega^- J/\psi$ and $\Xi^- J/\psi$ systems are observed with the significances of 3.6σ and 2.9σ , respectively. The peak positions are

$$\begin{aligned}
 M(\Omega^- J/\psi) &= 6035.8 \pm 10.6 \text{ MeV}, \\
 M(\Xi^- J/\psi) &= 5775.9 \pm 12.8 \text{ MeV}.
 \end{aligned}$$

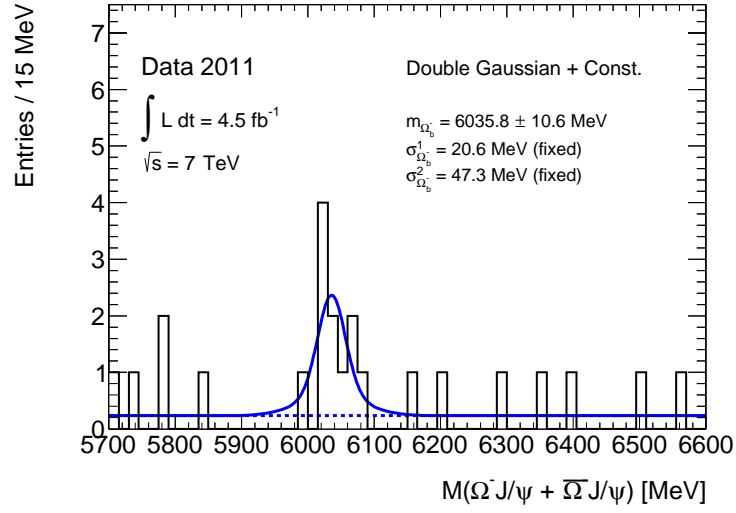


Figure 6.2: Invariant mass distributions of the Ω_b^- candidates with the fit for the data.

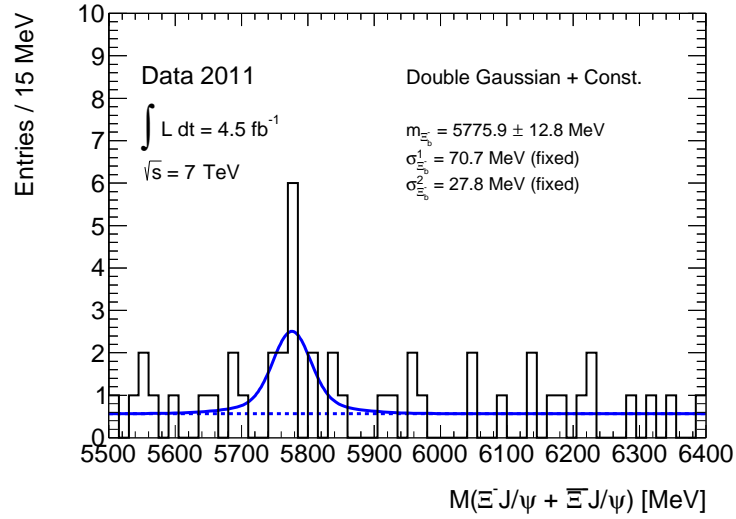


Figure 6.3: Invariant mass distributions of the Ξ_b^- candidates with the fit for the data.

6.1.4 Systematic uncertainties

The systematic uncertainty in the mass measurement can be estimated by evaluating the shifts with respect to the baseline value in the extracted mass. In this analysis, following three sources for the shift are considered 1) track reconstruction biases, 2) an uncertainty of the tracking momentum scale, and 3) inaccurate modeling of the amount of material in the inner detectors. Each observed shift is added in quadrature. This value is quoted as the systematic uncertainty. The observed shifts are summarized in Table 6.4 and the details are following.

Table 6.4: Summary table of the systematic uncertainties of the masses.

Syst. uncertainty	$\Delta m_{\Omega_b^-}$	$\Delta m_{\Xi_b^-}$
Reconstruction bias	± 1.0 MeV	± 0.8 MeV
Momentum scale	$+6.7$ MeV	$+5.8$ MeV
ID material	± 0.3 MeV	± 0.3 MeV
Total	$^{+6.7}_{-1.1}$ MeV	$^{+5.9}_{-0.8}$ MeV

Reconstruction bias

The bias originated from the reconstruction procedure mainly comes from the vertex fit. It is also influenced by the various cut parameters such as the p_T and η thresholds of the tracks. In order to estimate the overall biases, the shifts between the true (generated) and measured masses in the MC samples are used. As listed in Table 6.1, the two values are within 1.3σ of the measurement. Therefore, it is consistent to no bias. To be conservative, nevertheless, the differences between the two values are assigned the systematic uncertainties. These give ± 1.0 MeV for the Ω_b^- mass and ± 0.8 MeV for the Ξ_b^- mass.

Uncertainty of the tracking momentum scale

The uncertainty of the tracking momentum scale is evaluated by the differences of the reconstructed masses of the selected J/ψ , Ω^- , and Ξ^- candidates. Table 6.5 is the summary of the masses from the data and the MC samples. These values are obtained by the binned fit with the Gaussian + polynomial function on Figure 5.7, 5.31, and 5.25 for the J/ψ , Ω^- , and Ξ^- candidates, respectively. The fitted curves are shown in Figure 6.4.

As for the J/ψ candidates, the mass obtained from the distribution is +0.19% larger. Assuming this difference comes from the uncertainty of the absolute scale of

Table 6.5: Summary table of the fitted masses and the tracks momenta scale shifts.

Particles	J/ψ	Ω^-	Ξ^-
MC Masses	3101.1 ± 0.1 MeV	1672.91 MeV	1321.66 MeV
Data Masses	3095.1 ± 0.2 MeV	1673.98 MeV	1322.55 MeV
Mom. shifts	+0.19%	-0.063%	-0.067%

the muon momentum, the momentum of the data is shifted by +0.19%. Similarly, momenta of the Λ and K^- candidates from the Ω^- decay is shifted by -0.063% and those of the Λ and π^- from the Ξ^- decay is shifted by -0.067% to align the mass peak positions of the data to the MC sample. The masses of the Ω_b^- and Ξ_b^- candidates are calculated after these scaling, and the unbinned maximum likelihood fit are repeated. The differences from the standard analysis are assigned to the systematic uncertainties. These results are shown in Table 6.4. The mass distributions with the shifted tracks are shown in Appendix D.2.

Uncertainty in the amount of material in the inner detectors

The particle energy loss is estimated by the tracking algorithm using the ATLAS material map. Therefore, inaccurate modeling of the amount of material in the inner detectors could affect the measurements. This uncertainty was studied by the ATLAS $\Lambda_b^0 \rightarrow J/\psi(\mu^+\mu^-)\Lambda(p^+\pi^-)$ analysis, and the mass shift of ± 0.2 MeV is reported [32]. In this analysis, ± 0.3 MeV is conservatively quoted as the uncertainties since the number of used tracks increase from four to five.

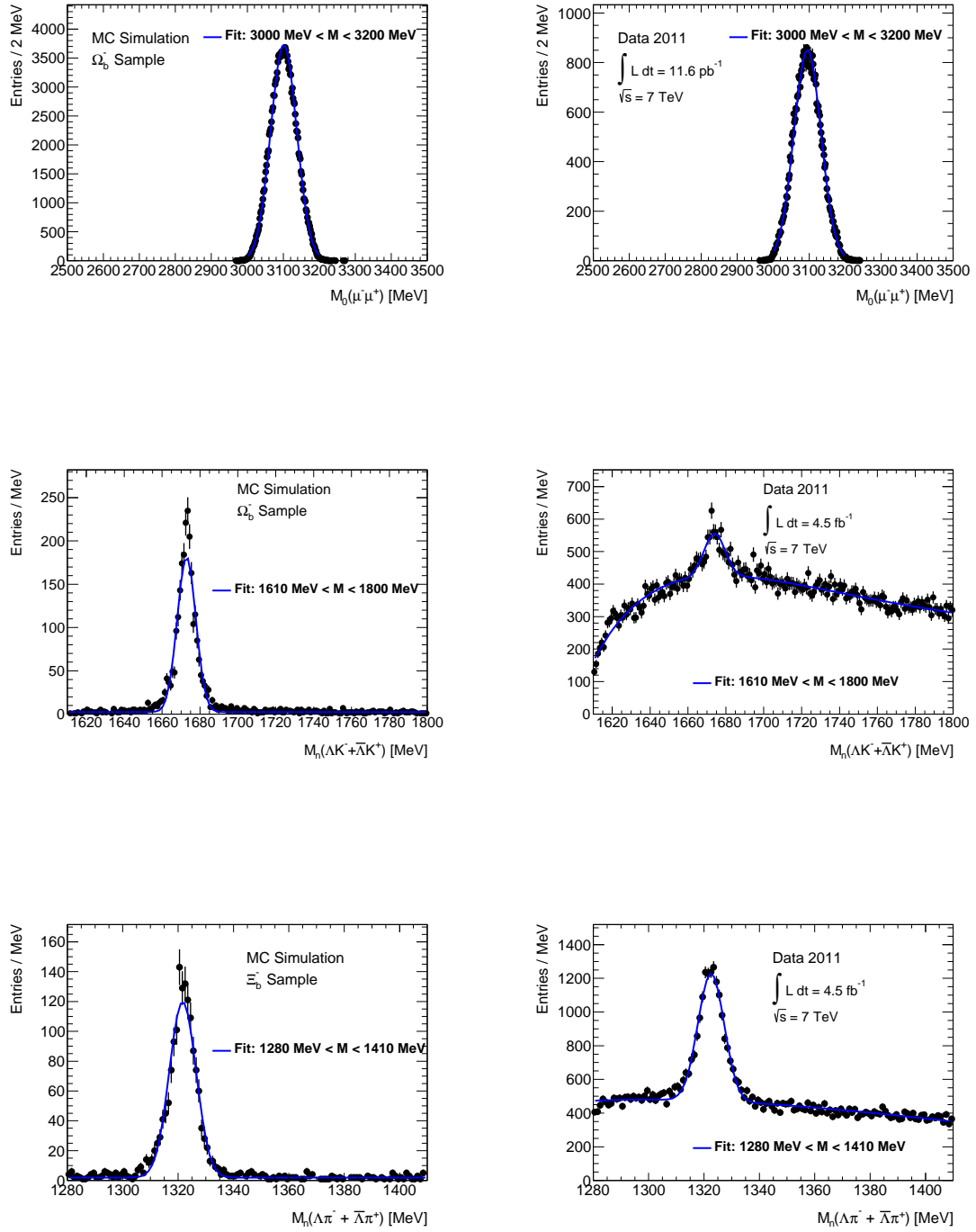


Figure 6.4: The J/ψ , Ω^- , and Ξ^- mass distributions from the data (right) and the MC samples (left) with the fitted curves.

6.1.5 Mass results

The estimated masses of the Ω_b^- and Ξ_b^- baryons with the statistical and systematic uncertainties are:

$$M_{\Omega_b^-} = 6035.8 \pm 10.6(\text{stat.})_{-1.1}^{+6.7}(\text{syst.}) \text{ MeV},$$

$$M_{\Xi_b^-} = 5775.9 \pm 12.8(\text{stat.})_{-0.8}^{+5.9}(\text{syst.}) \text{ MeV}.$$

These values are compared with the results of the other experiments in Figure 6.5 and 6.6. They are consistent with the average PDG values [13]. As described in Chapter 2, the D0 experiment significantly reported the higher value for the Ω_b^- mass [10]. This measurement does not support it.

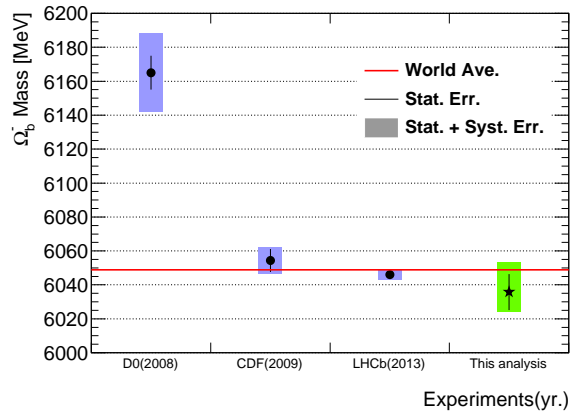


Figure 6.5: The Ω_b^- masses at each experiment.

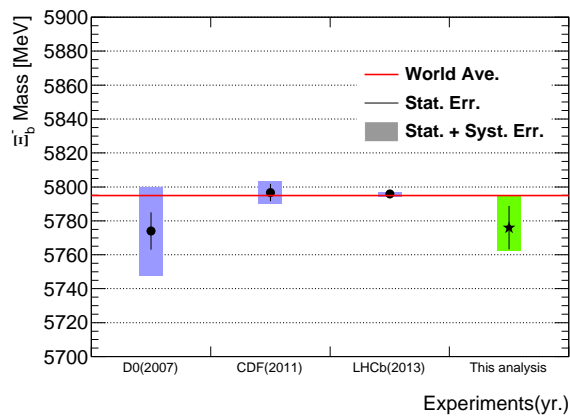


Figure 6.6: The Ξ_b^- masses at each experiment.

6.2 Production cross sections

From the obtained $N_{\text{data}}^{\text{Sig}}$, the production cross sections of the Ω_b^- and Ξ_b^- baryons are estimated. As the signal is extracted from the $\Omega^- J/\psi$ ($\Xi^- J/\psi$) invariant mass and as the branching fraction to this decay mode is unknown, obtained values are the product of the production cross sections and the branching ratio. It is estimated from $N_{\text{data}}^{\text{Sig}}$ with the following relation;

$$\sigma_{\Omega_b^-} \times B_r(\Omega_b^- \rightarrow J/\psi \Omega^-) = N_{\text{data}}^{\text{Sig}} \frac{1}{\mathcal{L}} \frac{1}{\epsilon} \frac{1}{B_r(J/\psi \rightarrow \mu^+ \mu^-)} \frac{1}{B_r(\Omega^- \rightarrow \Lambda^0 K^-)} \frac{1}{B_r(\Lambda^0 \rightarrow p \pi^-)}. \quad (6.3)$$

For the Ξ_b^- analysis, $B_r(\Omega^- \rightarrow \Lambda^0 K^-)$ is replaced with $B_r(\Xi^- \rightarrow \Lambda^0 \pi^-)$. The used branching ratios are summarized in Table 5.2. \mathcal{L} is the integrated luminosity, $N_{\text{data}}^{\text{Sig}}$ is the total signal yields listed in Table 6.2, and ϵ is the efficiency of this analysis. Since the properties of the Ω_b^- and Ξ_b^- baryons are not well-known, the ϵ values are model dependent. In this analysis, ϵ is estimated using the PYTHIA MC model that has been used in the detector simulation. The ϵ values are simply estimated as

$$\epsilon = \frac{N_{\text{MC}}^{\text{Sig}}}{N^{\text{Gen}}}, \quad (6.4)$$

where $N_{\text{MC}}^{\text{Sig}}$ is the total signal yields of the MC sample and N^{Gen} is the number of generated bottom baryons.

Table 6.6: Parameters used for evaluating the production cross sections.

Particle	Ω_b^-	Ξ_b^-
$N_{\text{data}}^{\text{Sig}}$	8.98 ± 3.34	10.91 ± 4.21
$N_{\text{MC}}^{\text{Sig}}$	1185.88 ± 34.67	835 ± 28.91
N^{Gen}	366998	517119
ϵ	$(3.23 \pm 0.0944) \times 10^{-3}$	$(1.62 \pm 0.0559) \times 10^{-3}$

Since the MC samples are generated with the conditions of $p_T > 6 \text{ GeV}$ and $|\eta| < 2.7$ for the bottom baryons and $p_T > 3.5 \text{ GeV}$ and $|\eta| < 2.5$ for at least one of the two muons from the J/ψ decay, the production cross sections are first measured within this fiducial volume (denoted as $\sigma^{\text{F.V.}}$). The obtained production cross section values are

$$\begin{aligned} \sigma_{\Omega_b^-}^{\text{F.V.}} \times B_r(\Omega_b^- \rightarrow J/\psi \Omega^-) &= 24.1 \pm 9.0 \text{ pb}, \\ \sigma_{\Xi_b^-}^{\text{F.V.}} \times B_r(\Xi_b^- \rightarrow J/\psi \Xi^-) &= 39.7 \pm 15.4 \text{ pb}. \end{aligned}$$

In the simulation of the muon selection, the fractions of the Ω_b^- and Ξ_b^- samples to fall in the fiducial volume are recorded. The recorded values are 0.131 and 0.141, respectively. The errors of these values are negligible. Using these values, the obtained production cross sections under the bottom baryon conditions of $p_T > 6$ GeV and $|\eta| < 2.7$ are

$$\begin{aligned}\sigma_{\Omega_b^-} \times B_r(\Omega_b^- \rightarrow J/\psi\Omega^-) &= 0.183 \pm 0.068 \text{ nb}, \\ \sigma_{\Xi_b^-} \times B_r(\Xi_b^- \rightarrow J/\psi\Xi^-) &= 0.282 \pm 0.109 \text{ nb}.\end{aligned}$$

6.2.1 Systematic uncertainties

The systematic uncertainties in the production cross sections are estimated by evaluating the uncertainty in each term in Equation (6.3). An uncertainty in the luminosity measurement during the 2011 running has been estimated to be $\pm 1.8\%$ [42]. The uncertainties in the branching ratios are $\pm 1.01\%$, $\pm 1.03\%$, $\pm 0.035\%$, and $\pm 0.782\%$ for the J/ψ , Ω^- , Ξ^- , and Λ^0 decays, respectively [3], resulting in the uncertainties of $\pm 1.64\%$ for the Ω_b^- production cross section and $\pm 1.28\%$ for the Ξ_b^- production cross section. The uncertainty in ϵ is suspected to be large and difficult to estimate. The efficiency is evaluated with the MC samples without the pile-up, in which only one pp collision is simulated in each event. In the used data, the average number of collisions per a bunch crossing (μ) is 8.3. Therefore, in reality, there are 8.3 events overlapped in the data (which is called as ‘pile-up’). A small number of the MC samples were generated with the pile-up ($\bar{\mu} = 8.6$). Some results obtained from the two MC samples are shown in Table 6.7. The efficiency reduces when the pile-up is added. However, the significance of the reduction is only 2.7σ for the Ω_b^- sample and 2.2σ for the Ξ_b^- sample. With the limited statistics, it is not clear if the difference

Table 6.7: Parameters used for evaluating the production cross sections, estimating by using the MC samples with the pile-up.

Particle	Ω_b^-	Ξ_b^-
$N_{\text{MC}}^{\text{Sig}}$	46.10 ± 6.82	62.57 ± 7.99
N^{Gen}	19989	50533
ϵ	$(2.30 \pm 0.341) \times 10^{-3}$	$(1.24 \pm 0.158) \times 10^{-3}$

comes from the pile-up effect or the statistical fluctuation. To be conservative, the efficiency ϵ from the pile-up MC sample is used for the center value and the difference

between the two estimations is assigned as the systematic error; $\pm 28.6\%$ for the Ω_b^- production cross section and $\pm 23.3\%$ for the Ξ_b^- one. The uncertainty estimated for each parameter and the resultant total uncertainties are summarized in Table 6.8. The discussion about the pile-up effect is detailed in Appendix D.3.

Table 6.8: Summary table of the systematic uncertainties for the production cross sections.

Syst. uncertainty	$\Delta\sigma_{\Omega_b^-}$	$\Delta\sigma_{\Xi_b^-}$
Luminosity	$\pm 1.8\%$	$\pm 1.8\%$
Branching ratio	$\pm 1.64\%$	$\pm 1.28\%$
Pile-up	$\pm 28.6\%$	$\pm 23.4\%$
Total	$\pm 28.7\%$	$\pm 23.5\%$

6.2.2 Production cross section results

The estimated production cross sections in the fiducial volume are

$$\begin{aligned}\sigma_{\Omega_b^-}^{\text{F.V.}} \times B_r(\Omega_b^- \rightarrow J/\psi\Omega^-) &= 33.7 \pm 13.5(\text{stat.}) \pm 9.7(\text{syst.}) \text{ pb}, \\ \sigma_{\Xi_b^-}^{\text{F.V.}} \times B_r(\Xi_b^- \rightarrow J/\psi\Xi^-) &= 51.7 \pm 21.0(\text{stat.}) \pm 12.1(\text{syst.}) \text{ pb}.\end{aligned}$$

Here, the center values are obtained from the MC samples with the pile-up. These results can be extrapolated to the production cross sections under the bottom baryon conditions of $p_T > 6$ GeV and $|\eta| < 2.7$. They are, including the uncertainty of the efficiency,

$$\begin{aligned}\sigma_{\Omega_b^-} \times B_r(\Omega_b^- \rightarrow J/\psi\Omega^-) &= 0.256 \pm 0.103(\text{stat.}) \pm 0.074(\text{syst.}) \text{ nb}, \\ \sigma_{\Xi_b^-} \times B_r(\Xi_b^- \rightarrow J/\psi\Xi^-) &= 0.368 \pm 0.149(\text{stat.}) \pm 0.086(\text{syst.}) \text{ nb}.\end{aligned}$$

These are the first measurements in pp collisions at $\sqrt{s} = 7$ TeV.

6.3 Discussion and outlook

In this analysis, the integrated luminosity was not sufficient to measure the bottom baryons accurately and resulted in the significances of 3.6σ for the Ω_b baryon and 2.9σ for the Ξ_b^- baryon. However, this study has demonstrated that the two-stage

kinematical fit can suppress the background in pp collisions and one can provide for research in the field of bottom baryon spectroscopy at the LHC. The LHCb experiment, which has a lead in this field, has succeeded in identification of the bottom baryons in the pseudorapidity region of $2 < \eta < 5$, but the production cross section results of this analysis are the first measurements in the central region of pseudorapidity ($|\eta| < 2.4$), where a large area is covered by the ATLAS detector and it is possible, in the future, to perform studies in association to bottom baryons. This paves a pathway to the research field of the system with bottom baryons.

As one of the directional movements in bottom baryon spectroscopy, the search for heavier bottom baryons can be presented with a large amount of statistics since a lot of other bottom baryons including excited states are expected. The LHCb experiment has observed two new Ξ_b^- baryon resonances by combining the Ξ_b^0 baryon and the π^- track and calculating the mass difference of $\Delta M = m(\Xi_b^0\pi^-) - m(\Xi_b^0) - m(\pi^-)$ [15]. Figure 6.7 shows the example of excited states of the Ξ_b^- baryon observed by the LHCb experiment with the mass difference. The experiment also found excited states of the Λ_b^0 baryon with the mass distribution of the $\Lambda_b^0\pi^+\pi^-$ system [43]. At the ATLAS experiment, the production cross sections of these particles in the central region can be measured by the use of these methods.

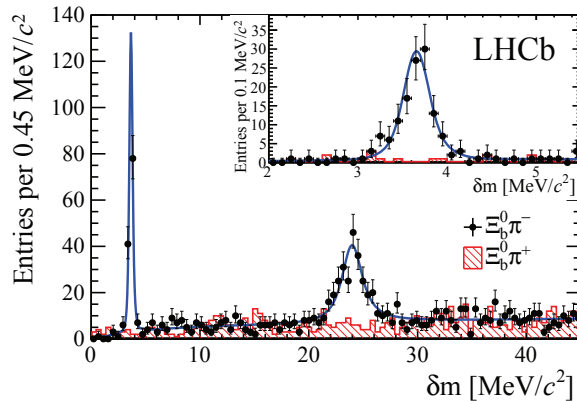


Figure 6.7: Distribution of the mass difference for the Ξ_b^{*-} baryon [15].

The highly excited state of the Ω_b^- baryon, which has not been observed yet at all, is considered as another example. The excited state with a heavier mass can be searched for like the case of the excited Λ_b^0 states. However, as shown in the following paragraph, the first excited state Ω_b^{*-} likely has the mass close to the Ω_b^- baryon and is not easy to observe.

The color-hyperfine (HF) interaction theory is often used for expectation of the masses [44]. Baryons are described as valence quarks in a sea of gluons and $q\bar{q}$

pairs, and the masses are estimated by summation of the quark masses and their correlations;

$$M = \sum_i m_i + \sum_{i<j} V_{ij}^{HF}, \quad (6.5)$$

where $\sum_{i<j} V_{ij}^{HF} \equiv v_0 (\vec{\lambda}_i \cdot \vec{\lambda}_j) \frac{\vec{\sigma}_i \cdot \vec{\sigma}_j}{m_i m_j} \langle \psi | \delta(r_i - r_j) | \psi \rangle$ is the correlation part from HF, $\vec{\lambda}$ is the SU(3) color matrix, $\vec{\sigma}$ is the quark spin operator, and $|\psi\rangle$ is the baryon wave function. This equation provides a good prediction for mass splitting and magnetic moments. For example, HF splitting of the Σ baryon is described as [45]

$$M(\Sigma^*) - M(\Sigma) = 6v_0 \frac{\vec{\lambda}_u \cdot \vec{\lambda}_s}{m_u m_s} \langle \psi | \delta(r_{us}) | \psi \rangle. \quad (6.6)$$

This frame work can be extended to the bottom baryons with the estimation of the correlation part from the meson mass splitting [45]:

$$M(\Sigma_b^*) - M(\Sigma_b) = \frac{M(B^*) - M(B)}{M(K^*) - M(K)} [M(\Sigma^*) - M(\Sigma)] = 22 \text{ MeV}. \quad (6.7)$$

This splitting was measured by the CDF experiment [7] and the result (~ 20 MeV) is consistent with this model. This method can be also applied to estimate the mass of the Ω_b^{*-} baryon. The relation equation between the Ω_b^- and Ω_b^{*-} baryons is [45]

$$M(\Omega_b^{*-}) - M(\Omega_b^-) = (M(\Omega_c^{*-}) - M(\Omega_c^-)) \frac{m_c \langle \delta(r_{bs}) \rangle_{\Omega_b^-}}{m_b \langle \delta(r_{cs}) \rangle_{\Omega_c^-}} = 30.7 \pm 1.3 \text{ MeV}. \quad (6.8)$$

The mass difference is too small to decay with hadrons. In the search for the Ω_b^{*-} baryon, the decay mode $\Omega_b^{*-} \rightarrow \Omega_b^- \gamma$ is the main target. The detection of the soft photon is not easy. Considering the measured mass of the Ω_b^- baryon in this study, energy of γ is 30.6 MeV at the Ω_b^{*-} rest frame. However, the wide coverage of the ATLAS liquid argon calorimeter in the central pseudorapidity area will help for the photon identification. In the case that γ energy resolution is essential, measurements with the converted photons will be helpful.

Baryons with two bottom quarks bbq are expected from bottom baryon spectroscopy (see Figure 2.6 and 2.7). The single bottom baryon bqq can decay via the hadronic mode $b \rightarrow c\bar{c}(J/\psi) s$. Therefore, if both of two bottom quarks of the double bottom baryon can also decay like this way, events which have two J/ψ can be considered as the target. The example of the Ω_{bb}^- and Ξ_{bb}^- decay kinematics is shown in Figure 6.8, where the double bottom baryons decay via $\Omega_{bb}^- \rightarrow \Omega_b^- (\rightarrow \Omega^- J/\psi) J/\psi$ or $\Xi_{bb}^- \rightarrow \Xi_b^- (\rightarrow \Xi^- J/\psi) J/\psi$. This unique signature is produced at a very low rate and reducing the background is more important. In this study, the two-stage kinematical fit is used and the single bottom baryons can be reconstructed with the high purity in

pp collisions. At some future point, where a lot of integrated luminosity is recorded at the LHC, this vertex fit would be effective for the search for double bottom baryons, too.

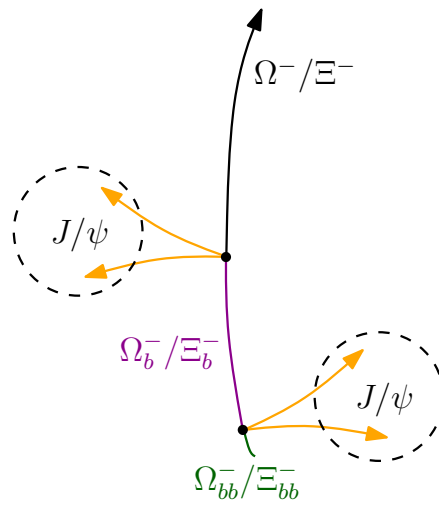


Figure 6.8: Image of a double bottom baryon decay chain.

Chapter 7

Conclusions

Studies of the bottom baryons Ω_b^- and Ξ_b^- produced in pp collisions were performed at $\sqrt{s} = 7$ TeV with the ATLAS detector at the LHC. The bottom baryons were reconstructed in the decay modes of $\Omega_b^- \rightarrow J/\psi(\rightarrow \mu^+\mu^-) + \Omega^-(\rightarrow \Lambda^0(\rightarrow p\pi^-)K^-)$, $\Xi_b^- \rightarrow J/\psi(\rightarrow \mu^+\mu^-) + \Xi^-(\rightarrow \Lambda^0(\rightarrow p\pi^-)\pi^-)$, and their charge conjugates. These studies were performed using data collected in the year 2011 corresponding to the integrated luminosity of 4.5 fb^{-1} . The events were collected with an online trigger in which the detection of an opposite charge muon pair was required to have an invariant mass within the range of $2.5 < m_{\mu\mu} < 4.3$ GeV and each muon to have $p_T > 4$ GeV.

The masses of the Ω_b^- and Ξ_b^- candidates were reconstructed from momenta of the five charged tracks after applying constraint fits on the vertex points and the masses of the decayed particles. The background was strongly suppressed by requiring a constraint to have sufficiently separated decay vertices between the J/ψ , Ω^- (Ξ^-), and Λ^0 candidates.

In the Ω_b^- study, 23 candidates selected in the mass range of $5700 < M(\Omega^- J/\psi) < 6600$ MeV showed a concentration around 6050 MeV. The unbinned maximum likelihood fit was performed with the signal shape determined by the MC sample and with the constant background. 8.6 events were found at the mass position of 6035.8 ± 10.6 MeV with the significance of 3.6σ .

In the Ξ_b^- study, 45 candidates remained in the mass range of $5500 < M(\Xi^- J/\psi) < 6400$ MeV. The Ξ_b^- mass was determined to be 5775.9 ± 12.8 MeV with 10.4 events. The significance was 2.9σ .

Considering that the events were the signals, the masses and the production cross sections were estimated with the systematic uncertainties. Taking possible biases from the selection procedure, the masses of the Ω_b^- and Ξ_b^- baryons were determined

to be

$$\begin{aligned}
M_{\Omega_b^-} &= 6035.8 \pm 10.6(\text{stat.})_{-1.1}^{+6.7}(\text{syst.}) \text{ MeV}, \\
M_{\Xi_b^-} &= 5775.9 \pm 12.8(\text{stat.})_{-0.8}^{+5.9}(\text{syst.}) \text{ MeV}.
\end{aligned}$$

These results are consistent with the values reported by the CDF and LHCb experiments.

The production cross section including the branching ratio of $\Omega_b^- \rightarrow J/\psi\Omega^-$ ($\Xi_b^- \rightarrow J/\psi\Xi^-$) was evaluated using the prediction of PYTHIA. The production cross sections in the fiducial volume, $p_T > 6$ GeV and $|\eta| < 2.7$ for the bottom baryons, and $p_T > 3.5$ GeV and $|\eta| < 2.5$ for at least one of the two muons from the J/ψ decay, were measured to be

$$\begin{aligned}
\sigma_{\Omega_b^-}^{\text{F.V.}} \times B_r(\Omega_b^- \rightarrow J/\psi\Omega^-) &= 33.7 \pm 13.5(\text{stat.}) \pm 9.7(\text{syst.}) \text{ pb}, \\
\sigma_{\Xi_b^-}^{\text{F.V.}} \times B_r(\Xi_b^- \rightarrow J/\psi\Xi^-) &= 51.7 \pm 21.0(\text{stat.}) \pm 12.1(\text{syst.}) \text{ pb}.
\end{aligned}$$

These results can be extrapolated to the production cross sections under the conditions of the bottom baryons, $p_T > 6$ GeV and $|\eta| < 2.7$. The obtained values were

$$\begin{aligned}
\sigma_{\Omega_b^-} \times B_r(\Omega_b^- \rightarrow J/\psi\Omega^-) &= 0.256 \pm 0.103(\text{stat.}) \pm 0.074(\text{syst.}) \text{ nb}, \\
\sigma_{\Xi_b^-} \times B_r(\Xi_b^- \rightarrow J/\psi\Xi^-) &= 0.368 \pm 0.149(\text{stat.}) \pm 0.086(\text{syst.}) \text{ nb}.
\end{aligned}$$

This analysis represents that bottom baryons can be reconstructed with the high purity at the LHC by the two-stage kinematical fit. This paves a pathway to the field of bottom baryon spectroscopy as a lot of excitation levels of bottom baryons and double bottom baryons are expected and most of them are undiscovered.

Appendix A

Distributions of the data and the MC samples

A.1 MC truth distributions

Figure A.1 shows the p_T and η distributions of the MC samples at the generated level. The red lines show the distributions before the muon cuts and the blue lines show those with $p_T > 3.5$ GeV of the muon. The black lines show the efficiencies under the condition.

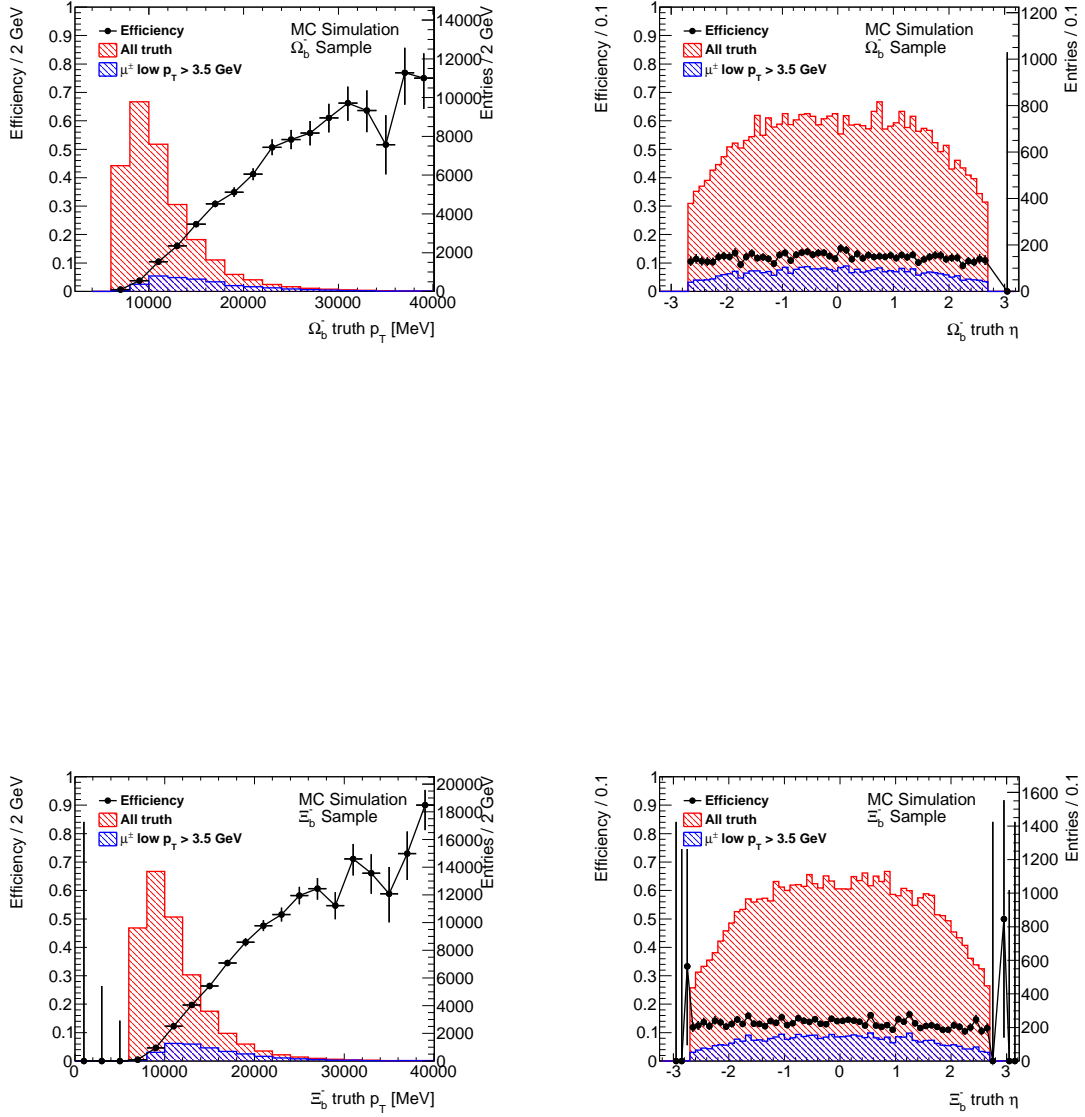


Figure A.1: Generated p_T (left) and η (right) distributions of the Ω_b^- (top) and Ξ_b^- (bottom) samples.

A.2 Baryon reconstruction

Figure A.2 shows the invariant mass distributions of the Λ^0 candidates satisfying the quality requirements. These plots are those for the MC samples corresponding to Figure 5.12. Figure A.3 also shows the L_{xy} distributions for the MC samples corresponding to Figure 5.14.

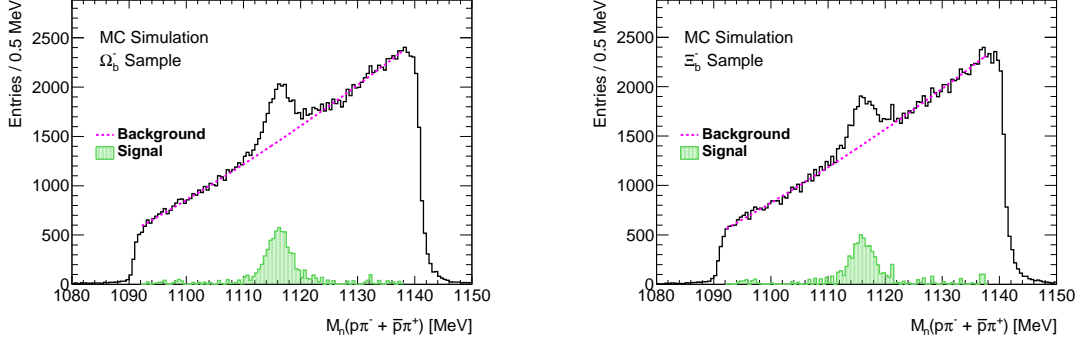


Figure A.2: Invariant mass distributions of the Λ^0 candidates satisfying the quality requirements in the MC samples.

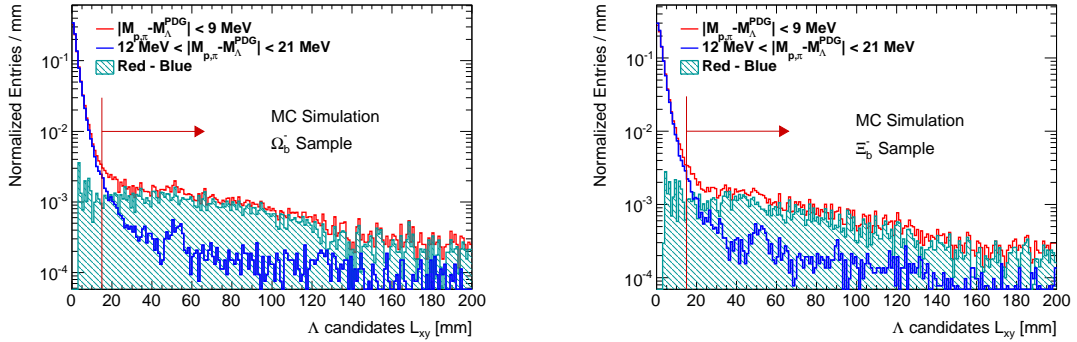


Figure A.3: L_{xy} distributions of the Λ^0 candidates in the MC samples.

Figure A.4 shows the invariant mass distributions of the Ω^- and Ξ^- candidates satisfying the quality requirements. The left and right plots are those for the MC samples corresponding to Figure 5.28 and 5.21, respectively. Figure A.5 shows the L_{xy} distributions corresponding to Figures 5.29 and 5.23. Figure A.6 shows the $\cos\theta$ distributions corresponding to Figures 5.30 and 5.24.

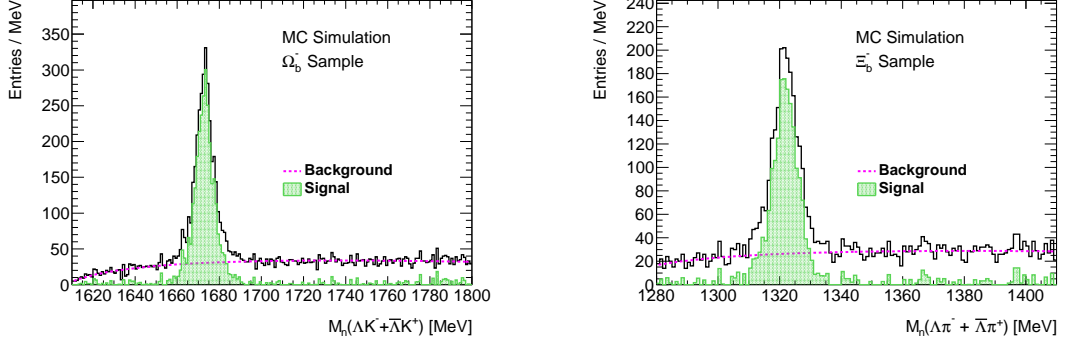


Figure A.4: Invariant mass distributions of the Ω^- (left) and Ξ^- (right) candidates satisfying the quality requirements in the MC samples.

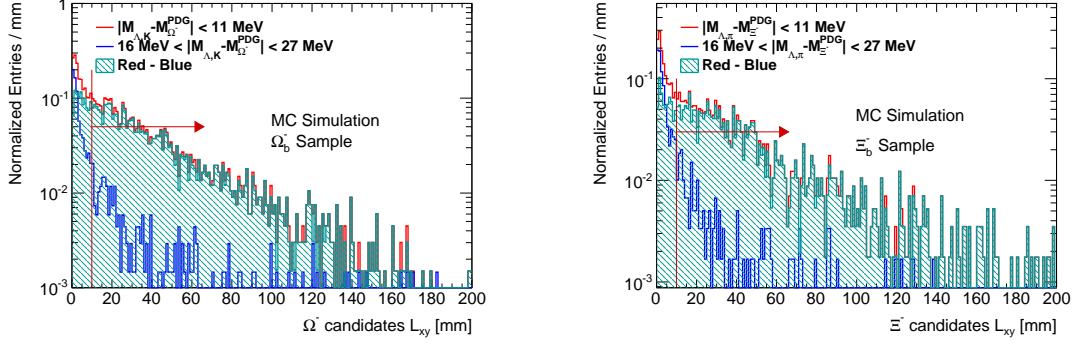


Figure A.5: L_{xy} distributions of the Ω^- (left) and Ξ^- (right) candidates in the MC samples.

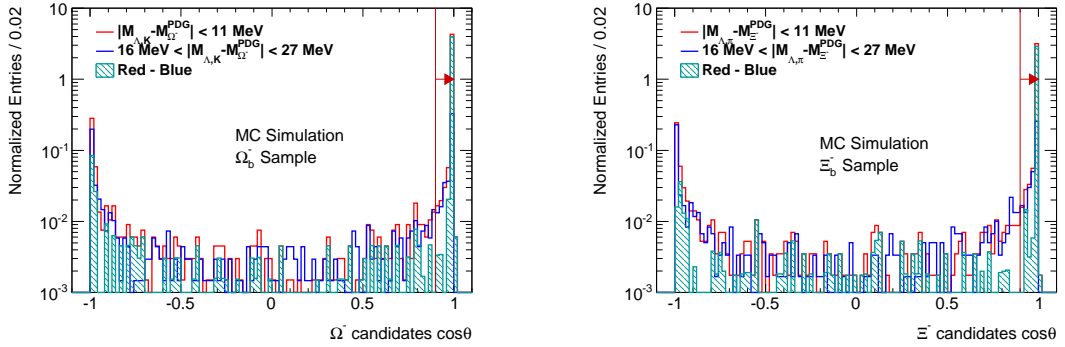


Figure A.6: $\cos \theta$ distributions of the Ω^- (left) and Ξ^- (right) candidates in the MC samples.

A.3 Ω^- and Ξ^- reconstruction efficiencies

Figure A.7 shows dR distributions between the truth Ω^- (left)/ Ξ^- (right) and the reconstructed Ω^- / Ξ^- candidates in the signal region in the MC sample. When $dR < 0.05$ is also required as a condition of matching between the truth and the reconstruction events in addition to the signal mass window requirement, the efficiencies in p_T , η , and ϕ of the truth Ω^- / Ξ^- are shown in Figure A.9. Here, the efficiencies represent those with respect to the matched Λ^0 events. Figure A.8 shows the efficiencies in L_x with respect to the truth J/ψ vertex.

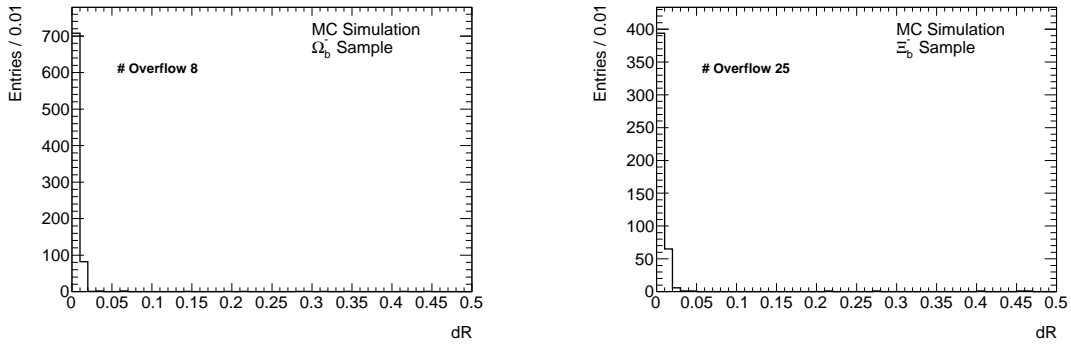


Figure A.7: dR distributions between the truth Ω^- (left) and Ξ^- (right) and the reconstructed Ω^- and Ξ^- candidates, respectively

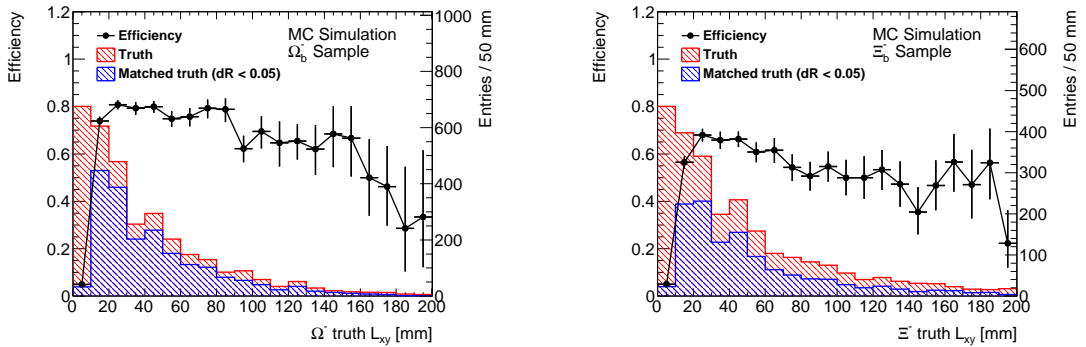


Figure A.8: Reconstruction efficiencies in L_{xy} of the Ω^- (left) and Ξ^- (right) candidates.

A.3 Ω^- and Ξ^- reconstruction efficiencies

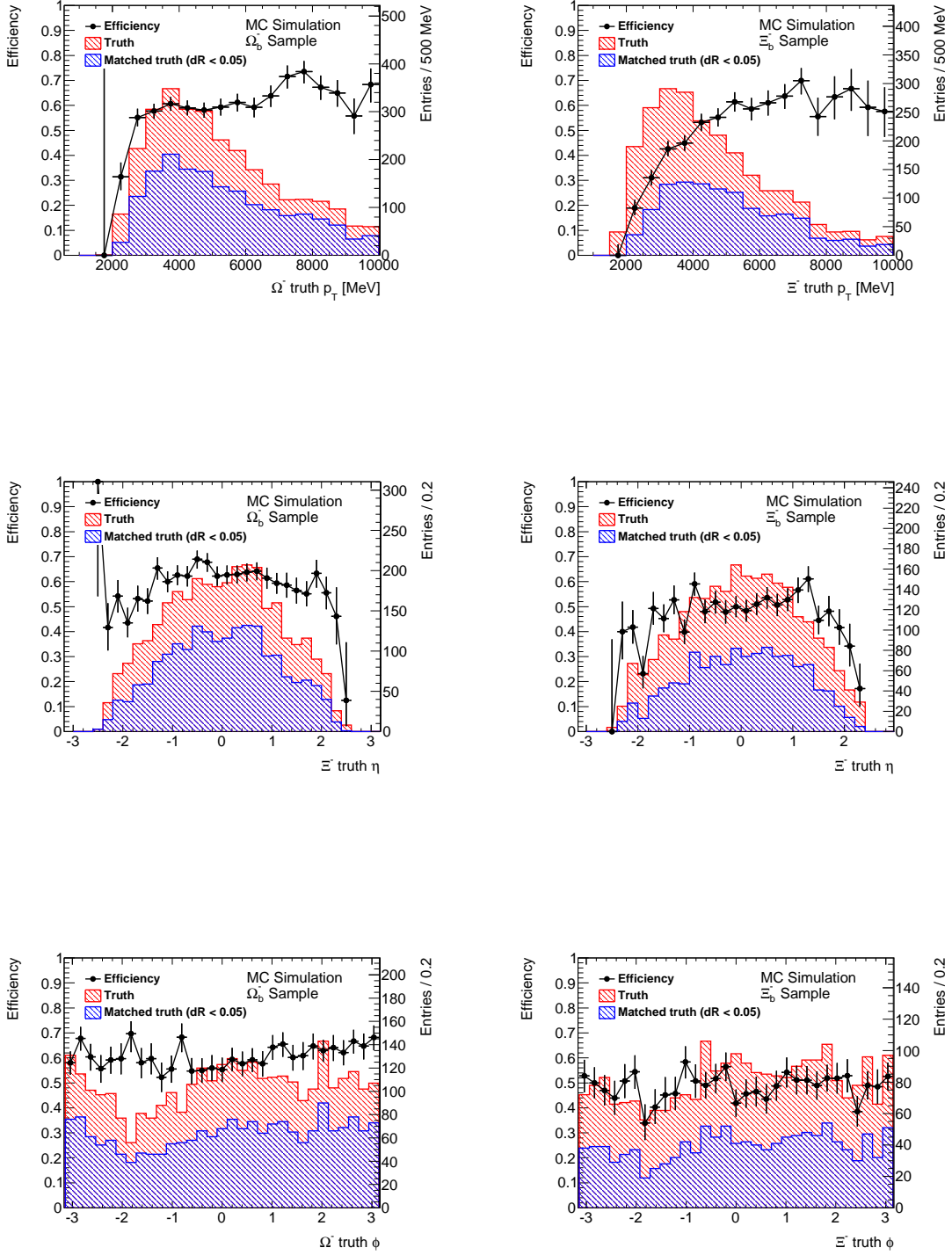


Figure A.9: Ω^- and Ξ^- reconstruction efficiencies.

A.4 Distributions of the Ω_b^- candidates

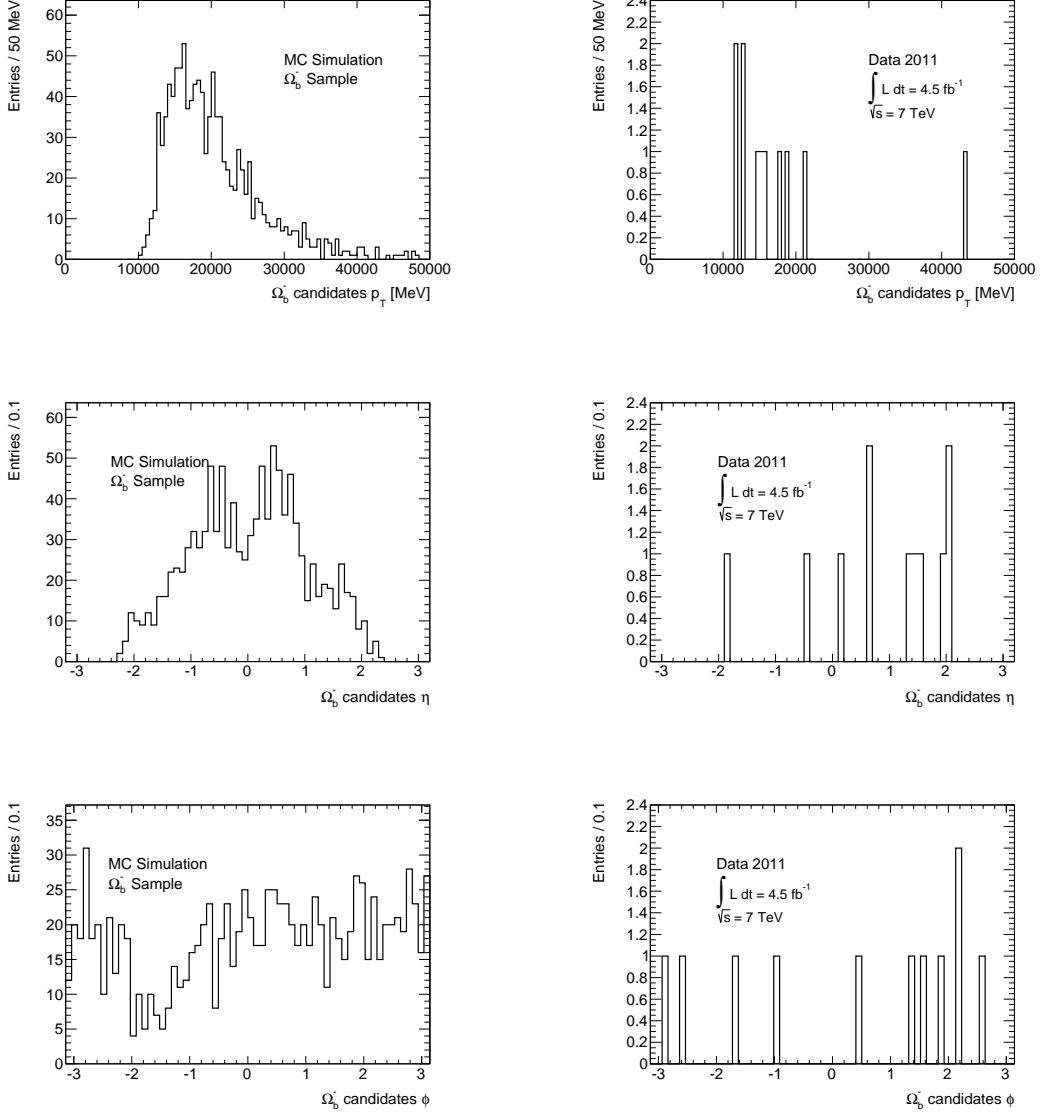


Figure A.10: p_T , η , and ϕ distributions of the Ω_b^- candidates in the data (right) and the MC sample (left).

Figure A.10 shows the p_T , η , and ϕ distributions of the Ω_b^- candidates. The draw range is set between $m_{\text{data}}^G - 2\sigma$ and $m_{\text{data}}^G + 2\sigma$ detailed in Subsection 6.1.2.

A.5 Distributions after the refit for the Ξ_b^- analysis

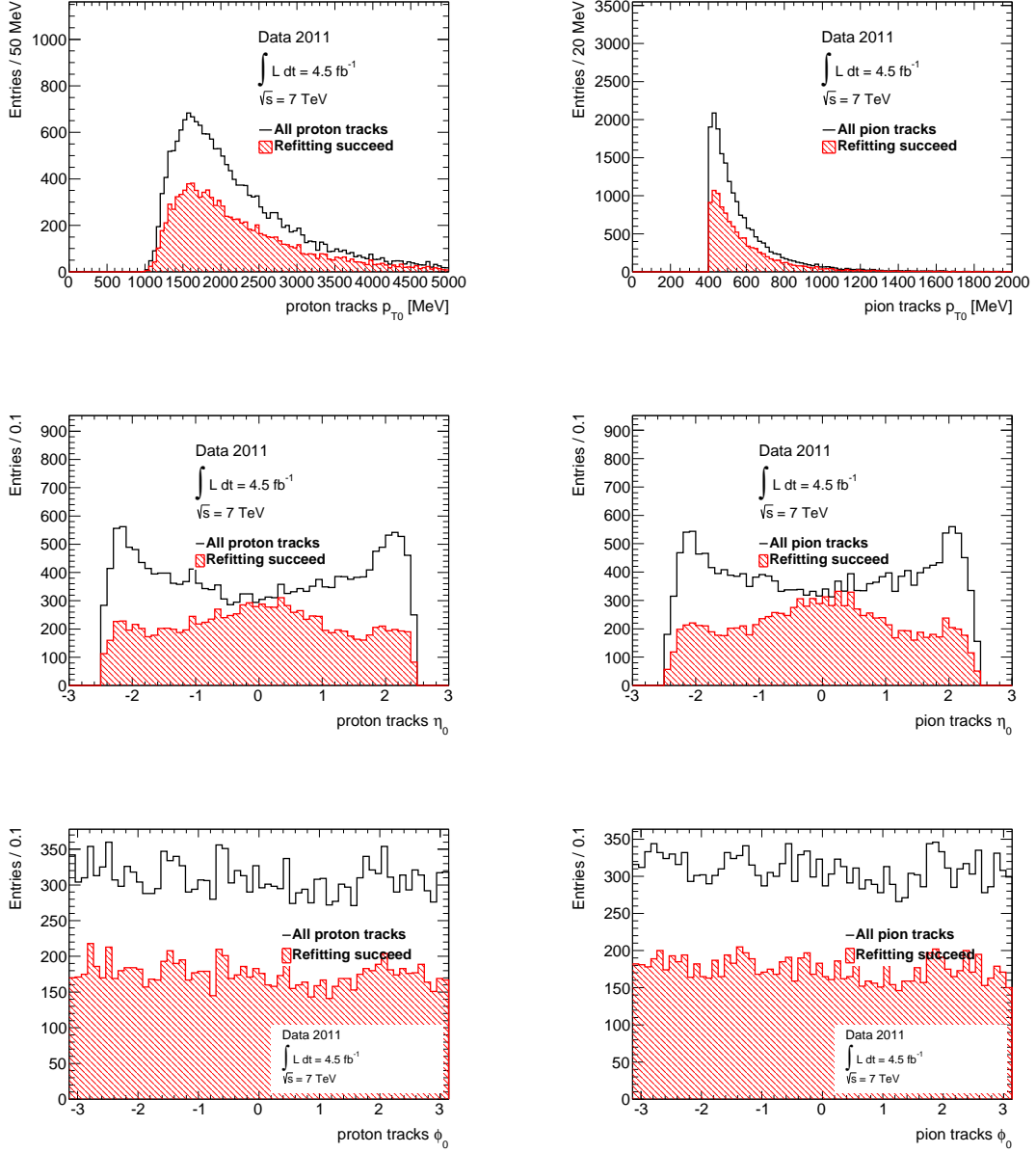


Figure A.11: p_{T0} , η_0 , and ϕ_0 distributions after the refit for the Ξ_b^- candidates (data).

A.5 Distributions after the refit for the Ξ_b^- analysis

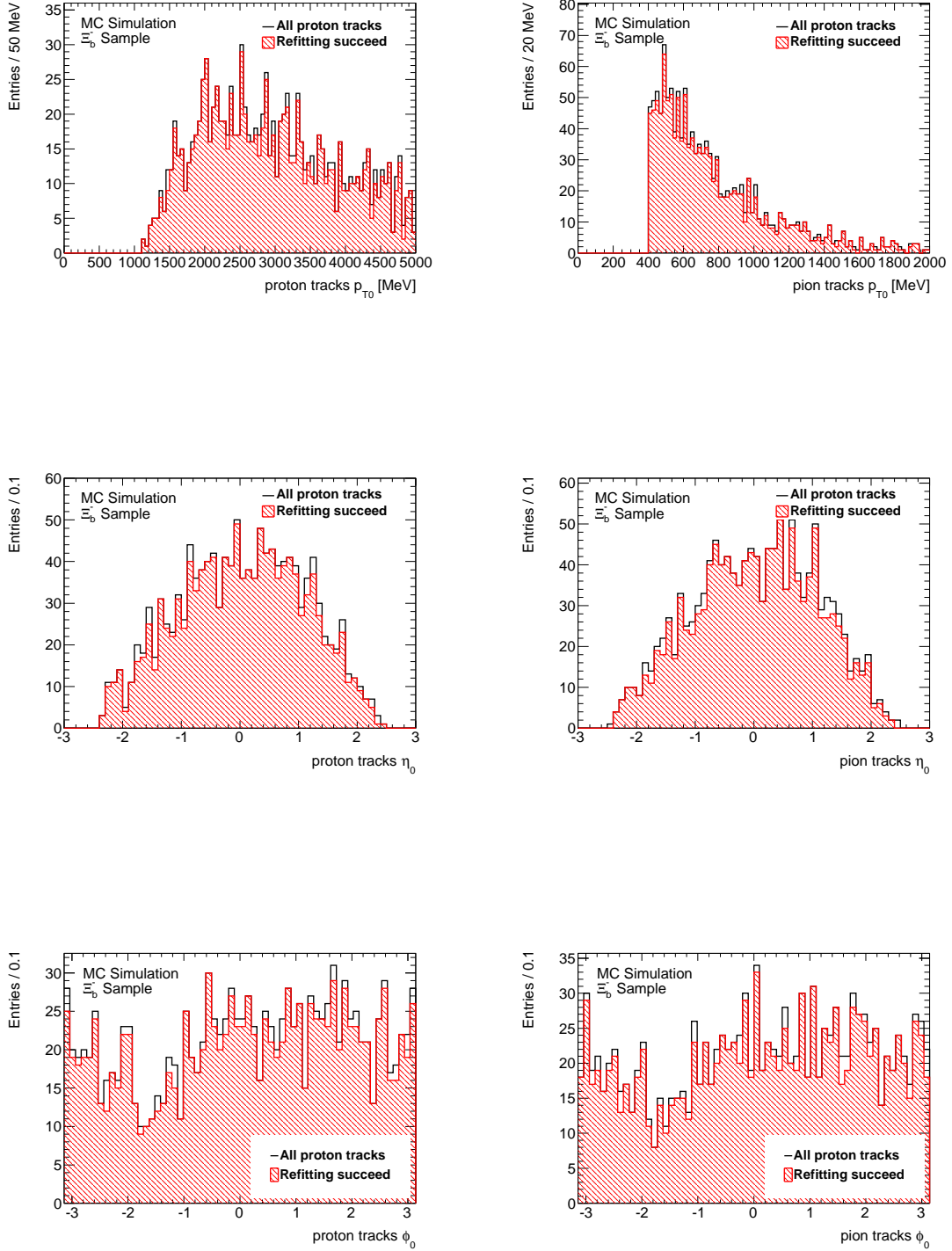


Figure A.12: p_{T0} , η_0 , and ϕ_0 distributions after the refit for the Ξ_b^- candidates (MC).

A.5 Distributions after the refit for the Ξ_b^- analysis

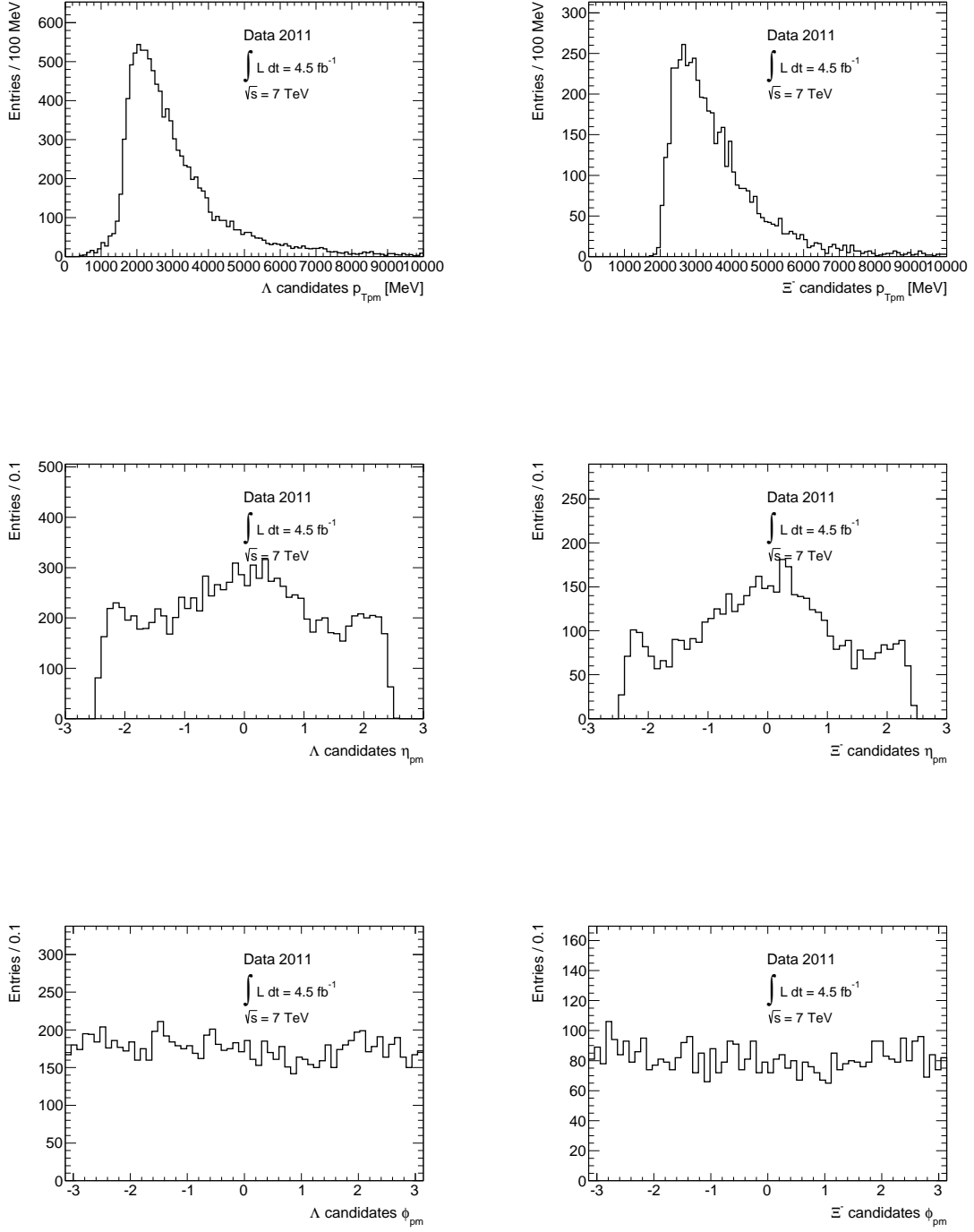


Figure A.13: p_{Tpm} , η_{pm} , and ϕ_{pm} distributions of the Λ^0 and Ξ^- candidates after the refit.

A.6 Distributions of the Ξ_b^- candidates

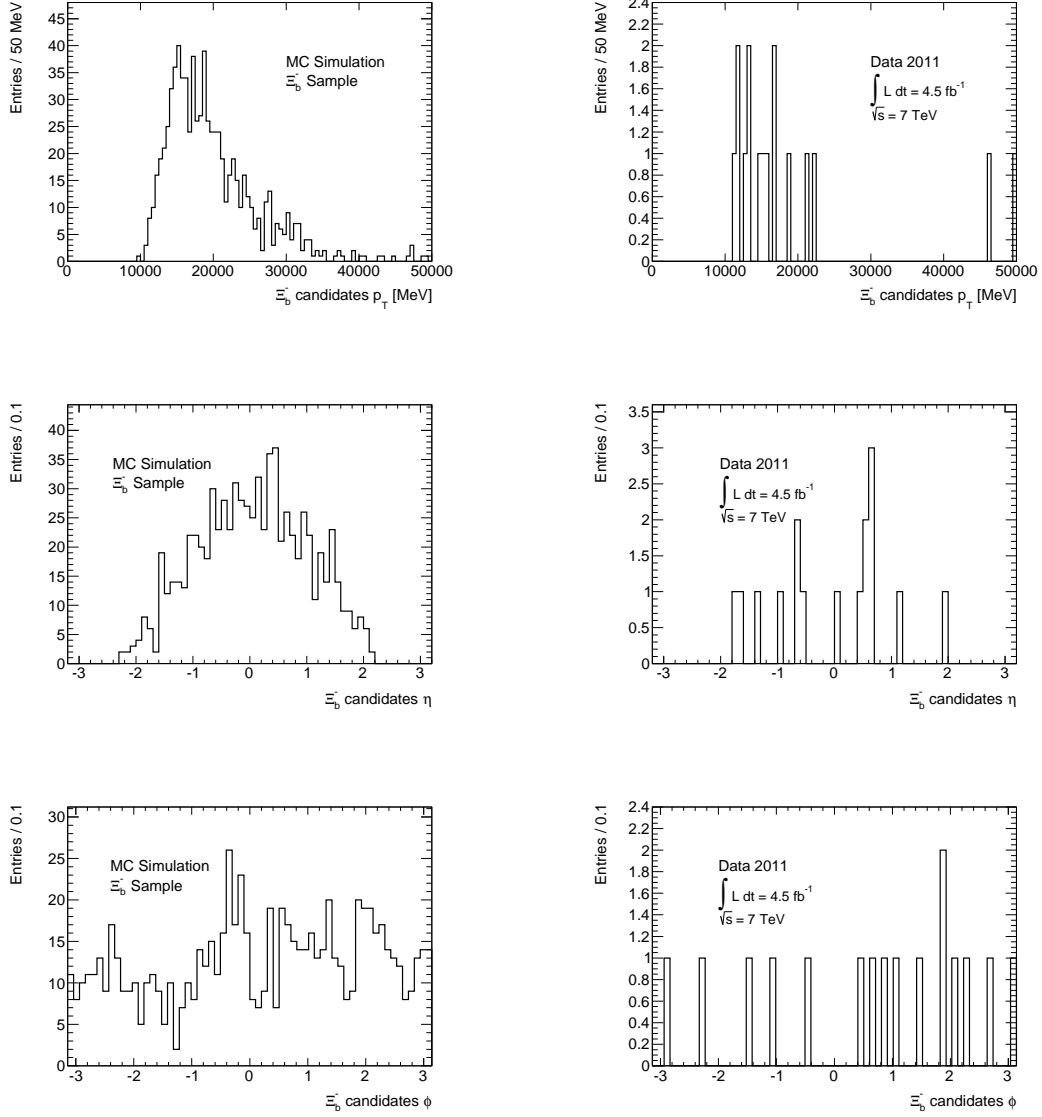


Figure A.14: p_T , η , and ϕ distributions of the Ξ_b^- candidates in the data (right) and the MC sample (left).

Figure A.14 shows the p_T , η , and ϕ distributions of the Ξ_b^- candidates. The draw range is set between $m_{\text{data}}^G - 2\sigma$ and $m_{\text{data}}^G + 2\sigma$ detailed in Subsection 6.1.2.

Appendix B

Unbinned maximum likelihood fit

A function for the likelihood fit is generally defined as $L(\boldsymbol{\theta}) = P(\mathbf{x}|\boldsymbol{\theta})$. Here, $P(\mathbf{x}|\boldsymbol{\theta})$ represent a conditional probability of data \mathbf{x} under a hypothesis $\boldsymbol{\theta} = (\theta_1, \theta_2, \dots, \theta_N)$, and \mathbf{x} is a function of $\boldsymbol{\theta}$. To evaluate the values that give the maximum of $L(\boldsymbol{\theta})$, partial differentiation is executed to the logarithm:

$$\frac{\partial \ln L}{\partial \theta_i} = 0, \quad i = 1, 2, \dots, N. \quad (\text{B.1})$$

When the data $\mathbf{x} = (x_1, x_2, \dots, x_n)$ are independent and identically distributed (*i.i.d*) values and have the same *p.d.f.* $f(x; \boldsymbol{\theta})$, the likelihood function is written as

$$L(\boldsymbol{\theta}) = \prod_{i=1}^n f(x_i; \boldsymbol{\theta}), \quad (\text{B.2})$$

where n is the number of events and depends on $\boldsymbol{\theta}$, i.e., $f(x_i; \boldsymbol{\theta})$ includes a function about n . In general, it is assumed that n follows the Poisson distribution with the mean μ . Therefore, Equation (B.2) is able to be rewritten as [3]

$$L(\boldsymbol{\theta}) = \frac{\mu^n}{n!} e^{-\mu} \prod_{i=1}^n P(x_i; \boldsymbol{\theta}). \quad (\text{B.3})$$

Here, $P(x_i; \boldsymbol{\theta})$ means the new *p.d.f.* about the data \mathbf{x} . An interpretation of the *p.d.f.* is that $P(x_i; \boldsymbol{\theta})$ describes a shape of the expected distribution in \mathbf{x} [36]. In this analysis, Equation (B.3) is used as the likelihood function.

Appendix C

Single Gaussian fit

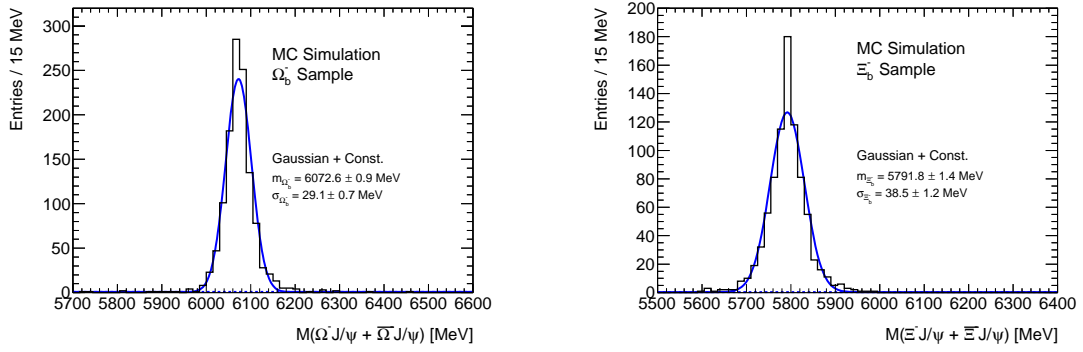


Figure C.1: Invariant mass distributions of the Ω_b^- (left) and Ξ_b^- (right) candidates with the single Gaussian fit in the MC samples.

Appendix D

Significance and systematic uncertainties

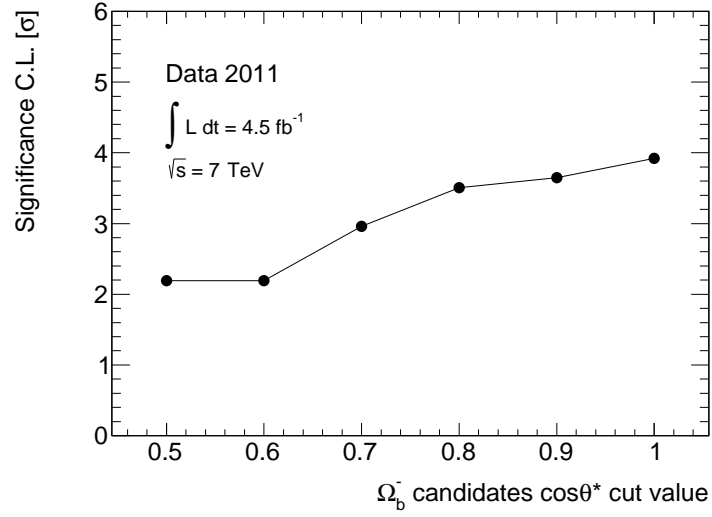
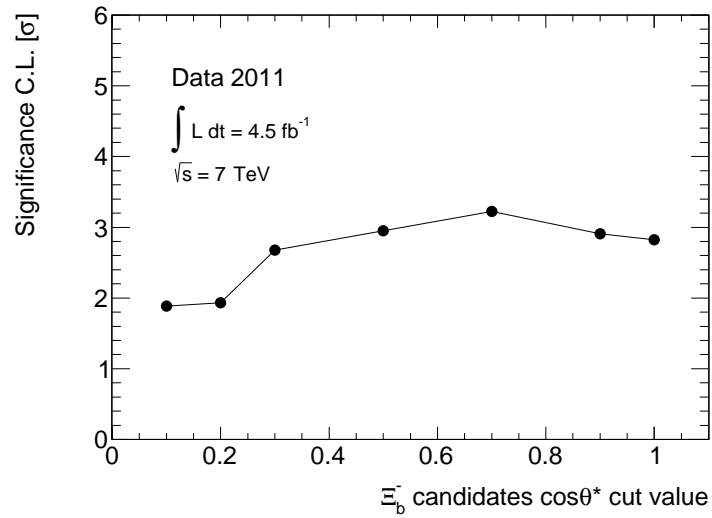
D.1 Significance

The statistical significance depends on the $\cos\theta^*$ requirement. Figures D.1 and D.2 show distributions of the statistical significance in $\cos\theta^*$. The Ω_b^- significance reaches a peak when the $\cos\theta^*$ requirement is $\cos\theta^* \lesssim 1$, and the Ξ_b^- significance reaches a peak around $\cos\theta^* \lesssim 0.7$. In this analysis, $\cos\theta^* < 0.9$ is required for both of the Ω_b^- and Ξ_b^- candidates. The significances are summarized in Table D.1.

Table D.1: Summary table of the statistical significance.

Ω_b^-	$\cos\theta^* < x$	σ
-	$x = 1$	3.9
-	0.9	3.6
-	0.8	3.5
-	0.7	3.0
-	0.6	2.2
-	0.5	2.2

Ξ_b^-	$\cos\theta^* < x$	σ
-	$x = 1$	2.8
-	0.9	2.9
-	0.7	3.2
-	0.5	3.0
-	0.3	2.7
-	0.2	1.9
-	0.1	1.9

Figure D.1: Ω_b^- significance in $\cos\theta^*$.Figure D.2: Ξ_b^- significance in $\cos\theta^*$.

D.2 Systematic uncertainties of the tracking momentum scale

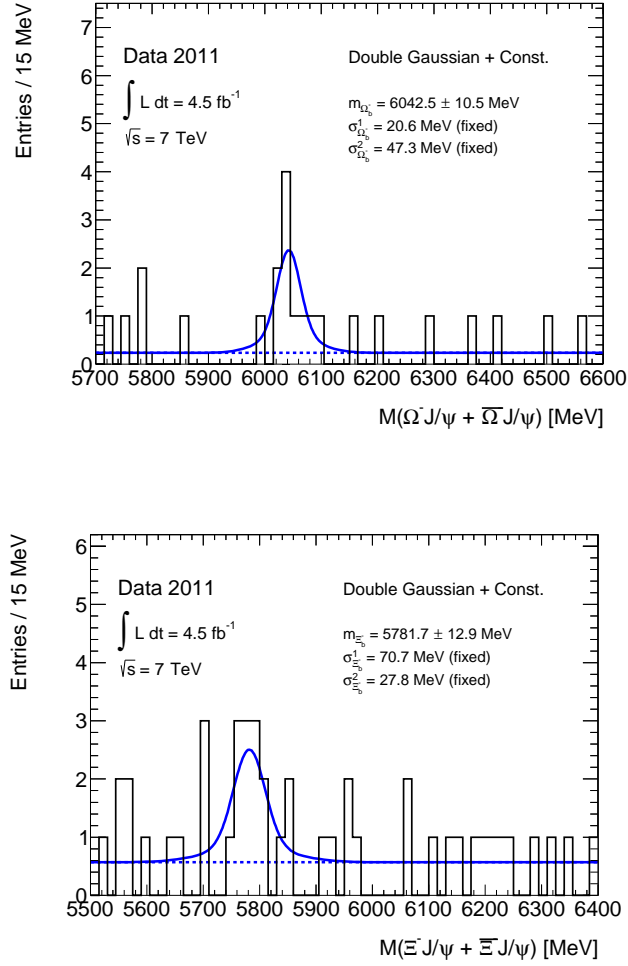


Figure D.3: Invariant mass distributions of the Ω_b^- (top) and Ξ_b^- (bottom) candidates with the shifted tracks.

D.3 Systematic uncertainties of the pile-up effect

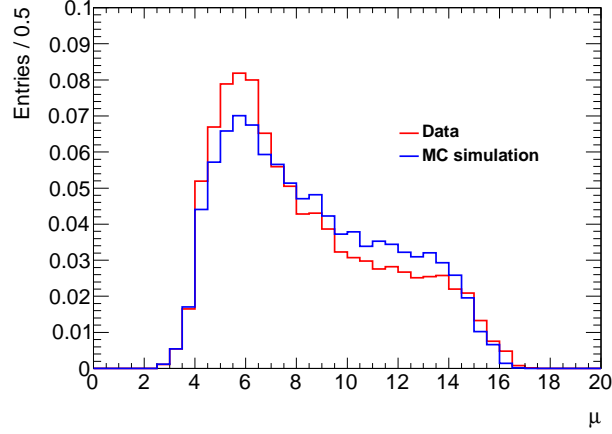


Figure D.4: μ distributions of the data and the MC sample.

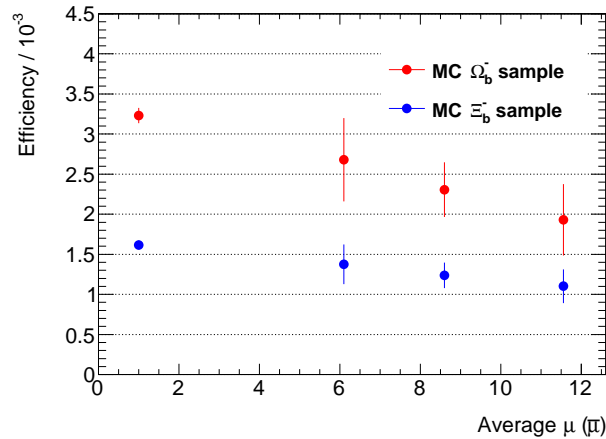


Figure D.5: Efficiencies in the average μ values.

Figure D.4 shows the μ distributions of the data (red) and the MC sample (blue). Figure D.5 shows the dependence of the efficiency with the average μ values. In Figure D.5, the second point from the right is used for the estimation of the center value of the production cross section. The three points from the right is evaluated by the same pile-up MC sample, i.e., the pile-up MC sample is separated into upper and lower parts of μ ; $\mu > 8.6$ or $\mu < 8.6$. Although the efficiency has a tendency to decrease as the average μ values increase, it is not clear if the difference comes from the pile-up effect or the statistical fluctuation.

Bibliography

- [1] E. Jenkins, “Heavy Baryon Masses in the $1/m_Q$ and $1/N_c$ Expansions”, *Phs. Rev. D* 54, 4515, 1996
- [2] D. Ebert, R. N. Faustov, and V. O. Galkin, “Masses of heavy baryons in the relativistic quark model”, *Phs. Rev. D* 72, 034026, 2005
- [3] Particle Data Group, “Review Of Particle Physics”, *Phys. Rev. D* 86, 010001, 2012
- [4] LHCb Collaboration, “Measurement of the Λ_b^0 , Ξ_b^- , and Ω_b^- Baryon Masses”, *PRL*, 110, 182001, 2013
- [5] CMS Collaboration, “Measurement of the Λ_b cross section and the $\bar{\Lambda}_b$ to Λ_b ratio with $J/\psi\Lambda$ decays in pp collisions at $\sqrt{s} = 7$ TeV”, arXiv:1205.0594v2, 2013
- [6] UA1 Collaboration, “First observation of the beauty baryon Λ_b in the decay channel $\Lambda_b \rightarrow J/\psi\Lambda$ at the CERN proton-antiproton collider”, *Phys. Lett. B* 273, 540-548, 1991
- [7] CDF collaboration, “Observation of the Heavy Baryons Σ_b and Σ_b^* ”, *PRL*, 99, 202001, 2007
- [8] D0 Collaboration, “Direct observation of the strange b baryon Ξ_b^- ”, *PRL*, 99, 052001, 2007
- [9] The Tevatron
<http://www.fnal.gov/pub/tevatron/tevatron-accelerator.html>
- [10] D0 Collaboration, “Observation of the doubly strange b baryon Ω_b^- with the D0 detector”, *PRL*, 101, 232002, 2008
- [11] CDF collaboration, “Observation of the Ξ_b^0 Baryon”, *PRL*, 107, 102001, 2011
- [12] CDF collaboration, “Observation of the Ω_b^- baryon and measurement of the properties of the Ξ_b^- and Ω_b^- baryons”, *Phs. Rev. D* 80, 072003, 2009

- [13] Particle Data Group, “Review Of Particle Physics”, Chinese Phys. C, 38, 090001, 2014
- [14] CMS Collaboration, “Observation of a new Ξ_b baryon”, arXiv:1204.5955v2, 2012
- [15] LHCb Collaboration, “Observation of two new Ξ_b^- baryon resonances”, arXiv:1411.4849v2, 2015
- [16] ATLAS Collaboration, “Observation of a new particle in the search for the Standard Model Higgs boson with the ATLAS detector at the LHC”, Phys. Lett. B716, 1-29, 2012
- [17] CMS Collaboration, “Observation of a new boson at a mass of 125 GeV with the CMS experiment at the LHC”, Phys. Lett. B716, 30-61, 2012
- [18] G. Aad et al. (ATLAS Collaboration, CMS Collaboration), “Combined Measurement of the Higgs Boson Mass in pp Collisions at $\sqrt{s} = 7$ and 8 TeV with the ATLAS and CMS Experiments” Phys. Rev. Lett. 114, 191803, 2015
- [19] The Large Hadron Collider
<http://home.web.cern.ch/topics/large-hadron-collider>
- [20] CERN Document Server
<http://cds.cern.ch/record/1621894/>
- [21] ATLAS Collaboration, “Improved luminosity determination in pp collisions at $\sqrt{s} = 7$ TeV using the ATLAS detector at the LHC”, arXiv:1302.4393v2, 2013
- [22] The four main LHC experiments, CERN-AC-9906026, 1999
<http://home.web.cern.ch/>
- [23] ATLAS Collaboration, “The ATLAS Experiment at the CERN Large Hadron Collider”, Jinst, 2008
- [24] ATLAS Muon Collaboration, “ATLAS Muon Spectrometer Technical Design Report”, CERN/LHCC 97-22, 1997
- [25] ATLAS Collaboration, “ATLAS DETECTOR AND PHYSICS PERFORMANCE Technical Design Report”, CERN/LHCC 99-14, 1999
- [26] T. Lenz, “Vertex Fitting in the ATLAS Inner Detector”, WU D 06-06, 2006
- [27] P. Billoir, S. Qian, “Fast vertex fitting with a local parametrization of tracks”, NIM, A311, p139-150, 1992

- [28] V. Kostyukhin, “VKalVrt - package for vertex reconstruction in ATLAS”, ATLPHYS-2003-031, 2003
- [29] T. Sjöstrand, S. Mrenna, P. Skands, “PYTHIA 6.4 Physics and Manual”, JHEP, 05, 026, 2006
- [30] ATLAS Collaboration, “The ATLAS Simulation Infrastructure”, Eur. Phys. J., C70, 823, 2010
- [31] S. Agostinelli *et. al.*, “GEANT4: A simulation toolkit”, NIM, A506, 250, 2003
- [32] ATLAS Collaboration, “Measurement of the Λ_b^0 lifetime and mass in the ATLAS experiment”, Phys. Rev. D87, 032002, 2013
- [33] ATLAS EXPERIMENT - Public Results
<https://twiki.cern.ch/twiki/bin/view/AtlasPublic/MuonTriggerPublicResults>
- [34] ATLAS EXPERIMENT - Public Results
<https://twiki.cern.ch/twiki/bin/view/AtlasPublic/LuminosityPublicResults>
- [35] “ATLAS Muon Combined Performance Guidelines for Analyses of 2011 Data in Release 17”
<https://twiki.cern.ch/twiki/bin/view/AtlasProtected/MCPAnalysisGuidelinesRel17MC11a> (protected)
- [36] R. Barlow, “Extended maximum likelihood”, NIM, A297, p496-506, 1990
- [37] W. Verkerke, D. Kirkby, “RooFit Users Manual v2.91”, 2008
- [38] W. Verkerke, D. Kirkby, “The RooFit toolkit for data modeling”, <http://roofit.sourceforge.net>, CHEP, 2003
- [39] C. Kyle, L. George, M. Lorenzo, S. Akira, V. Wouter, “HistFactory: A tool for creating statistical models for use with RooFit and RooStats”, CERN-OPEN-2012-016, 29, 2012
- [40] ROOT | A Data Analysis Framework - Cern
<https://root.cern.ch/>
- [41] Z. Marshall (for the Atlas Collaboration), “Simulation of Pile-up in the ATLAS Experiment”, J.Phys.Conf.Ser. 513, 022024, 2014
- [42] ATLAS Collaboration, “Improved luminosity determination in pp collisions at $\sqrt{s} = 7$ TeV using the ATLAS detector at the LHC”, Eur. Phys. J. C73, 2518, 2013

- [43] LHCb Collaboration, “Observation of Excited Λ_b^0 Baryons”, PRL, 109, 172003, 2012
- [44] N Isgur, G Karl, “Ground-state baryons in a quark model with hyperfine interactions”, Phys. Rev. D20, 1191, 1979
- [45] Marek Karliner, Harry J. Lipkin, Nils A. Tornqvist, “Heavy Baryons and Exotics Spectrum”, arXiv:1109.3472, 2011

Acknowledgments

I am deeply grateful to my supervisor Prof. Katsuo Tokushuku who provided carefully considered feedback and valuable comments. Discussions with him have been always illuminating. If he were not my supervisor, it might not be able to finish my study. A lot of his advice could continue to be a big help if I came up against a difficulty on my work. I also would like to express my gratitude to Dr. Shigeru Odaka, Prof. Kunihiro Nagano, and Dr. Takanori Kono. They helped me to understand physics and to resolve many technical issues. Their advice was always accurate for me and I could continue to go on smoothly.

I would like to express the deepest appreciation to Dr. Takeshi Dohmae, Mr. Toyonobu Okuyama, Mr. Yoichi Ninomiya, Mr. Ryuma Hori, too. They not just helped my study but gave a lot of fun. The graduate-school-days that I spent with them is vivid no matter how many years pass by.